© Copyright 2025
Olivia Prado

Endothelial Track Patterning for Directing Vascularization of Engineered Tissues

Olivia Prado

A dissertation

submitted in partial fulfillment of the

requirements for the degree of

Doctor of Philosophy

University of Washington

2025

Reading Committee:

Kelly R. Stevens, Chair

Ying Zheng

Cole A. DeForest

Program Authorized to Offer Degree:
Bioengineering

University of Washington

Abstract

Endothelial Track Patterning for Directed Vascularization and *In Vivo* Integration of Engineered Tissues

Olivia Prado

Chair of the Supervisory Committee:
Kelly R. Stevens
Department of Bioengineering

Engineered organs may one day provide critical therapeutic relief to patients suffering from end-stage organ failure. However, generation of physiological vascular networks within organ-scale tissues that rapidly integrate upon *in vivo* remains a major challenge for clinical translation. Here, we address these challenges by patterning vascular promoting, endothelial collagen "tracks" that guide vessel assembly and improve integration with host circulation within engineered tissue constructs. First, we implant track-containing patches in mice and rats and find significant differences in vascularization and cardiac tissue engraftment, highlighting the often overlooked but crucial role that host biology plays in successful implantation of engineered tissues. We then sought to increase the architectural complexity of engineered vasculature within larger, physiologically relevant tissues and conduct a thorough evaluation of three-dimensional (3D) biofabrication approaches that prioritize sustaining viability of living cells during fabrication

pipelines. Finally, we leverage a 3D biofabrication approach to develop a platform for fabricating complex branching track networks within centimeter scale tissues of many biomaterial matrices– achieving a 10-fold volume increase from all previous track containing tissues. When implanted *in vivo*, these tissues undergo volumetric vascularization, spanning entire tissue constructs, and significantly improve host integration. In all, the work presented here advances tissue engineering by evaluating and emphasizing the importance of host biology, and by developing scalable 3D vascularization methodologies, collectively moving the field closer to the reality of transplantable engineered human organs.

TABLE OF CONTENTS

LIST OF FIGURES

LIST OF TABLES

Acknowledgements

To begin, I'd like to thank my advisor, Dr. Kelly R. Stevens for all her support and mentorship throughout my PhD journey. Kelly, thank you for fostering such a special environment in the Stevens Lab and caring for us not only as scientists or trainees, but individuals as well. I'd also like to thank my committee members, Dr. Ying Zheng, Dr. Cole A. DeForest, and Dr. Claudia G. Vasquez for challenging and supporting me throughout my PhD.

Next, I would like to thank all Stevens Lab members, past and present, for their guidance and camaraderie. I've learned so much from each and every one of you! Special thank you to Dr. Sherina Malkani – I can't imagine working so closely with anyone else these past few years. Your constant (op)timi(sm) and friendship made many of the long days of grad school not only tolerable but filled with laughter!

To my parents— thank you for being such wonderful role models and for making sure my brothers and I had every opportunity growing up. I'm so lucky you were always a phone call away and there to cheer me on whenever I needed it, I would not be here without you! To the rest of my family and friends, both near and far, thank you for being such a wonderful, motivating, and inspiring support system.

Finally, to my partner, Will, thank you for your incredible patience, kindness, and willingness to listen and help. Whether it was talking through day-to-day frustrations, listening to practice talks, watching shows, or playing word games together, you never failed to make me laugh and gain perspective over the years. I am so grateful for your unwavering support!

Chapter 1: INTRODUCTION AND ROADMAP

1.1 INTRODUCTION

Engineered human organs could one day provide life-saving treatments to patients with end-stage organ failure. To achieve this, engineered organs must contain functional, biomimetic vascular networks capable of supplying oxygen and nutrients to large volumes of densely cellularized tissues. These networks must also seamlessly integrate with host circulation and be able to withstand hemodynamic forces when implanted *in vivo*. However, successful generation of vascular networks that capture the cellular and architectural complexity of those found in human organs remains as a major roadblock to clinical translation of engineered organs[1]. Thus, volumetric vascularization strategies that enable rapid host integration of vascular networks that recapitulate those in native tissues would transform tissue engineering and have a major impact on human health.

To engineer tissues containing physiologically relevant vascular networks, a detailed understanding of the biological processes governing vascular formation and development is required. Such processes include vasculogenesis – the de novo formation of blood vessels from endothelial progenitor cells—and angiogenesis—the sprouting and remodeling of new vessels from existing vasculature. In vasculogenesis, which only occurs during embryonic development, endothelial cell progenitors termed angioblasts, amalgamate to form branching networks of solid cord-like structures. Next, the cuboidal angioblasts flatten and move all cell-cell junctions to the cord periphery, forming the primary capillary plexus. Finally, during tubulogenesis, they differentiate into endothelial cells and form lumenized vessels where the compacted cord once was[2–4].

Separately, angiogenesis occurs during embryonic development and in adults, often in response to a tissue hypoxic environment or angiogenic growth factor gradients. To thus transport more oxygen to the tissue, an endothelial "tip" cell sprouts from an existing vessel, enzymatically digests the extracellular matrix (ECM), and recruits proliferating endothelial "stalk" cells to elongate the angiogenic sprout[3,5,6].

Vessels formed via these mechanisms, however, are diameter limited as they typically only involve a few endothelial cells, thus fail to explain de no formation of larger vessels[2–6]. As such, others have investigated alternative de novo vessel formation mechanisms during vasculogenesis that result in large diameter vessels. Specifically, *in vivo* zebrafish studies have shown that when vessels with small diameters coalesce, the endothelial cells making up these vessels rearrange, forming intermediary structures termed "struts" between vessels. Finally, the endothelial cells finish rearranging and form large diameter lumens[7].

Together, vasculogenic and angiogenic processes provide essential insight for engineering vascular networks through self-assembly, harnessing the innate abilities of endothelial cells to organize, remodel, and form vessels. Early vascular engineering studies leveraged these insights, embedding endothelial cells in biological (*e.g.*, collagen, fibrin)[8] and synthetic (PLLA/PLGA)[9] matrices and reported spontaneous self-assembly of microvascular networks *in vitro* and *in vivo*. Importantly, when implanted *in vivo*, these microvascular networks anastomosed, or connected with host circulation, filling the self-assembled human vessels with host red blood cells (RBCs)[9–14].

We recently demonstrated the importance of biomaterial matrix composition in supporting vascular self-assembly and integration of engineered tissues with host vasculature *in*

vivo[15]. After 1 week *in vivo*, engineered tissues made with 5% gelatin methacrylate (GelMA), a modified gelatin, exhibited higher levels of self-assembled microvasculature (magenta) while tissues made with 15% GelMA contained little observable vascular self-assembly (Fig. 1.1A). Moreover, the 5% GelMA tissues can be seen to inosculate with a host vessel (lower right), filling a portion of the self-assembled microvasculature with host blood, while host vessels are seen adjacent to the 15% GelMA tissues, but do not integrate within the tissue. Quantification of huCD31 and TER119 signal revealed significantly higher percent graft in 5% GelMA tissues compared with 15% GelMA tissues, highlighting the drastic affect matrix choice has on tissue vascularization and integration.

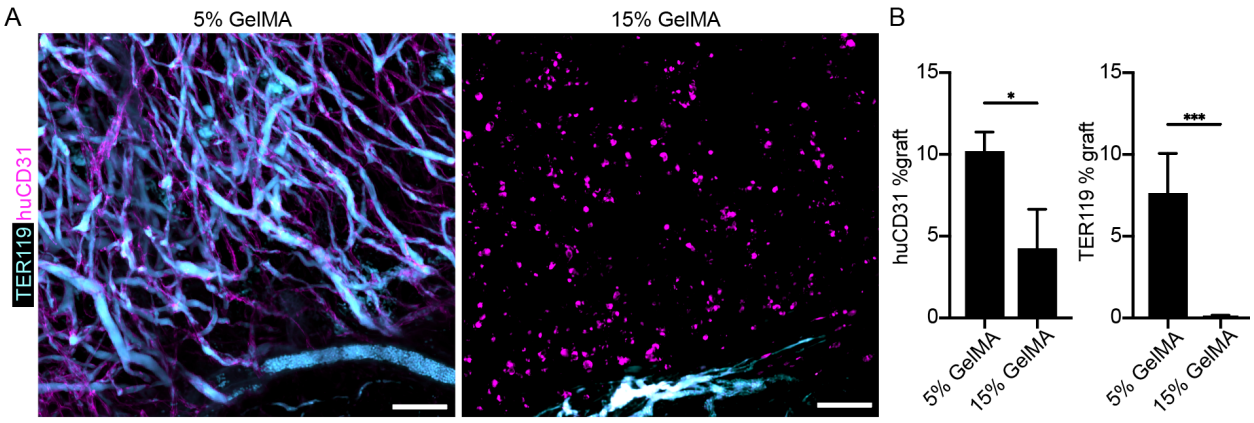

Figure 1.1. Biomaterial matrices differentially support vascular self-assembly *in vivo*.

(A) Unpatterned engineered tissues made with 5% GelMA (left) and 15% GelMA (right) immunostained for human endothelial cells (huCD31, magenta) and host RBCs (TER119, cyan). Scale bars = 100 μm. (B) Percent of total graft that is huCD31 positive. C) Percent of total graft that is TER119 positive. n=7. Mann-Whitney test. Data represented as mean ± SEM. $^{****}p < 0.0001$, $^{*}p < 0.05$.
Adapted from O'Connor & Zhang et al[15].

While the 5% GelMA tissues exhibited more vascularization and host integration than the 15% tissues, is it important to note that even the 5% GelMA tissues were not sufficiently vascularized across the whole tissue. Specifically, when examining the entire explanted tissue,

host-blood filled vessels largely limited to the few millimeters adjacent to the tissue edge (Fig. 1.2). Thus, even in matrices that support self-assembly, self-assembly alone cannot effectively integrate with host circulation and vascularize entire organ-scale tissues.

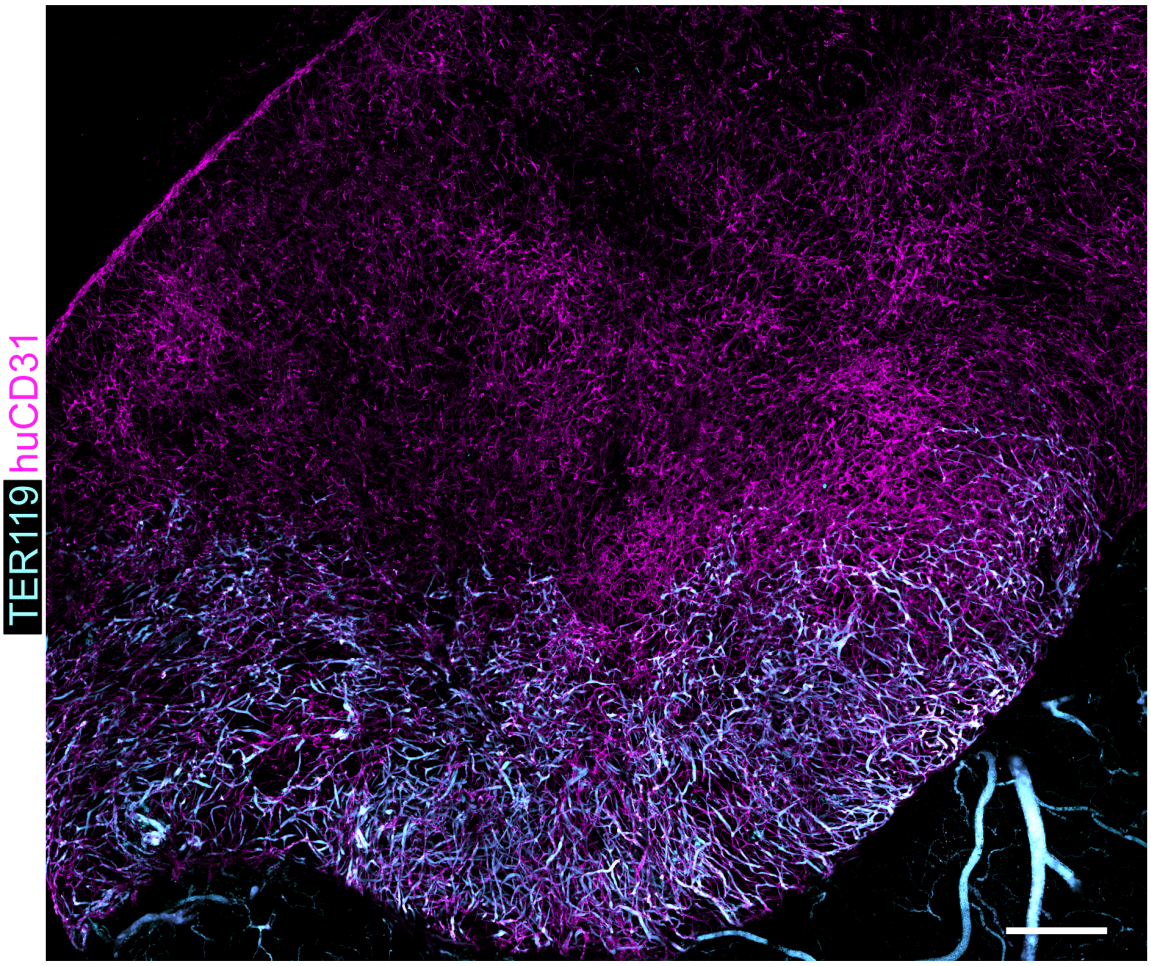

Figure 1.2. Vascular self-assembly insufficiently for large tissue vascularization.

Limited host integration in unpatterned 5% GelMA tissues with self-assembled human vessels (magenta). Host blood (TER119, cyan) localized to outer edges of tissue. Scale bar = 500μm.
Adapted from O'Connor & Zhang et al[15].

For this reason, we and other have developed various biofabrication approaches to improve integration of engineered tissues with host circulatory systems. Towards this end, we and others developed methods to pattern parallel arrays of endothelial cells in neutralized

collagen, or "endothelial collagen tracks" within engineered tissues (Figure 1.3A). When cultured *in vitro*, the endothelial cells self-assemble into a tubular structure around the aligned collagen (Fig. 1.3A, black box). When encapsulated in fibrin, biopsy punched to form 6mm discs (Fig. 1.3A, right), and implanted into athymic nude mice, endothelial collagen tracks, or simply "tracks" as referred to in this work, guide formation of chimeric, host-graft vessels (Figure 1.3B). Specifically, tracks guide formation of capillary- and arteriole-scale vessels parallel to the aligned collagen (Fig. 1.3C) that anastomose with host circulation as early as three days after implant[11–13,16].

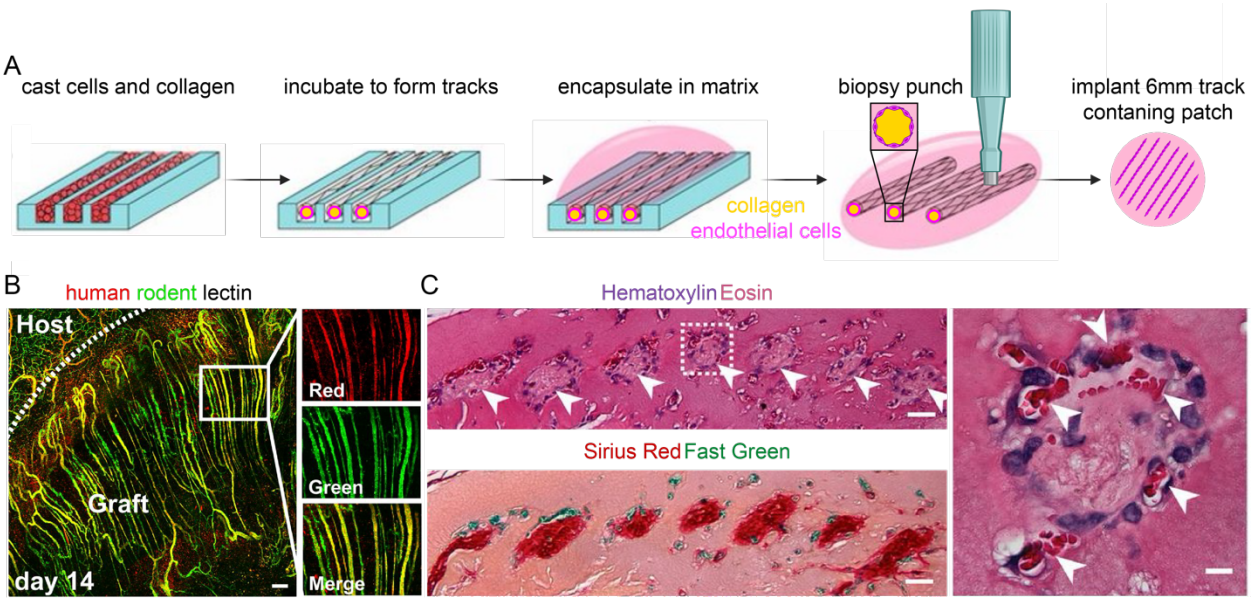

Figure 1.3. Fabrication of micro-molded endothelial collagen "tracks" in fibrin tissues.

(A) Fabrication of track containing patches. Cells in collagen are cast in PDMS molds. Cells and collagen self-organize to form tracks. Tracks are encapsulated and biopsy punched before implant.

(B) Intravenously injected fluorescent human (red) and rodent (green) lectins depict chimeric, host-graft vessels following parallel array of patterned tracks after 14 days *in vivo*. Scale bar = 150μm.

(C) Cross-section of track containing patches after 7 days *in vivo* stained for hematoxylin and eosin (top), and Sirius Red Fast Green (bottom). Scale bars = 25μm. Host blood-filled vessels form around collagen track (white arrows, right inset). Scale bar = 5μm.

Adapted from Baranski et al.

Importantly, the inclusion of tracks improved hepatic function and engraftment of engineered liver tissues when compared to tissues without tracks in mice[12,14] (Figure 1.4). Encouraged by these results, our group then sought to apply track patterning to cardiac tissue engineering, where rats are the widely used host model. Surprisingly, after 7 days on the epicardial surface of rats, there was little to no evidence of tracks or track guided vasculature in the tissues (Fig. 1.4a, b). Instead, a significant increase in nuclear infiltration and collagen deposition suggests a robust inflammatory response with few host-blood containing vessels present (Fig. 1.4b, d, e).

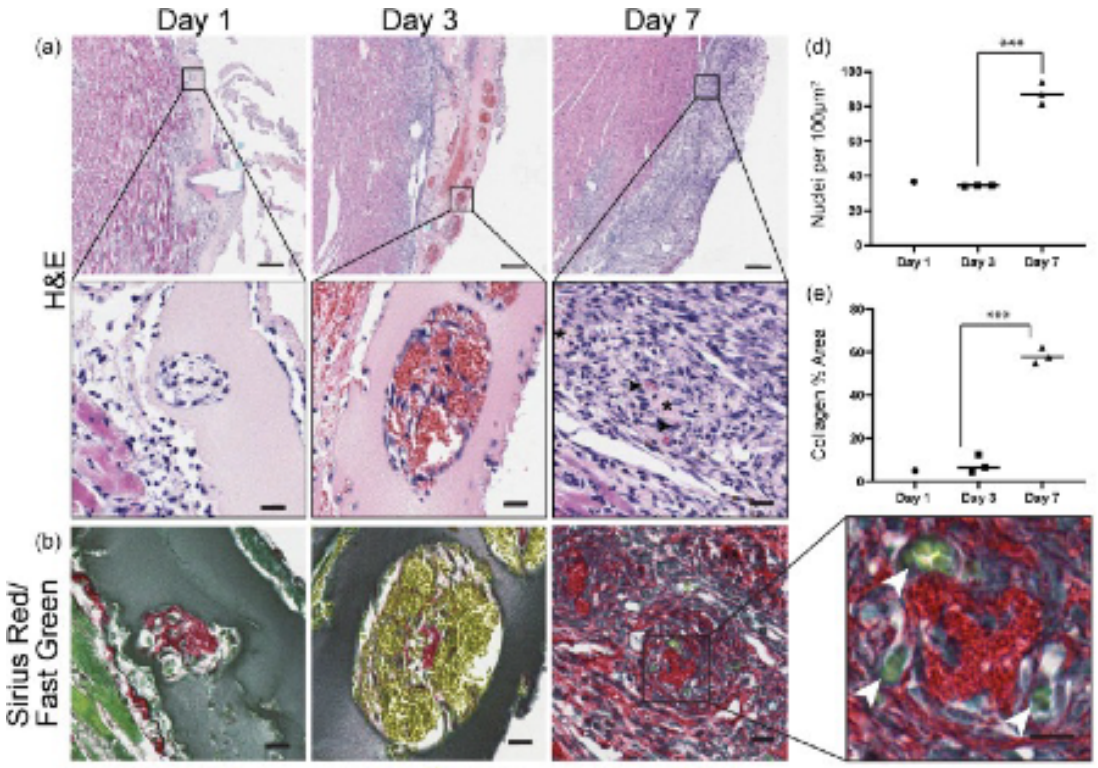

Figure 1.4. Epicardial track containing patches show signs of an inflammatory response while few patterned track vessels are observed after 7 days *in vivo* in rats.

(a) Hematoxylin & Eosin staining of track containing patches explanted at 1, 3 and 7 days in rats. Scale bar = 20 μm, inset scale bar = 10 μm.

(b) Sirius Red/Fast Green staining of track containing patches explanted at 1, 3 and 7 days in rats. Scale bar = 20 μm, inset scale bar = 10 μm.

(d) Quantification of nuclear infiltration. ANOVA with Tukey's honestly significant difference (HSD) Error bars indicate S.E.M ***p < 0.001.
(c) Quantification of collagen as percent % area. ANOVA with Tukey's honestly significant difference (HSD) Error bars indicate S.E.M ***p < 0.001.
Adapted from Brady et al[16].

In all, vascular promoting tracks made up of self-organized endothelial cells around a collagen core have shown potential for improving host mediated vascularization and engraftment of engineered tissues. However, various applications of track-containing tissues have yet to be explored. The remained of this work describes further investigation into applications of vascular promoting tracks, highlighting key findings and biofabrication developments achieved that collectively advance tissue engineering towards clinical translation of engineered tissues.

1.2 ROADMAP

Engineered organs may one offer critical therapeutic relief to patients with end stage organ failure that suffer while waiting for donor organs to become available. A key component of engineered functional organs is generating volumetric vasculature to maintain tissue viability and function while integrating rapidly with host circulation. Here, we present significant steps toward this goal, leveraging vascular promoting tracks to evaluate *in* vivo vascularization and engraftment, and to engineer centimeter-scale tissues via 3D printing enabled track patterning.

In **Chapter 2,** we use track containing fibrin patches, as depicted in Figure 2, to evaluate the role of host biology and implant location on engineered tissue engraftment and guided vascularization *in vivo*. We fabricate track containing patches with various parenchymal cell populations and implant them in two distinct implant locations (abdominally and epicardially). We implant these track containing patches in two host models – athymic nude mice and nude rats

– and report diverging vascularization and engraftment responses. We show evidence of track guided vascularization in engineered tissues implanted in mice at both implant locations, but a nearly complete loss of vascular patterning in rats. Conversely, when cardiomyocytes were incorporated into track containing tissues, we observed more robust engraftment of the cardiomyocytes when sutured to the epicardial surface of rats, 3-fold greater than engraftment of the same tissues in mice. In all, we highlight the often overlooked and critical role host biology plays in engineered tissue vascularization and engraftment. Attention to host biology will prove critical as we scale engineered tissues to physiologically relevant sizes.

While fibrin track containing patches allowed us to investigate the role host biology plays in engineered tissue vascularization and engraftment, the micromolding approach used to fabricate such patches limits tracks architectures to a single plane, and tissue sizes to planar discs. As such, we next sought to develop new fabrication methods to pattern tracks in 3D with complex architectures, at larger, more physiologically relevant sizes. Thus **Chapter 3** evaluates various biofabrication technologies, identifying sacrificial templating as a promising biofabrication strategy for patterning hierarchal vasculature within engineered tissues. Briefly, sacrificial templating involves fabrication of temporary or removable vascular networks that can be embedded in cellularized matrices. When removed, the sacrificial material leaves a hollow network replicating the architecture of the patterned sacrificial material. We broadly categorize sacrificial templating methods into two groups— coupled and decoupled approaches. Coupled approaches print the sacrificial ink and the cellularized matrices at the same time, while decoupled methods first print a stand-alone sacrificial template and later cast a cellularized matrix around it. We highlight the biocompatibility benefits of decoupled methods, given that cells are shielded from harmful fabrication conditions, as the template is produced before cells

are introduced into fabrication pipelines. We then discuss various sacrificial agent mechanisms, differences in achievable resolutions with various printing technologies, and long-term stability of templated vasculature *in vivo*. Finally, we discuss sacrificial templating approaches compatible with materials that support vascular self-assembly, leveraging biology to form microvasculature networks. These combinatorial approaches are particularly exciting, as no single fabrication technology has been able to recapitulate the entire vascular hierarchy (5 μm to 10 mm).

In **Chapter 4,** we then go on to leverage a decoupled sacrificial templating approach to pattern tracks within centimeter-scale tissues— a 10-fold volumetric increase from previous track containing tissues. Specifically, sacrificial isomalt templates enabled us to pattern track networks in several matrices that have been shown to support vascular self-assembly. To investigate whether tracks similarly improve host integration as shown in Chapter 1, we fabricated patterned tracks networks in sacrificially templated tissues of various matrix compositions and implanted them *in vivo*. After the tissues were explanted, we observed formation of host blood filled vasculature closely following the branching vascular geometries of the patterned tracks. We then assessed vascular network characteristics, host integration, and tissue fidelity of each matrix used. We identified compositions of cellularized matrices that supported volumetric vascularization of implanted tissues, utilizing 2D and 3D analyses to robustly characterize vascularization responses. In all, we present a combinatorial vascularization platform and demonstrate integration of track-guided and self-assembled vasculature with host circulation.

Finally, **Chapter 5** summarizes the key findings and advancements developed in this work moving engineered tissues closer to clinical translation. To end, we address limitations of the work presented here and the remaining challenges in the field.

Chapter 2: ENGINEERED TISSUE VASCULARIZATION AND ENGRAFTMENT DEPENDS ON HOST MODEL

Adapted from: Brady, E. L.*, and **Prado, O.***, *et al.* Engineered tissue vascularization and engraftment depends on host model. *Sci Rep* **13**, 1973 (2023).
Reproduced with permission.

Developing vascular networks that integrate with the host circulation and support cells engrafted within engineered tissues remains a key challenge in tissue engineering. Most previous work in this field has focused on developing new methods to build human vascular networks within engineered tissues prior to their implant in vivo, with substantively less attention paid to the role of the host in tissue vascularization and engraftment. Here, we assessed the role that different host animal models and anatomic implant locations play in vascularization and cardiomyocyte survival within engineered tissues. We found major differences in the formation of graft-derived blood vessels and survival of cardiomyocytes after implantation of identical tissues in immunodeficient athymic nude mice *versus* rats. Athymic mice supported robust guided vascularization of human microvessels carrying host blood but relatively sparse cardiac grafts within engineered tissues, regardless of implant site. Conversely, athymic rats produced substantive inflammatory changes that degraded grafts (abdomen) or disrupted vascular patterning (heart). Despite disrupted vascular patterning, athymic rats supported > 3-fold larger human cardiomyocyte grafts compared to athymic mice. This work demonstrates the critical importance of the host for vascularization and engraftment of engineered tissues, which has broad translational implications across regenerative medicine.

2.1 INTRODUCTION

The need for transplantable organs far outpaces the number of available donor organs. As this discrepancy grows, an increasing number of patients on organ transplant waiting lists will die awaiting an organ[17]. Tissue engineering could address this problem by generating an alternative source of healthy human tissue for those unable to access donor organs. However, without a vasculature engineered tissues are limited in thickness by the diffusion limit of oxygen (100-200μm)[18–20]. Thus, vascularization is required to replicate the tissue thickness and complexity of commonly transplanted organs such as liver, lung, or heart.

Major progress towards vascularizing engineered tissues arose from the discovery that endothelial cells have the capacity to self-assemble into microvessel-like networks *in vivo*. These early experiments found that when endothelial cells were encapsulated in natural (fibronectin/collagen)[8] or synthetic (PLGA/PLLA)[9] hydrogel scaffolds and implanted in immunodeficient mice, they formed tubular networks that connected (anastomosed) to host circulation and contained host blood. Later studies further showed that including both endothelial and stromal cells within engineered tissues enhanced the vascular self-assembly process, leading to the formation of perfused, vascular networks that were at least in part derived from the grafted cells[21,22].

Despite this progress in leveraging cooperation between the graft and host for tissue vascularization, randomly self-assembled networks exhibited irregular vessel architecture, susceptibility to early thrombosis[23,24], and a delay between implantation and perfusion during which sensitive cells are deprived of oxygen. To address these limitations, we and others have developed methods to exert additional control over vascular architecture within the engineered tissue[12,25]. We developed a method to pattern endothelial cells and collagen into arrays of parallel

channels and then encapsulate the resultant "endothelial tracks" within engineered tissues[12,25]. Upon implantation in athymic mice, these endothelial tracks act as "railroad tracks" that guide the formation of chimeric host-graft vessels that became anastomosed with the host circulation. Importantly, inclusion of patterned vascular networks improved the survival of functional hepatocytes within engineered liver tissue over randomly organized networks[12]. Due to this early success, we then sought to extend our approach for guided vascularization for cardiac tissue engineering, by implanting engineered tissues with endothelial tracks on athymic rat hearts[16]. We were surprised to find robust inflammation and no evidence of patterned vessels after tissue implantation[16]. These results drew our attention to the likely critical yet often overlooked role that factors such as host biology and anatomic location of the grafted tissue may play in affecting vascular integration and engraftment of engineered tissues. We hypothesized that different host models (here, animal models) and anatomic implant locations play a role in the vascularization of human engineered tissues upon their implantation *in vivo*.

Here, we test this hypothesis and report divergent responses in vascularization and cardiomyocyte engraftment of engineered tissues after their implantation in athymic mice *versus* athymic rats. These results suggest that guided vascularization and cardiomyocyte survival are supported by different host factors, which vary across animal models.

2.2 RESULTS

2.2.1 *Patches with endothelial "tracks" retain patterning and anastomose with host circulation in the mouse abdomen and heart.*

We previously showed that patterning endothelial cells and collagen into track-like structures within fibrin-based engineered tissues facilitates the guided formation of patterned,

chimeric host-graft vessels upon their intraperitoneal (IP) implantation in the abdomen of athymic mice. Yet paradoxically, we also showed recently that such engineered tissues are rapidly degraded and do not retain vessel patterning after 7 days of implantation on the heart of athymic rats[16]. We first hypothesized that differences in host response across anatomic locations of the implanted tissue, in this case between the heart and the abdomen, might explain these results.

To methodically test this hypothesis here, we suspended endothelial cells (HUVECs) and stromal cells in collagen within a PDMS mold with parallel channels to form "endothelial tracks", then encapsulated these tracks within fibrin to create engineered tissues, as we have done before[12]. We then randomly allocated these tissues into two groups and sutured the tissues from each group onto either the intraperitoneal (IP) gonadal fat pad or on the epicardial surface of the heart in athymic nude mice (Fig. 2.1a). These engineered tissues were explanted at either 3- or 7-days post implantation for histological analyses. Upon gross examination at explanted tissues, we identified intact engineered tissues with minimal adhesions at 3- and 7-day timepoints at each anatomic implant location (Fig. 2.1a). Furthermore, Hematoxylin and Eosin (H&E) and Sirius Red staining of sectioned explanted tissues revealed regularly spaced clusters of cells in a pattern reflecting track cross-sectional geometry from both locations at 3 and 7 days (Fig. 2.1b, Fig. 2.1c). Within these clusters, these stains identified a collagen core surrounded by loosely organized cells at 3 days (Fig. 2.1b) that consolidated to form blood-containing lumens at the periphery of each track by 7 days (Fig. 2.1c), similar to our previous results for tissues implanted IP in mice[12,25]. We next assessed inflammation by looking for nuclear infiltration and collagen deposition within the explanted engineered tissues. Whereas hematoxylin-positive nuclei were present at the grafted tissue boundary, nuclear infiltration did not extend into the graft,

suggesting that the inflammatory response was contained at the host-graft interface. Furthermore, all explanted tissues had an intact Eosin-positive fibrin matrix without interstitial collagen deposition (Fig. 2.1b, c). Taken together, these results demonstrate a morphologic pattern of track-associated lumen formation with minimal inflammation in both IP and epicardial implant locations in athymic nude mice.

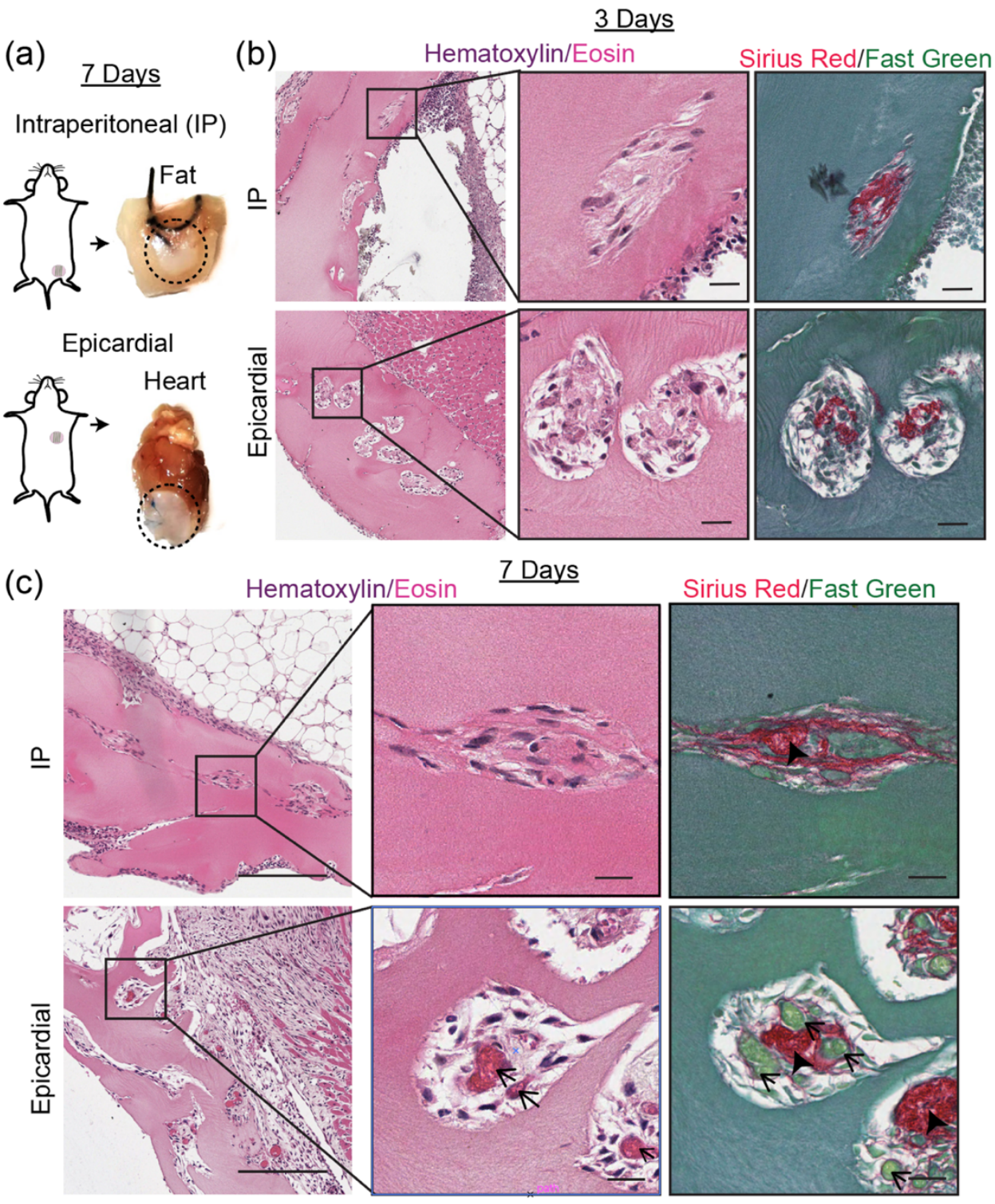

Figure 2.1. Track patterning visible at 3 days but guided vascularization occurs in Intra-peritoneal (IP) and epicardial locations after 7 days in mice.

(a) Explants from gonadal fat pad (IP) or epicardial (heart) locations have intact patches at 7 days (dotted lines).
(b) H&E and Sirius Red/Fast Green stains of epicardial and abdominal track- containing patches explanted at 3 days. Scale bar = 200μm. Inset scale bar = 20μm
(c) H&E and Sirius Red/Fast Green stains of day 7 explants show track-associated vessels in both IP and epicardial implants. Insets: open arrows indicate blood pools, closed arrows mark collagen cords. Scale bar = 100μm (left). Inset scale bar = 20μm.

To further explore the phenotype of cells in these structures, we performed immunostaining with a human specific anti-huCD31 antibody and a mouse specific red blood cell marker (TER-119). At 3-days post implantation, huCD31+ cells remain primarily clustered at the periphery of the tracks in the IP implants, with evidence of some rudimentary lumen formation more predominantly in the epicardial implants (Fig.2.2a). Quantification of collagen, fibrin, cellular nuclei (Hoechst), huCD31, and blood (TER-119) showed greater huCD31+ area in the epicardial group compared to IP implants at 3 days (Fig.2.2b).

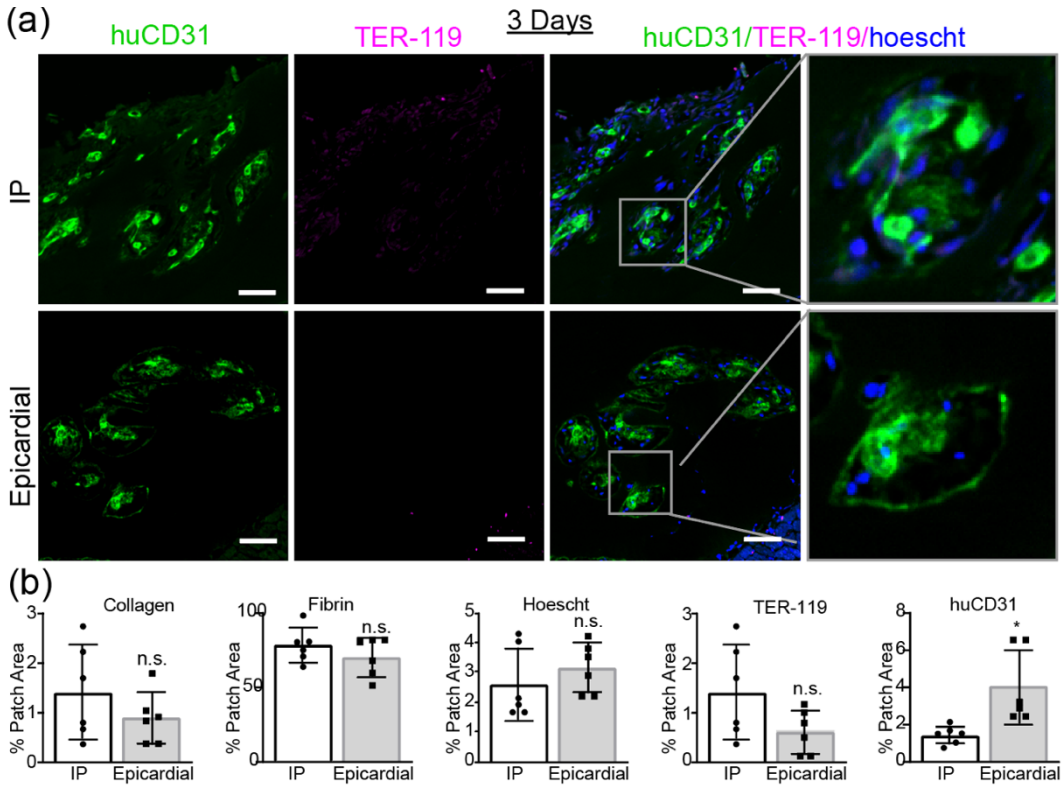

Figure 2.2. Immunostaining of IP and epicardial track containing patches after 3 days.

(a) Immunostaining of 3-day patches with huCD31 (green), TER-119 (magenta), and Hoescht (blue). Scale bar = 50μm.
(b) Quantification of fibrin, collagen, Hoescht, TER-119, and huCD31 at day 3 reported as percent of patch area. Error bars show S.D.

By 7 days, the tracks at both implant locations are lined with tracks of huCD31+ lumen that contain mouse red blood cells (RBCs) (Fig.2.3a). Additionally, this staining confirmed that tracks geometry was retained in patches from either implant location, with huCD31+ cells found almost exclusively in distinct clusters of lumens spaced approximately 50-100μm apart (Fig.2.3a, arrows). However, by 7 days this had resolved and there were no significant differences in patch architecture, inflammation, or vascularization between implant locations (Fig. 2.3b). By 7 days in both groups, nearly 100% of tracks were associated with TER-119 (RBC) containing huCD31+ lumens (Fig. 2.3c). Overall, our results demonstrate that guided vascularization[12] occurs at both IP and epicardial (heart) implant locations in athymic nude mice.

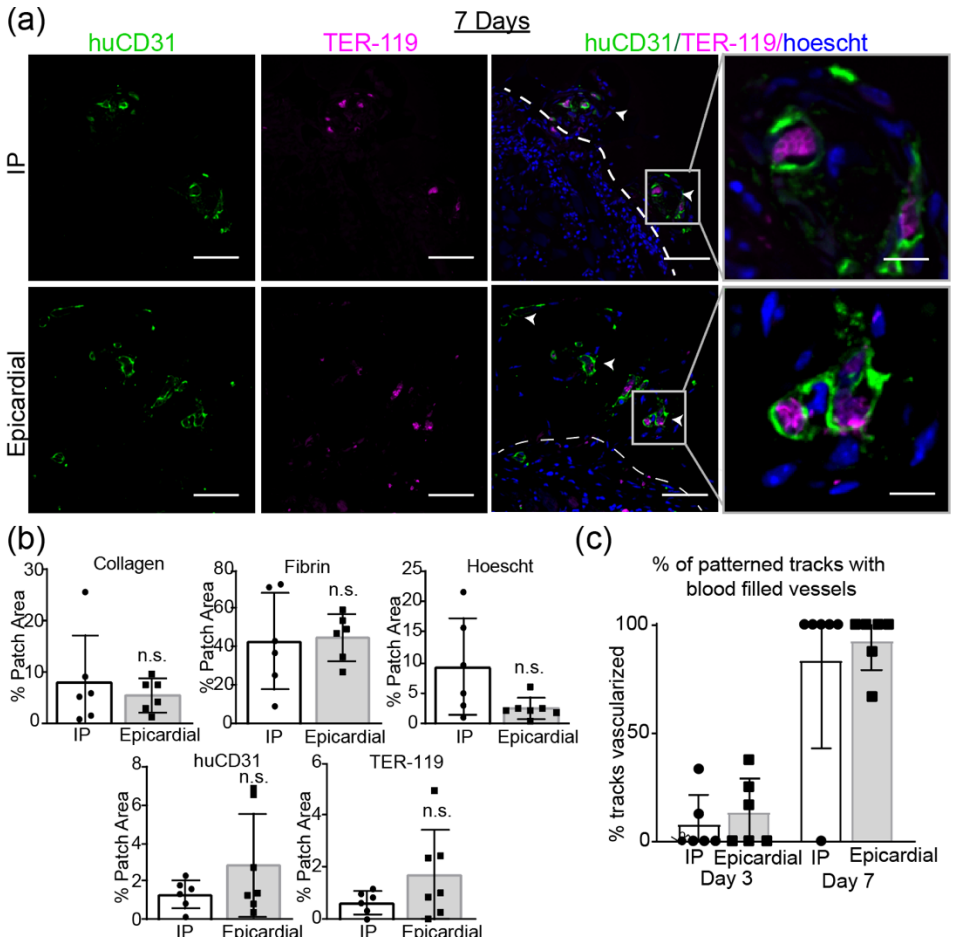

Figure 2.3. Immunostaining of IP and epicardial track containing patches after 7 days.

(a) Immunostaining of day 7 explants confirm regular clusters (white arrows) of graft-derived vessels (huCD31+) filled with mouse blood (TER-119+). Scale bar = 50μm. Inset scale bar=10μm.
(b) Quantification of staining by percent patch area shows no difference between groups in collagen, fibrin, nuclei, blood (TER-119), or huCD31. Each point represents an individual animal. Error bars reported as S.D. n = 7 (IP), n = 7 (Epicardial). (d) Percentage of tracks that are associated with blood-containing lumens (% tracks vascularized). Error bars show S.D.

2.2.2 *Tracks-containing cardiac patches in mice develop patterned vessels with increased lumen size.*

After we had confirmed that guided vascularization occurs in the mouse heart, we next sought to apply this technique for cardiac tissue containing not only vascular cells, but also

human pluripotent stem cell-derived cardiomyocytes ("cardiomyocytes"). We fabricated engineered tissues containing randomly seeded cardiomyocytes along with three endothelial cell patterning compositions: 1) patterned EC tracks as well as randomly seeded ECs in the bulk (tracks + bulk), 2) ECs in tracks only (tracks), 3) randomly seeded ECs in the bulk only (bulk) (Fig. 2.4a).

To compare vascularization between groups, we first used 2D histology to assess overall tissue structure and look for evidence of blood-vessels within the grafts after 7 days of engraftment, since our previous experiment (Fig. 2.1-2.3) had indicated that host-graft anastomosis occurs by this timepoint. Hematoxylin and Eosin and Sirius Red stains suggested guided vascularization had occurred, with blood pools associated with collagen tracks in both tracks+bulk and tracks-only groups (Fig. 2.4b). Similar large blood consolidations were absent in patches lacking tracks (Fig. 2.4b). Patches from all groups remained intact with minimal collagen deposition or excessive inflammation, with no significant differences between groups (Fig. 2.4c). To further compare graft-derived vessel morphology between groups, we co-stained for human endothelium (huCD31), mouse erythrocytes (TER-119), and the pericyte marker α-smooth muscle actin (Fig. 2.4d). Compared to patches with only unpatterned ECs, we found that graft-derived endothelial cells in tracks-containing groups more efficiently recruited blood (Fig. 2.4c). We then assessed for the presence of α-SMA+ pericytes, which are a marker of mature microvessels[26]. We found the tracks-associated vessels often had nearby α-SMA+ cells (Fig.3d). Additionally, some of these vessels had α-SMA+ cells partially or fully encircling the huCD31+ lumen, as would be expected in mature vessels (Fig. 2.4d, inset). The increased efficiency of blood recruitment and the presence of vessel associated α-SMA+ cells suggest that guided vascularization could support stable vessel formation in the mouse heart.

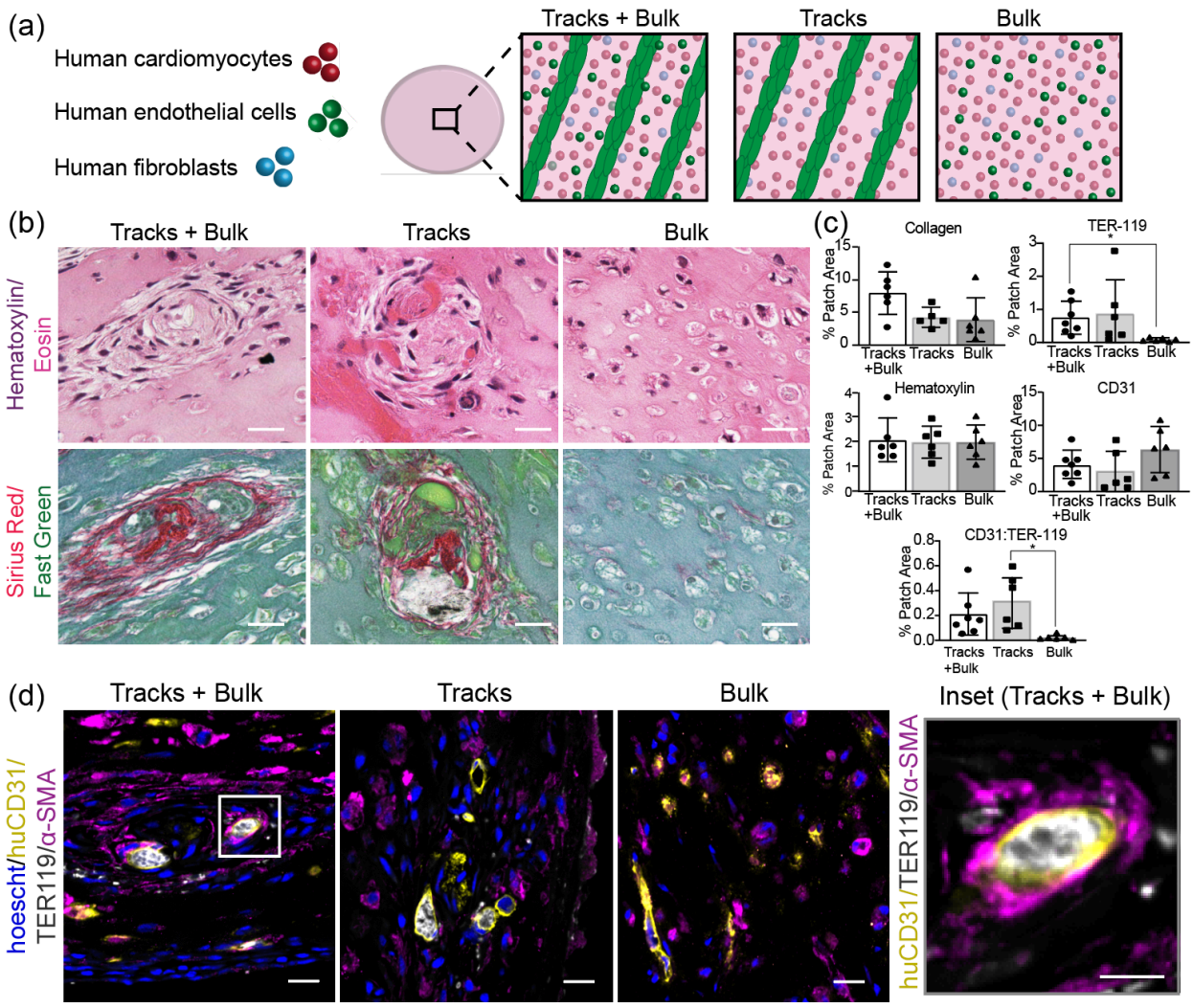

Figure 2.4. Tracks guide vascularization of engineered cardiac tissues in the athymic mouse heart.

(a) Human cardiomyocytes, ECs, and stromal cells were used to create cardiac patches with different tissue geometries.

(b) Hematoxylin & Eosin and Sirius Red demonstrate tracks-associated blood pools in patches containing EC tracks harvested at 7 days post-implantation. Scale bar = 25μm.

(c) Quantification of collagen, nuclei, huCD31, TER-119, and huCD31: TER-119 between patches with different EC configurations. Error bars report S.D. n = 6 (Tracks + Bulk), n = 5 (Tracks), n = 6 (Bulk)

(d) Patterned huCD31+ vessels are filled with blood (TER-119) and recruit α-SMA pericytes. Scale bar = 20μm. Inset scale bar = 10μm.

While the clustered pattern of graft-derived vessels in the 2D staining data suggested that vessels retained tracks geometry in mice, we wanted to better understand three-dimensional (3D) engineered vascular geometry on the surface of the heart. To do this, we stained whole tissues for human endothelium (huCD31) and imaged the cleared samples with confocal microscopy. We also visualized perfused vessels using fluorescent lectin that had been introduced intravenously prior to harvest. In both tracks-containing groups, we identified a parallel array of huCD31+ vessels (Fig. 2.5). Cross-sections of these tracks revealed hollow 20-40μm lumens forming "trunks" aligned with the axis of each "track", and smaller vessels branching orthogonally from these larger trunks. No patterning was evident in the bulk-only patches. Instead, the bulk-only tissues had small vessel-like structures scattered throughout and many huCD31+ cells remained as isolated cells not incorporated into vessels (Fig.2.5). The group containing both tracks and HUVECs in the bulk had features of both the tracks and bulk-only groups, with larger vessels in the tracks and smaller vessels and unincorporated huCD31+ cells throughout.

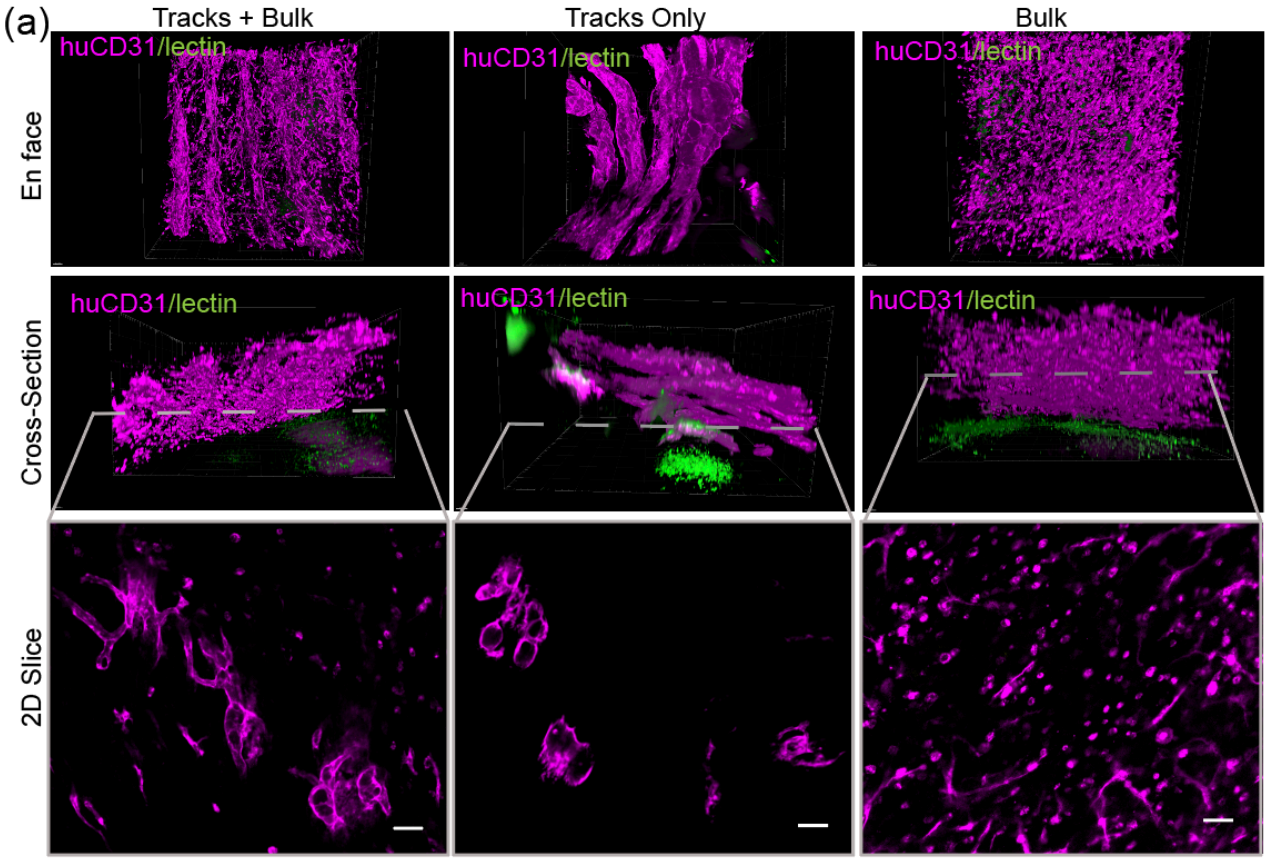

Figure 2.5. Three-dimensional characterization of vessel geometry in engineered cardiac tissues. (a) Top: 3D visualization of huCD31 (magenta) and intravenously circulated fluorescent lectins (UEA-1 and LEL, green). Bottom: single 2D slice taken from z-stack at level indicated by dashed line. Scale bar = 50μm.

To quantify the observed differences in vessel size between tracks-associated vessels and those derived from randomly seeded HUVECs, we used Vesselucida software to generate tracings of vessels from each engineered tissue (Fig. 2.6a). Analysis of these tracings showed that vessels in the bulk-only group were significantly smaller than those in the tracks-containing groups, with an average of 86% of vessels in bulk-only patches having a diameter <10μm and less than 1% having diameter >20μm (Fig. 2.6a). The tracks-associated vessels were significantly larger, with an average diameter close to 20μm (Fig. 2.6c). In the tissues with both tracks and bulk HUVECs, vessels in the tracks (black) more closely matched the tracks-only

group, while vessels in the bulk (gray) were similar in size to those in the bulk-only cohort (Fig.2.6c). While 2D immunostaining identified blood within graft-derived lumens, indicating anastomosis with the host circulation, we very rarely observed lectin+ vessels in the patches in any group (Fig. 2.5), suggesting that flow in patches was too slow to be detected in the lectin circulation time. Taken together, these data indicate that in the athymic mouse heart EC tracks guide the formation of patterned blood-filled vessels with larger lumen sizes compared to vessels assembled from homogeneously seeded cells, albeit with circulation that remains lower than that of the host coronary vasculature. Thus, guiding vascularization with EC tracks may be a viable strategy for cardiac tissue engineering applications in an appropriate host setting.

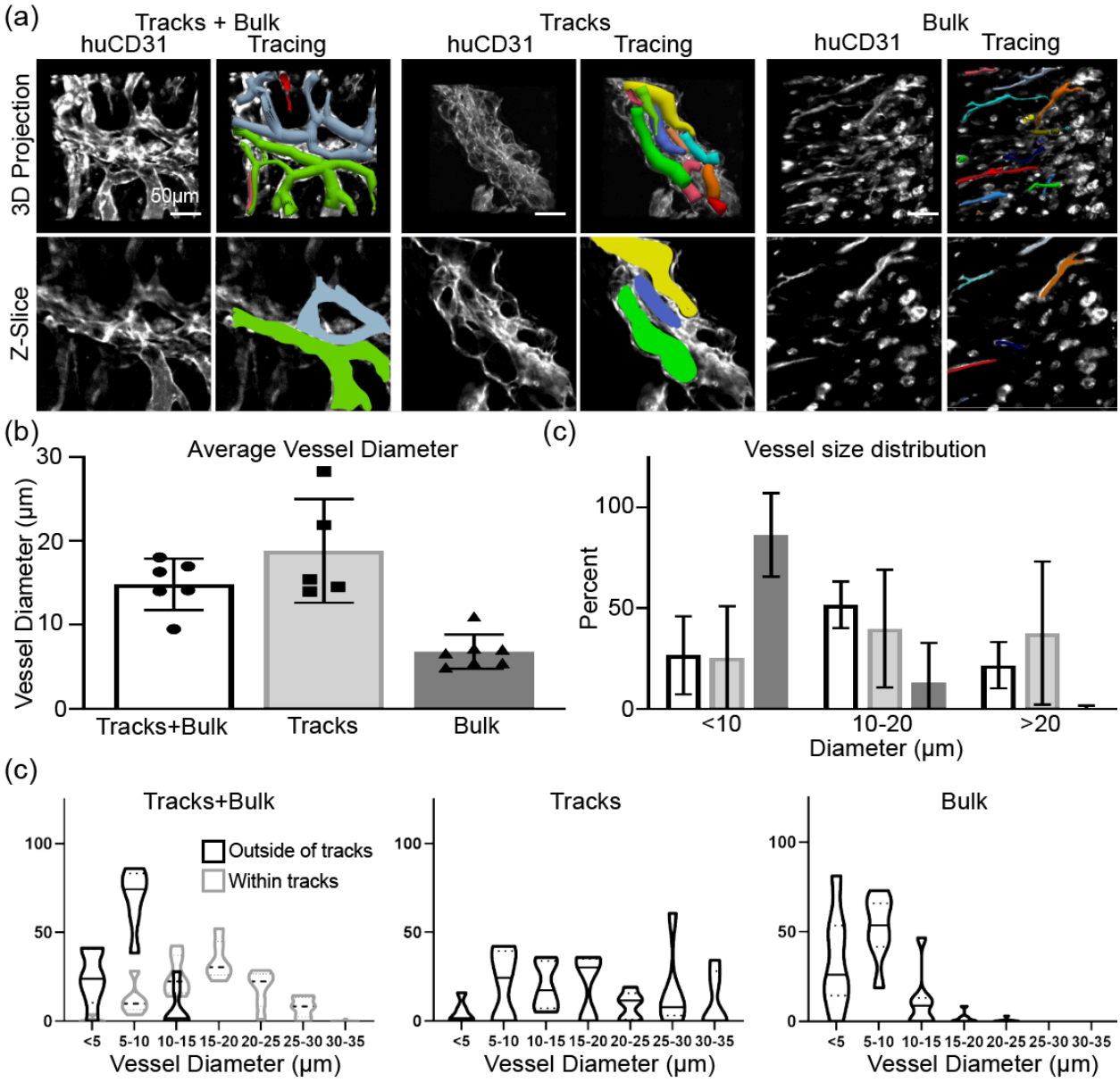

Figure 2.6. Vessel tracing and morphometric analysis.

(a) Vesselucida software was used to trace all vessels within a 250µm^3 ROI taken from the center of each patch.

(b) Quantification of vessel diameter from traced vessels. Error bars indicate S.D.

(c) Vessels found outside tracks (black) are smaller than those found within tracks (grey). n = 6 (Tracks + Bulk), n = 5 (Tracks), n = 6 (Bulk)

2.2.3 *Animal model differences in response to tracks-containing human cardiac patches*

From our studies of tracks-containing cardiac tissues in mice, we saw that vascular patterning was retained, and furthermore that endothelial tracks influence the organization and size of vessels formed *in vivo*. Yet we were surprised to find that despite vessel formation and anastomosis *in vivo*, the human cardiomyocyte grafts remained rather small and dispersed across all conditions (Fig. 2.7). We found this particularly interesting since we and others have observed substantive cardiac grafts previously in other settings, such as in the athymic nude rat. Thus, we wanted to further explore the host response to grafts in athymic nude mice *versus* rats.

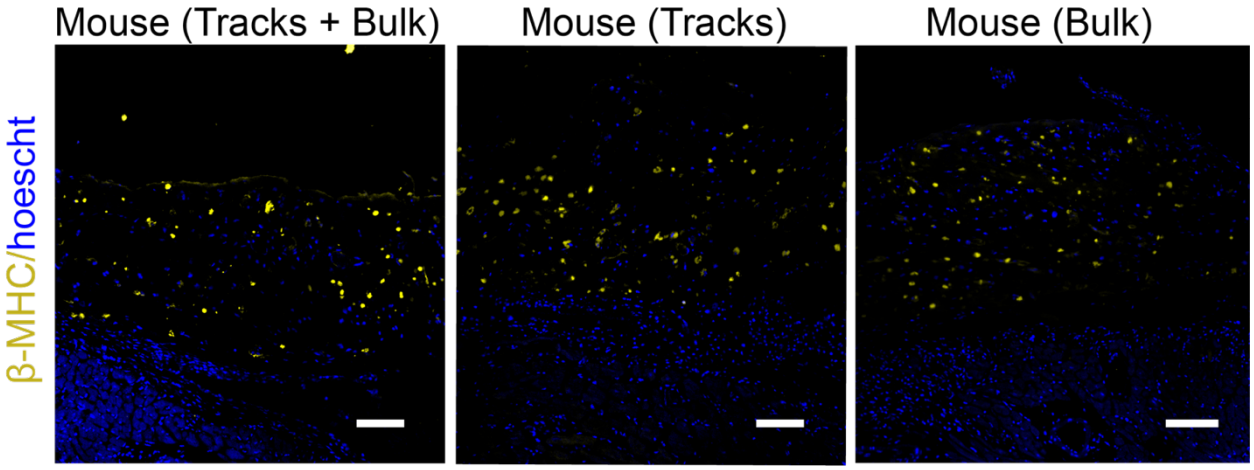

Figure 2.7. β-MHC+ cardiac grafts in mice harvested at 7 days remain sparse despite guided vascularization. Scale bar = 100μm.

As a first step, we performed an "implant location" study in athymic nude rats, as we had done in athymic nude mice (Fig. 2.1-2.3). We implanted identical fibrin patches containing endothelial tracks either in the abdomen (IP space) or the epicardial surface of athymic rats. Upon retrieval of the tissues from the IP location, we were able to identify the location of the implant by visualizing the suture but could not identify any of the engineered tissues in any of

the animals, either by gross observation or upon histologic examination through the plane of the suture (Fig. 2.8.

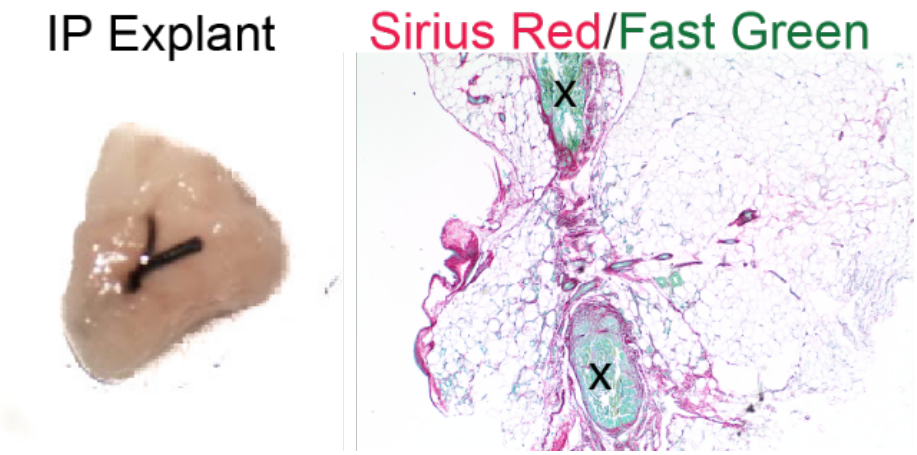

Figure 2. 8. Fibrin tissues containing EC tracks are obliterated in the athymic rat IP space at 7 days.

Left: explanted gonadal fat with intact suture but no visible patch. Right: Sirius Red/Fast Green through the middle of the suture (suture = x) fails to reveal remaining fibrin.

Conversely, all epicardial implants were identified grossly at the time of explant and further histologically processed. Histological staining of the epicardial explants with Hematoxylin and Eosin and Sirius Red revealed an inflammatory reaction characterized by nuclear infiltration, collagen deposition, and minimal remaining fibrin matrix (Fig.2.9a), consistent with our previous findings[16]. Further immunostaining revealed numerous CD68+ macrophages throughout the tissue and concentrated around the perimeter of the remaining fibrin (Fig. 2.9b), as well as microvessels lined with huCD31+ graft-derived endothelial cells scattered throughout the graft (Fig. 2.9c). Further 3D huCD31 staining, clearing, and imaging of whole tissues (Fig. 2.9d) demonstrated the presence of human vessel structures with diameters in the range of 5µm-10µm, with minimal architectural patterning (Fig.2.9d). Thus, athymic rats appeared to produce a robust inflammatory response that seemingly degrades engineered tissues

in the IP space and disrupts vessel patterning in those implanted on the epicardial surface of the heart[16].

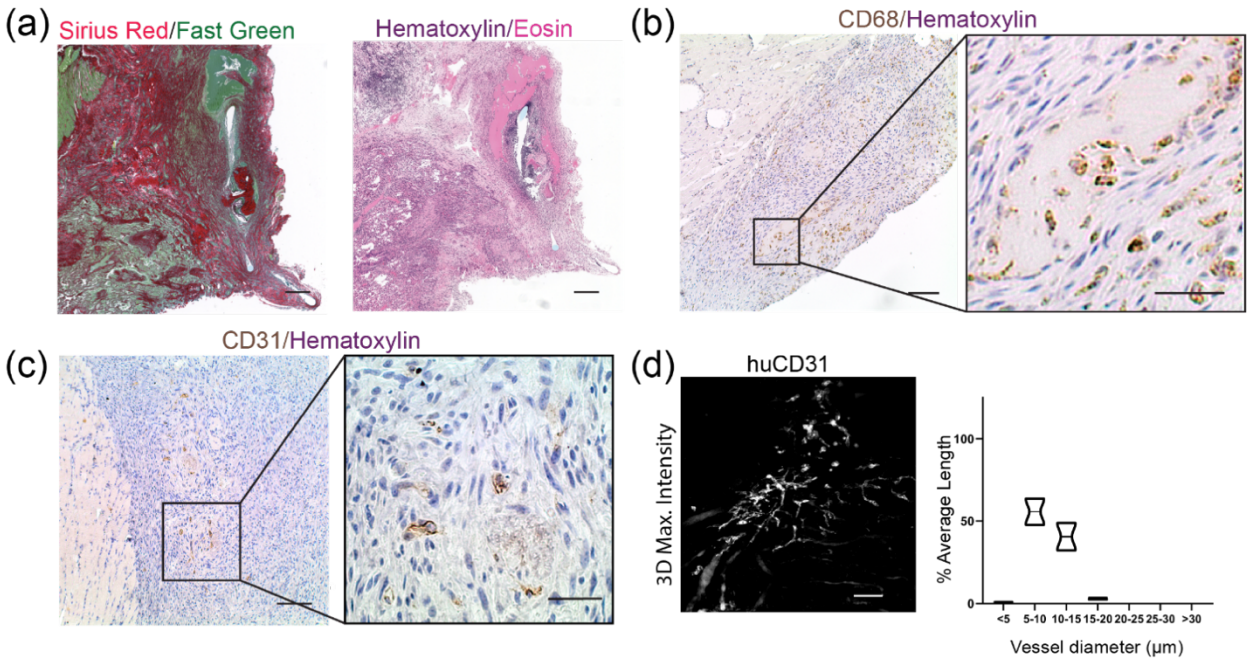

Figure 2.9. Fibrin patches with tracks induce inflammation on the athymic rat heart.

(a) Sirius Red staining reveals the fibrin matrix has been replaced by dense collagen (left). Hematoxylin & Eosin shows robust nuclear infiltration throughout the patch, with no evidence of patterned vessels (right). Scale bar = 100µm.

(b) Immunostaining identifies numerous CD68+ macrophages clustered around the remaining fibrin (inset). Scale bar = 50µm, inset scale = 20µm.

(c) Staining for huCD31 reveals sparse graft-derived vessels. Inset shows close view of a track with occasional graft-derived vessels in the vicinity. Scale bar = 50µm, inset scale = 20µm

(d) 3D projection of huCD31 staining from a cleared tissue (left). 3D stacks were used to generate vessel traces and quantify lumen size using Vesselucida software (right). Scale bar = 100µm.

We next directly compared engraftment of engineered cardiac tissues on the epicardial surface of athymic mouse or rat hearts. We fabricated cardiac tissues containing endothelial cells in both tracks and the tissue bulk, as well as human cardiomyocytes (Fig. 2.10a, b). These tissues were then distributed for implant on the hearts of athymic rats or mice.

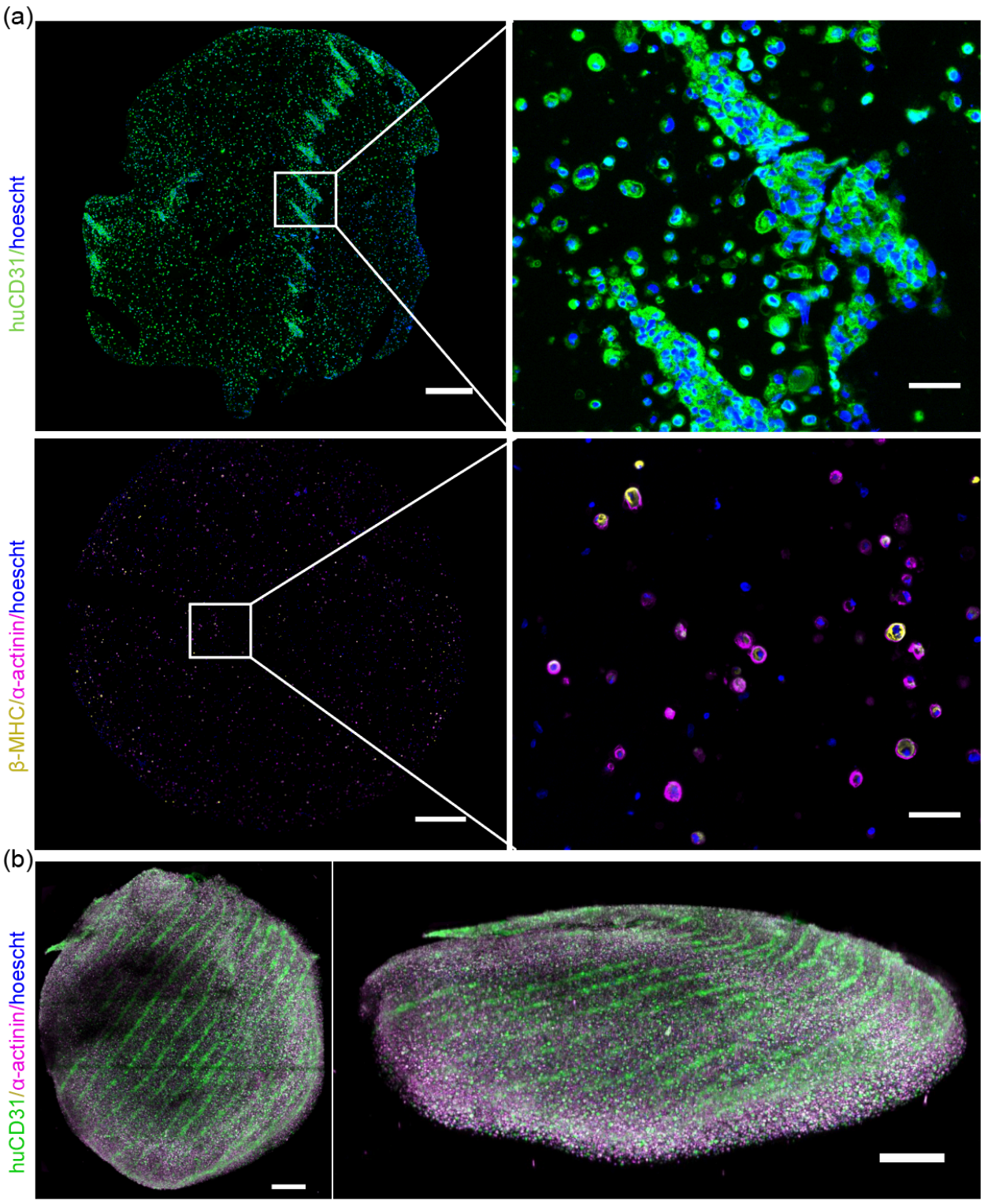

Figure 2.10. In vitro characterization of track-containing patches prior to implantation.

(a) huCD31 (green) and hoechst (blue) staining reveals patterned tracks in fibrin patch pre-implantation. βMHC (yellow) and α-actinin (magenta) staining shows cardiomyocytes in a fibrin patch pre-implantation, scale bar = 500μm.
(b) 3D visualization of an optically cleared fibrin patch stained with CD3, α-actinin, and Hoechst. Scale bar = 500μm.

Upon retrieval of the tissues 10 days post-implantation, we found that the explanted tissues from mice had evidence of guided vascularization, with Hematoxylin & Eosin and Sirius Red/Fast Green staining showing large blood-filled lumens in a linear pattern reminiscent of track cross-sections and Sirius Red staining confirming these were associated with collagen tracks, similar to our previous results (Fig. 2.11a). In contrast, tissues recovered from rats had no evidence of tracks-associated blood consolidations (Fig. 2.11a). Instead, most of the tissue was replaced by a collagen matrix in rats, with >3-fold more collagen found in tissues in rats compared to those in in mice (Fig.2.11b). While little fibrin remained in rat explants, the tissues recovered from mice contained primarily Eosin-stained fibrin, with some collagen present at the graft-host boundary and within the tracks (Fig. 2.11a). We also noted substantively more Hematoxylin-positive nuclei, indicative of an inflammatory response, in the tissues recovered from athymic rats compared to mice (Fig.2.11a, b).

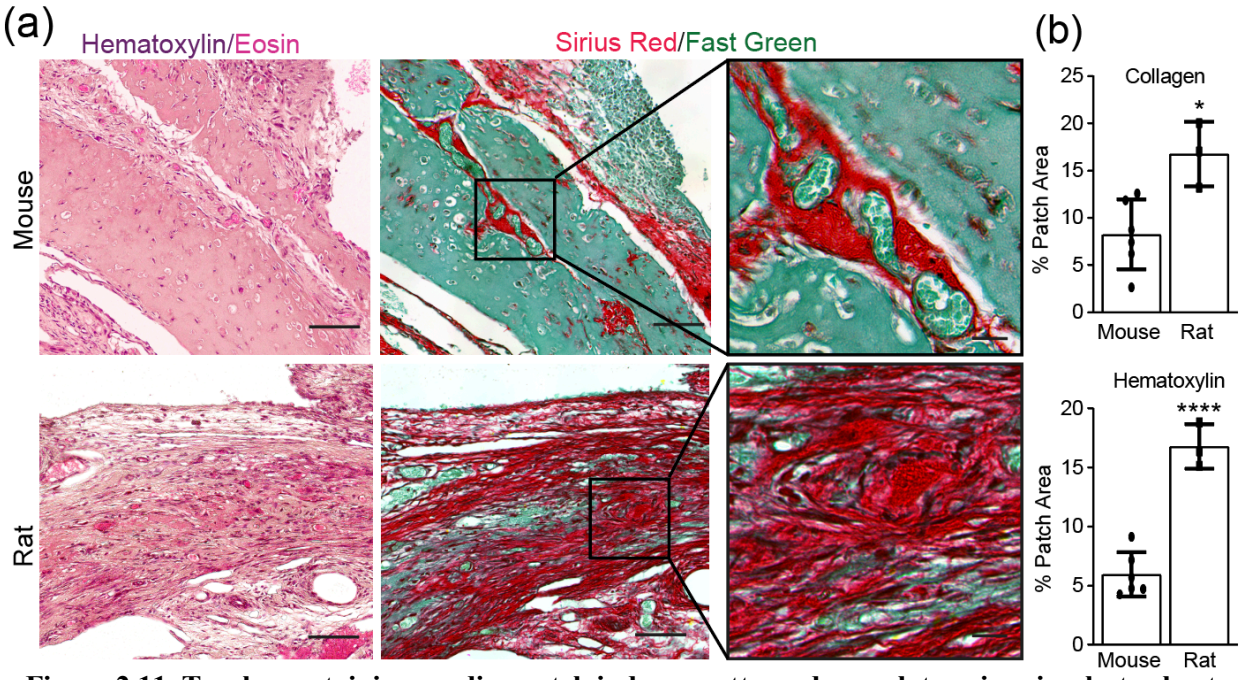

Figure 2.11. Tracks-containing cardiac patch induces patterned vasculature in mice, but robust inflammation in rat at 10 days post-implantation.

(a) H&E and Sirius Red/Fast Green show hematoxylin-positive nuclear infiltrate and SR+ collagen in patches implanted in rats, but minimal inflammation in mice. Dashed line indicates host-graft boundary. Patches in mice have blood pools associated with tracks (inset). Scale bar = 100μm. Inset scale bar = 20μm. (b) Quantification of collagen and nuclei as percent of patch area in rats and mice. Error bars report S.D. n = 6 (mice) n = 3 (rats).

Finally, we performed immunostaining to identify human graft-derived endothelial cells and cardiomyocytes in explanted tissues from the two animal models. Immunostaining revealed that tracks-containing patches in mice had distinct clusters of huCD31+ lumens that contained TER-119+ mouse blood, whereas the tissues explanted from rats had no discernible patterning of graft-derived cells (Fig.2.11c). However, immunostaining for rodent specific endothelium in explanted tissues from both animal models showed no significant differences in host-derived vasculature (Fig. 2.12).

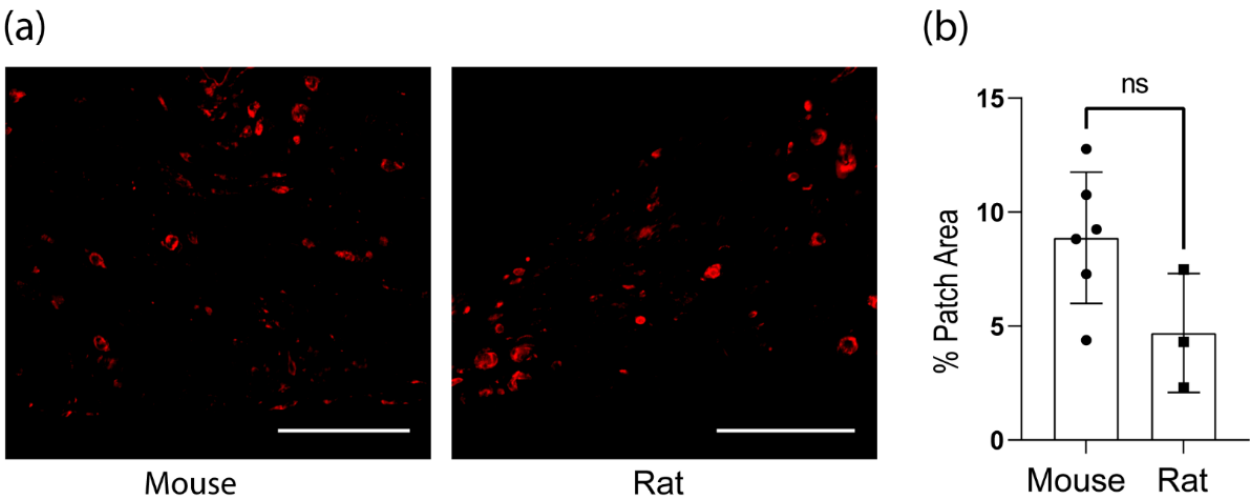

Figure 2.12. Mouse and Rat track containing patches stained for rodent specific lectins.

(a) 10-day mouse (n=6) and rat (n=3) patches stained with rodent specific lectins. Scale bar = 500µm.
(b) Quantification of rodent specific lectin as % patch area.

To further assess human cardiomyocyte graft size within explanted tissues, we stained for human myocardium with β-MHC (Fig.10d). Interestingly, grafts explanted from athymic rats were >3-fold larger grafts explanted from mice (Fig.10b). Morphologically, β-MHC cells in the tissue grafts explanted from rats were closely packed with larger cells that sometimes appeared elongated, while cells in the grafts in mice were isolated and small with a rounder, more punctate appearance (Fig.10 d, inset). Thus, while vascular patterning was retained in mice but disrupted in rats, cardiomyocyte engraftment as measured by overall graft size was paradoxically superior in rats despite apparent inflammation. These surprising results indicate a major variable that has been previously overlooked by our field, by demonstrating that identical tissues, when implanted in different host model systems, will yield vastly different engraftment results.

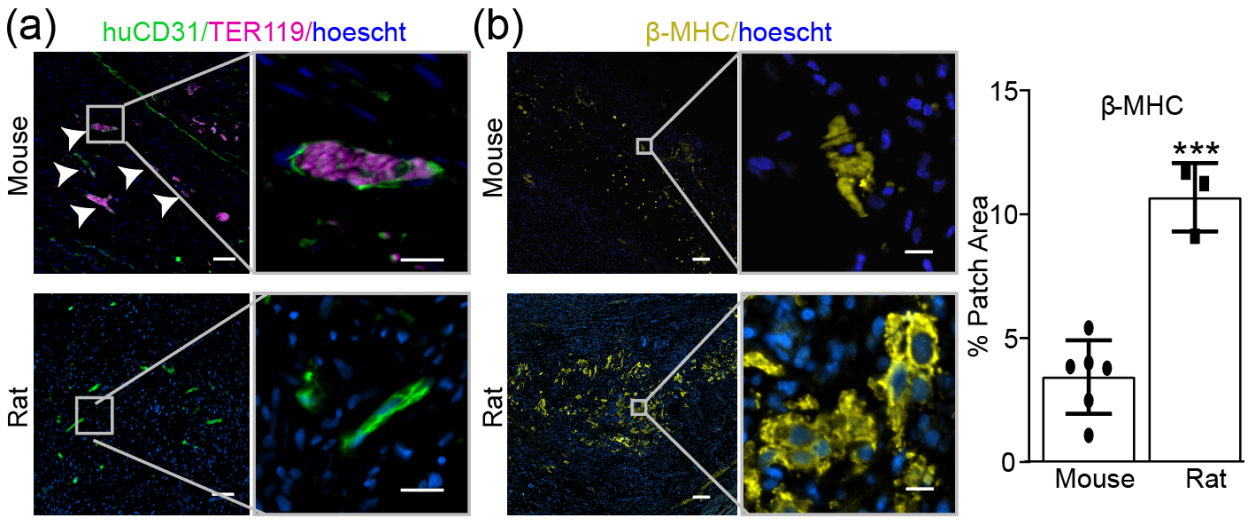

Figure 2.13. Immunostaining of tracks-containing cardiac patches induces patterned vasculature in mice, but improved cardiomyocyte engraftment in rat after 10 days.

(a) In mice, huCD31 staining reveals tracks-associated clusters of graft-derived vessels filled with TER-119+ blood (white arrows indicate tracks). huCD31 staining in rats fails to recapitulate tracks patterning. Scale bar = 50μm. Inset scale bar = 20μm.

(b) Human cardiac graft size is larger in rats than mice. Scale bar = 100μm. Inset scale bar = 10μm.

(c) Quantification of human myocardium as percent of patch area in rats and mice. Error bars report S.D. n = 6 (mice) n = 3 (rats).

2.3 DISCUSSION

We previously demonstrated that endothelial cell "tracks" encapsulated in a fibrin-based tissue guide the formation of host-perfused vessels along the axis of each track in athymic mice[12]. However, when we attempted to replicate this strategy in a cardiac patch implanted in athymic rats, the tracks led to only transient vessel patterning. In addition to loss of vessel patterning, we also observed a robust immune response leading to patch degradation and collagen deposition. Here, we meticulously assessed how host variables – anatomic implant location and animal model – differentially support guided vascularization and cardiac engraftment.

We first postulated that anatomic implant location may be the major variable at play in our studies, as others have reported a particularly robust immune response to biomaterials implanted in the epicardial environment compared to other anatomic locations. For example, Kellar et. al implanted collagen discs epicardially in mice and found increased leukocyte recruitment, inflammatory cytokine expression, and matrix degradation compared with subcutaneous implants[27]. Similarly, ePTFE discs implanted epicardially in rats showed increased immune cell density compared with either subcutaneous or abdominal implants[28]. Interestingly, we found no differences in tissue morphology or vascularization between engineered tissues with EC "tracks" implanted in either the IP space or on the heart in nude mice. We speculate that our failure to detect a difference between implant locations here could be explained by strain differences in immune response of athymic nude mice, as previous studies reporting increased inflammation in in epicardial implants have used immune-competent strains such as C56Bl/6 mice. The discrepancies between such studies thus may once again highlight the role for host factors and model systems as playing a role in tissue engineering outcomes.

Having found that athymic nude mice support guided vascularization in epicardial implants, we next sought to apply this strategy in the context of cardiac tissue engineering. By comparing engineered cardiac tissues with and without EC tracks, we found that patches with EC tracks more efficiently recruit host blood compared with unpatterned control and that patterning endothelial cells in this way may allow control over vessel size *in vivo*. Additionally, a portion of track-derived blood vessels were associated with α-SMA+ pericytes, a marker of mature vessel phenotype. We speculate that these pericytes are derived from the mouse mesenchymal cell line (CH310T1/2) incorporated within the tracks, as others have shown can occur within a pro-vasculogenic environment[29].These results represent a step forward towards replicating the

hierarchy of natural vascular networks in permissive host settings *in vivo*, as guided vascularization led to the formation of larger vessel "trunks" with lumen diameters of 20-40μm with smaller 5-15μm vessels formed "branches".

While we had confirmed that guided vascularization can be used successfully for cardiac tissue engineering applications in an appropriate host (athymic mouse), we still had not explained why this technique failed to perform similarly in the athymic rat heart[16]. To answer this question, we directly compared human cardiac tissues with EC tracks implanted epicardially in either athymic mice or athymic rats. We found that guided vascularization occurred only in athymic mice, whereas tissues in athymic rats instead exhibited signs of inflammation. Despite this failure of guided vascularization, rats supported larger human cardiac grafts compared to patches implanted in mice, indicating that vascularization and cardiomyocyte engraftment require different host environments. These data suggest that in the future, host factors could potentially be leveraged to improve engraftment of vascular or parenchymal cells such as cardiomyocytes.

Based on the dramatic difference we observed in inflammatory response between these models, we speculated that a heightened innate immune response in the athymic rat heart may promote cardiomyocyte engraftment while interfering with vascularization. Athymic nude mice and athymic nude rats both lack mature T lymphocytes, but retain other immune cell types including macrophages, neutrophils, dendritic cells, NK cells, and B cells. Despite their apparently similar immune systems, differences in immune function between these models has been reported[30,31]. For example, while NK cell activity is elevated in both athymic rodent models, athymic rats have very high NK activity in the peritoneal cavity, whereas athymic mice have relatively low peritoneal NK activity[32]. It is possible that this animal model difference

could explain our finding that abdominal tracks implants remained intact in the mouse abdomen but were obliterated in the rat. In addition to heightened NK activity, enhanced macrophage activity has been reported in both athymic mice[33] and athymic rats[31]. Mounting evidence points to the critical role of innate immunity in cardiac regenerative medicine[34,35]. In fact, recent groundbreaking work has suggested that the success of cellular therapies in the heart is primarily explained by the macrophage-predominant immune response induced by these therapies[35]. We thus speculate that a heightened innate immune response in athymic nude rats compared to athymic nude mice contributed to superior cardiomyocyte engraftment while interfering with vessel patterning[35].

Taken together, our results suggest that tissue engineering and cellular therapy fields would benefit from paying more careful attention to understanding and tuning host environment to achieve clinical success and ensure reproducibility. A challenge across biomedical research is the widespread replication crisis, which wastes limited resources, erodes public confidence in science, and impedes progress towards clinical translation[36]. Within tissue engineering and regenerative medicine, the neglected role of host biology may contribute to the high rate of pre-clinical failure and irreproducible findings[37]. This is likely particularly important in the pre-clinical development process, as new technologies are typically tested in increasingly larger animal models prior to human clinical trials. We suggest that increased attention to host biology could improve reproducibility and accelerate clinical translation of regenerative therapies, and potentially even be deployed to greatly enhance the efficacy of regenerative engineering strategies.

2.4 METHODS

2.4.1 *Cell culture and fabrication of tracks patches*

Human Umbilical Vein Endothelial Cells (Lonza, P4-P6) were cultured in EGM-2 media (Lonza) on tissue culture treated poly(styrene). Mouse mesenchymal cells CH310t1/2 (ATCC, P5-P7) were cultured in low glucose Dulbecco's Modified Eagle's Medium (DMEM) supplemented with 10% v/v fetal bovine serum (FBS, BioWest). Normal Human Dermal Fibroblasts (Lonza, P5-P7) were cultured in DMEM supplemented with 10% FBS. Media was replaced every 48 hours and cells were passaged or used for experiments at 80% confluence. Patches containing endothelial tracks were fabricated as has been previously described[12]. Briefly, HUVECs and CH310t1/2 cells were resuspended in a 2.5% collagen solution and introduced into a PDMS mold containing channels 150μm wide. Excess collagen was aspirated from the mold leaving the cell/collagen mixture only in the channels. Collagen polymerization was achieved by incubating the filled molds at 37°C for 8 minutes. Following polymerization, molds were incubated with EGM-2 media at 37°C for 3 hours to allow track formation. Tracks were then removed from the mold by encapsulating in a 1:1 mixture of 20mg/mL fibrinogen (Sigma) and 2.5U/mL thrombin (Sigma) that was allowed to polymerize. Last, a 6mm biopsy punch was used to punch out patches for implantation. Patches were then kept on ice floating in sterile EBM-2 (no supplements) until implantation.

For all cardiac patches, hPSC-CMs were prepared for implantation with heat-shock[38] and a pro-survival cocktail[39]. 24 hours prior to implantation, cardiomyocytes were changed to RPMI/BSA/Ascorbic acid that had been pre-warmed to 42°C and plates were incubated for 30 minutes at 42°C. After 30-minute heat shock, media was changed to RBA supplemented with

100 ng/mL IGF-1 (Peprotech) and 200nM Cyclosporine A (Wako). The next day, 1 hour prior to trypsinization, media was changed to RBA supplemented with pro-survival cocktail (100ng/mL IGF-1, 200nM Cyclosporine A, 10μM ZVAD-FMK (Calbiochem), 50nM TAT-BH4 (Calbiochem), 50μM pinacidil monohydrate (Sigma)). Immediately before the track encapsulation step, $2x10^6$ hCMs and $5x10^5$ NHDFs were collected and resuspended in 300μl fibrin for each tracks mold. For groups with HUVECs in the bulk, $1x10^6$ HUVECs per mold were also mixed with hCMs and NHDFs. The pooled cells were then resuspended in 20mg/mL fibrinogen and mixed thoroughly in a 1:1 ratio with thrombin to encapsulate cells in the bulk surrounding the tracks. After fabrication, patches containing cardiomyocytes were kept on ice floating in sterile EBM-2 supplemented with pro-survival cocktail supplements described above. Please see Table 1 below for detailed description of cells in the bulk gel for each experiment.

	Tracks	**HUVECs (bulk)**	**hPSC-CMs (bulk)**	**NHDFs (bulk)**
Mouse (Fig. 2.1-2.3)	Yes	No	No	No
Mouse tracks (Fig. 2.4-2.6)	Yes	No	6.67×10^6/mL	1.67×10^6/mL
Mouse bulk (Fig. 2.4- 2.6)	No	3.33×10^6/mL	6.67×10^6/mL	1.67×10^6/mL
Mouse tracks + bulk (Fig. 2.4-2.6)	Yes	3.33×10^6/mL	6.67×10^6/mL	1.67×10^6/mL
Mouse (Fig. 2.11-2.13)	Yes	3.33×10^6/mL	6.67×10^6/mL	1.67×10^6/mL
Rat (Fig. 2.11-2.13)	Yes	3.33×10^6/mL	6.67×10^6/mL	1.67×10^6/mL
Rat (Fig. 2.7-2.9)	Yes	No	No	No

Table 2.1: Cell types contained in patches for each experiment.

3.4.2 *Maintenance and differentiation of stem cells*

Human PSCs (WTC-11 or H7, Coriell) were maintained with mTeSR-1 media (Stemcell Technology) on Matrigel (BD Biosciences). Directed differentiation to cardiomyocytes was achieved through modulation of the Wnt pathway using small molecules[40]. Briefly, on day 0 hPSCs were changed to mTesR with 1μM Chiron 99021 (Tocris). After 24 hours, media was changed to Roswell Park Memorial Institute (RPMI) 1640 media supplemented with B27 (minus insulin) containing 1μM Chiron 99021. 48 hours later, media was replaced with RPMI/B27(minus insulin) with 2μM Wnt-C59 (Fisher). After 48 hours, media was changed to the final cardio maintenance media, comprised of RPMI with B27 supplement containing insulin. Thereafter, media was replaced every 48 hours. Between day 14 and 21, lactate selection with DMEM (no glucose) supplemented with 4 mM sodium lactate was performed for 72 hours, after which cells were returned to cardio maintenance media (RPMI/B27)[41]. Cardiomyocytes were used for experiments either directly following differentiation or were frozen and thawed for later use.

2.4.3 *In vivo implantation in mice and rats*

For all mouse experiments, male athymic nude mice (Taconic, 8-10 weeks), were used. Male athymic nude Hsd:RH-Foxn1rnu rats (Envigo, 150-220g) were used for rat studies. Sample size was determined prior to each experiment by reviewing the sample sizes required for statistical significance in similar published studies. For supra-epicardial patch placement, anesthesia was induced with either 5% isoflurane (rats) or ketamine/xylazine (130 mg/kg Ketamine, 8.8 mg/kg Xylazine, mice) preceding orotracheal intubation. Rats were maintained on 2% isoflurane and mice were supplemented with 0.5% isoflurane. The chest was opened via left

lateral thoracotomy and the pericardium was removed to expose the heart. For rats, two 6mm patches were affixed using 8-0 suture to the supra-epicardial surface. Due to their smaller heart size, mice received one 6mm patch similarly affixed with 8-0 suture. The chest was closed, and animals were provided analgesia for the first two post-operative days via subcutaneous injection of slow releasing buprenorphine (1mg/kg). For animals that received patches containing cardiomyocytes, daily injections of Cyclosporine A (5mg/kg) were administered beginning one day prior to implantation to promote cardiomyocyte survival actracking to previously published pro-survival protocols[39].

Animals receiving intra-peritoneal implants were induced with ketamine/xylazine (mice, 130 mg/kg Ketamine, 8.8 mg/kg Xylazine) or 5% isoflurane (rats) and a midline abdominal incision through the skin and peritoneum A single 6mm patch was affixed with 5-0 suture to the gonadal fat pad. The incision was closed, and analgesia was provided for two days via slow releasing buprenorphine. Mice for IP experiments were harvested at day 3 or day 7 (Fig.1 and S1) and rats for IP experiments were harvested at day 7 (Fig.6). All animal procedures were approved by the University of Washington Institutional Animal Care and Use Committee (IACUC protocol #4388-02).

2.4.4 *Tissue harvesting, processing, and 2D histology*

Animals were sacrificed at the pre-determined endpoint for each experiment (3, 7, or 10 days for mice; 10 days for rats). For mice receiving fluorescent lectins, 200µl of a 1:1 mix of Dylight-649 conjugated Lycopersicon Esculentum (Tomato) Lectin (1mg/mL, Vector Labs) and Dylight-649 conjugated Ulex Europaeus Lectin 1 (1mg/mL, Vector Labs) was introduced via intravenous injection and allowed to circulate for 10 minutes prior to sacrifice. Tissues were

fixed with 4% paraformaldehyde solution for 48 hours and immediately used for whole tissue staining, clearing, and 3D imaging (see below), or progressively dehydrated for paraffin embedding. Paraffin blocks were sectioned at 5μm with a microtome and sections collected on charged slides. Hematoxylin and Eosin (Harris hematoxylin and Eosin Y, Sigma) was used to visualize tissue morphometry. Collagen was identified with Picrosirius red (Direct Red 80, Sigma) using Fast Green (Sigma) as a counterstain. Prior to immunostaining, heat mediated antigen retrieval in pH 6.0 sodium citrate was performed. After blocking with 5% normal goat serum, primary antibodies were incubated at 4 degrees using antibodies against human CD31 (1:20, Dako), TER-119 (1:100, BD Biosciences), α-Smooth Muscle Actin (1:100, abcam), beta-myosin heavy chain (hybridoma supernatant, ATCC #CRL-2046, full strength), and 1:200 Dylight-649 conjugated Lycopersicon Esculentum (Tomato) Lectin (1mg/mL, Vector Labs) followed by species-appropriate secondary antibodies conjugated to Alexa Fluor 488, AlexaFluor 555, or Alexa Fluor 647. Nuclei were visualized with 1:500 Hoescht 33342. Fluorescent images were acquired on a Nikon Eclipse Ti inverted microscope with either Photometrics CoolSNAP HQ2 camera for widefield images, or Yokogawa W1 spinning disk confocal head and Andor iXon Life EMCCD camera for confocal images. Images of H&E and Sirius Red stains were obtained from whole slide scans acquired with an Aperio ScanScope AT2 digital whole slide scanner or with a Nikon Eclipse Ti inverted microscope.

2.4.5 *Clearing and 3D Imaging*

Following fixation, whole tissues (gonadal fat pad or heart) were incubated for 6 hrs at 37°C in a blocking solution (0.1M Tris, 1% BSA, 1% Normal Donkey Serum, 0.3% triton x-100) followed by 24-hour incubation with 1:100 anti-human CD31/PECAM-1 DyLight 550 conjugated antibody (Clone: JC/70A, Novus) at 37°C on an orbital shaker. After staining, tissues

were rendered optically transparent by clearing with the Clearing Enhanced 3D Microscopy (Ce3D) protocol at room temperature for 48hrs[42]. Cleared tissues were imaged with a Nikon Eclipse Ti inverted microscope with Yokogawa W1 spinning disk confocal head and Andor iXon Life EMCCD camera. After samples were imaged, cleared tissues were incubated with PBS overnight to remove clearing agents. Tissues were then processed for paraffin embedding and 2D histology as described above. 3D datasets were visualized with IMARIS 3D visualization and analysis software (Oxford Instruments). Fibrin patches fixed pre-implantation were incubated in a blocking solution overnight followed by a 24-hour incubation with 1:100 anti-human CD31/PECAM-1 DyLight 550 conjugated antibody (Clone: JC/70A, Novus) and 1:100 Recombinant Anti-Sarcomeric Alpha Actinin antibody (ab68167). Patches were then incubated in species appropriate secondary antibody conjugated to AlexaFluor 647 and 1:500 Hoescht 33342 overnight and subsequently rendered optically transparent by clearing with the Clearing Enhanced 3D Microscopy (Ce3D) protocol at room temperature for 24hrs[29]. Patches were imaged using a Leica SP8 confocal microscope.

2.4.6 *Quantitative Tissue Morphometry*

For all analysis, patch area was defined as the region between the surface of the host tissue (fat or cardiac) and the edge of the patch. Quantification of graft size for all stains (β-MHC, TER-119, huCD31, Hoescht, H&E, and Sirius Red) was accomplished using FIJI by applying a uniform threshold across images and measuring positive area[43]. For 2D analyses, a slide from the mid-point of the patch taken selected for quantification and the entire patch was analyzed using a composite image constructed through image stitching using built in Nikon microscopy software.

For vessel tracing and morphometry, a 250μm x 250μm x 250μm volume from the center of each patch was exported for analysis with the microvascular analysis suite Vesselucida (MBF biosciences). For the purposes of this analysis, "vessels" were defined as human CD31+ structures with continuous lumens. A semi-manual process was used for vessel tracing. First, small vessels were identified using the build in automatic tracing tool, which reliably identified vessels <10μm. Next, manual tracing was performed for all vessels not identified by automatic tracing. From these vessel tracings, the Vesselucida software generated data on vessel size for each network.

2.4.7 *Statistical Analysis*

Graphpad Prism software was used to complete all statistical analyses. For comparisons between two groups, an unpaired student t-test was performed. For analyses in which more than two groups were compared, a one-way ANOVA with Tukey's HSD as post-hoc test was used for data with equal variance, or Welch's Anova with Dunnett's T3 multiple comparison test was applied for data with unequal variance. Error bars are reported as SD.

2.5 Conclusions and future work

In this chapter, both 6mm in diameter track containing fibrin patches are used to evaluate vascularization and engraftment in different anatomical implant locations and in different animal models. One limitation of this work comes from the fabrication approach used to pattern tracks within tissues. Micromolding limits patterned tracks to a single plane and uses simple geometries. To improve the size, precision, and reproducibility of track containing tissues we next evaluate various 3D biofabrication methods to identify promising methodologies for producing large track containing tissues with complex geometries.

Chapter 3: SACRIFICIAL TEMPLATING FOR ACCELERATING CLINICAL TRANSLATION OF ENGINEERED ORGANS

Adapted from: Malkani, S*, **Prado, O***, and Stevens, K.R.S. 2025. "Sacrificial Templating for Accelerating Clinical Translation of Engineered Organs." *ACS Biomaterials Science & Engineering* 11 (1): 1–12. https://doi.org/10.1021/acsbiomaterials.4c01824. Reproduced with permission.

Transplantable engineered organs could one day be used to treat patients suffering from end-stage organ failure. Yet, producing hierarchical vascular networks that sustain the viability and function of cells within human-scale organs remains a major challenge. Sacrificial templating has emerged as a promising biofabrication method that could overcome this challenge. Here, we explore and evaluate various strategies and materials that have been used for sacrificial templating. First, we emphasize fabrication approaches that use highly biocompatible sacrificial reagents and minimize the duration that cells spend in fabrication conditions without oxygen and nutrients. We then discuss strategies to create continuous, hierarchical vascular networks, both using biofabrication alone and using hybrid methods that integrate biologically driven vascular self-assembly into sacrificial templating workflows. Finally, we address the importance of structurally reinforcing engineered vessel walls to achieve stable blood flow *in vivo*, so that engineered organs remain perfused and functional long after implantation. Together, these sacrificial templating strategies have the potential to overcome many current limitations in biofabrication and accelerate clinical translation of transplantable, fully functional engineered organs to rescue patients from organ failure.

3.1 Biofabrication of Vascular Networks

Engineered organs could one day serve as bridges or alternatives to organ transplantation, offering hope to those on long transplant waiting lists. However, for engineered organs to be clinically viable, they must be highly functional, densely cellularized, and incorporated into host circulation[44–46]. A major challenge in meeting these therapeutic requirements is fabricating the vascular networks that are needed to support oxygen and nutrient delivery to parenchymal cells. In most situations, these vascular networks must recapitulate human vascular architecture, integrate seamlessly with host circulation, and withstand hemodynamic forces after transplantation.

Striking advances in biofabrication have brought us closer to replicating the complex, multi-scale architecture of human vasculature. Many of these advances were achieved by adapting 3D printing technologies such as extrusion printing, inkjet printing, and stereolithography to be compatible with soft, hydrated, and/or biological materials (*e.g.,* hydrogels and cells)[47–49]. In extrusion bioprinting, biomaterials are extruded through a nozzle via pneumatic or physical pressure, forming filaments that build up a 3D structure[46,50,51]. Inkjet bioprinting employs thermal or piezoelectrical pulses to dispense droplets of biomaterials, making up 3D structures[52,53]. Stereolithography cures photopolymerizable materials by exposure to specific wavelengths of light[54]. Digital light projection (DLP), a form of stereolithography, uses slicing software to generate photomasks of light and dark pixels that are then projected over entire x-y planes, rapidly patterning 3D structures into large volumes[44,54–57]. Collectively, these techniques have enabled bioprinting of rudimentary vascular networks within biocompatible hydrogels containing live cells[58–63].

3.2 Sacrificial templating for producing physiological-scale organs

Despite the incredible progress made in bioprinting, much of this field still faces significant challenges in maintaining cell viability during fabrication of large tissues. This is largely because during many biofabrication processes, cells experience extended periods of time in suspension and in partially fabricated engineered tissues without a functional vascular network. Thus, the cells often experience hypoxia during fabrication, which can lead to irreversible cell damage[64,65]. Moreover, many bioprinting technologies also expose the tissue to additional stressors. Extrusion bioprinting can subject cells to shear stress as they are forced through small diameter nozzles[52,66–69]. Inkjet bioprinting can introduce shear and impact forces during ejection and landing of the droplets as well as high temperatures in thermally actuated approaches[52,69,70]. Conversely, DLP introduces minimal shear forces but exposes cells to ultraviolet or blue light and reactive oxygen species, which can cause DNA damage and lead to cell death or misrepair[52,69,71–73].

Additionally, most bioprinting strategies are still limited by material constraints and slow speeds of fabrication. To bioprint complex architectures such as vasculature with high precision, materials with relatively high Young's modulus (stiffness >60 kPa[54,74]) are required to achieve the necessary resolution and design fidelity during and after fabrication, and to prevent ruptures when the channels are perfused. These materials are often stiffer than human organs, which can inhibit vascularization and parenchymal function[75–83]. Importantly, most bioprinting processes are typically very slow. Fabricating a single bioprinted organ of human physiological scale takes many hours or even days[84], subjecting the cells to extended hypoxia and time in suspension. All in all, this means that cellular damage accumulates during fabrication pipelines – starting from

the time of cell collection until the engineered tissue is finished and perfused – massively limiting bioprinted organ functionality and therapeutic potential.

Sacrificial templating offers a potential solution to these major challenges by shielding living cells from detrimental fabrication conditions[45,52]. This approach uses "sacrificial" materials as inks to produce 3D vascular-mimetic templates. Various 3D printing or bioprinting technologies can be used to fabricate the sacrificial templates. The resultant sacrificial templates are later removed, leaving hollow perfusable vascular networks in a cellularized hydrogel matrix (Fig.1). These hollow lumens can then be seeded with vascular cells to form an endothelial barrier[85] and can be perfused to increase oxygen and nutrient delivery to the surrounding tissue. Notably, to achieve proper barrier functionality and replicate physiological blood-tissue exchange, channels may need to be lined with concentric layers of collagen, elastin, smooth muscle cells, and endothelial cells, as found in native vessels[44]. However, this is still challenging in the field and is often beyond the scope of biofabrication studies. As such, we refer to biofabricated channels containing endothelial cells as engineered vasculature below, with the caveat that the extent to which such 'vasculature' will remain functional under the physiological flow conditions in human organs has yet to be determined. Here, we explore some capabilities, challenges, and remaining questions that arise in the pursuit of building transplantable organs using sacrificial templating.

3.3 Biocompatibility considerations of sacrificial templating methods

3.3.1 *Coupled vs decoupled*

To evaluate the biological impacts of sacrificial fabrication approaches, one particularly important question is: At what point do the cells enter the process? Towards this end, we broadly

separate sacrificial techniques into two groups: coupled *vs.* decoupled methods (Fig. 3.1). The major distinction between these two methods is the duration of cell exposure to fabrication stressors.

For coupled methods, the sacrificial template and cellularized hydrogel matrix are patterned simultaneously. For example, sacrificial materials have been extrusion printed directly within a cellularized hydrogel precursor to pattern vascular networks[86,87]. After polymerization of the hydrogel, the sacrificial material is removed to leave hollow vascular networks. Others have developed multi-material approaches using extrusion printing[88,89] or DLP[90] to simultaneously pattern sacrificial and non-sacrificial inks. These coupled methods, where the sacrificial material is patterned along with the matrix and cells, allowed for the use of more physiological matrix stiffnesses and cell densities for the non-sacrificial ink. However, cells still accumulate damage due to hypoxic and suspension conditions during the course of fabrication. That is, the larger the tissue, the longer the fabrication process takes, extending the duration that cells experience hypoxia. As a result, the maximum size of bioprinted tissues and organs achievable is determined largely by the speed of fabrication. Thus, for coupled approaches, fabrication time and engineered tissue size must be limited to avoid damaging the cells.

Decoupled methods avoid this obstacle by fabricating the sacrificial template first, without cells being present. For decoupled methods, sacrificial inks are first printed to produce a vascular-mimetic template that is free-standing and retains its architectural features without needing a secondary support bath or gel. The resultant free-standing sacrificial templates can then either be stored under controlled conditions or directly encapsulated in cellularized hydrogels. For embedding, the cells and matrix are simply casted and cured around the sacrificial

template in one quick step (<15 minutes), minimizing hypoxic and suspension conditions for the cells. The template is then removed to leave hollow vascular networks.

Common decoupled approaches include fabricating the sacrificial templates via molding[91,92], droplet-based inkjet bioprinting[53,93], extrusion bioprinting[94–101], electrospinning[102,103], injection molding[104,105], and selective laser sintering[85]. For these methods, the time the cells spend in hypoxia is determined predominantly by how fast the sacrificial template can be removed (typically minutes), as opposed to how fast it can be fabricated (typically hours for large tissues). Thus, decoupled approaches truly shield the cellularized matrix from detrimental fabrication conditions, which may enable arbitrarily large tissues to be fabricated. Additionally, since the cells are not present during fabrication, there is less of a constraint to how long template fabrication can take, which enables use of higher precision fabrication methods. These distinctions are key as the field aims to maximize the function and therapeutic potential of engineered human tissues.

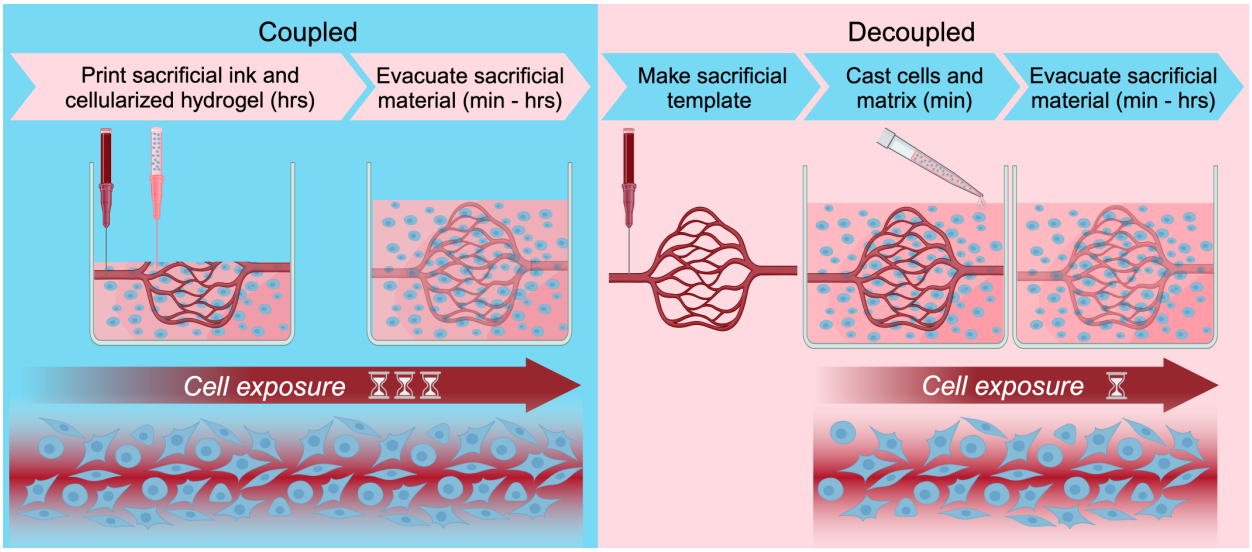

Figure 3.1. Coupled vs decoupled sacrificial fabrication.

Coupled sacrificial approaches pattern sacrificial materials and removable vascular structures in parallel,

exposing cells to extended fabrication durations (left). Decoupled sacrificial approaches limit cell exposure to fabrication conditions by first fabricating the removable vascular templates (right).

3.3.2 *Mechanism of the sacrificial agent*

A key consideration for sacrificial templating is the choice of sacrificial material and conditions required for evacuation. This choice is important for several reasons. First, different sacrificial materials vary massively in their biocompatibility and potential toxicity. This not only affects cellular viability and organ function but will also be important in navigating regulatory hurdles during the clinical translation process. Second, sacrificial materials have different mechanisms of evacuation. These mechanisms vary greatly in both the speed with which the sacrificial material can be removed as well as the biocompatibility of the removal reagents, both of which can impact cellular viability and function.

These considerations are particularly important for coupled methods, in which cells are present during the fabrication process. In these methods, exposure to extreme temperatures, harsh reagents, chemical byproducts such as free radicals, and extended time in suspension[44,45,56,106,107] during fabrication can greatly impact cell viability and function. While decoupled sacrificial templating methods circumvent some of these concerns since cells are not present during fabrication, the sacrificial material may still interact with cells during the casting and sacrificial template removal process. As such, the evacuation conditions, as well as any residual sacrificial material left behind in the construct, may still affect the cells. Some strategies to create and remove sacrificial templates include the use of water-soluble materials, thermoreversible materials, and pH- or ion-dependent reversible crosslinking (Table 1). Each of these approaches vary in their cell and tissue matrix compatibility. Here, we will discuss each of these strategies in more detail.

Sacrificial material types	Examples	Advantages	Limitations
Water-soluble	Sintered isomalt[85] Inkjet printed ice[93]	Decoupled fabrication Biocompatible reagents Fast evacuation	Limited flexibility with tissue matrix composition
Thermoreversible	Extruded Pluronic F127[108] Inkjet printed gelatin[89]	Biocompatible reagents Fast evacuation	Usually coupled fabrication Limited flexibility with tissue matrix composition Low resolution
pH and ion-dependent	Wet spun alginate[109] Melt spun shellac[102]	Decoupled fabrication Compatible with wide range of tissue matrix compositions High resolution	Moderate biocompatibility Slow evacuation
Synthetic polymers and resins	Extruded PLA[99] Injection molded PCL[105]	Decoupled fabrication Ability to form complex, biomimetic architectures High resolution	Poor biocompatibility Limited flexibility with tissue matrix composition Slow evacuation

Table 3.1: Sacrificial templating methods.

Water- or saline- soluble materials such as polyvinyl alcohol (PVA)[96–98,110], poly(ethylene oxide) (PEO)[111,112], sugar[85,95,113,114], and ice[93] have been used in decoupled sacrificial methods. To do this, these materials can be extruded or selectively laser sintered to fabricate stand-alone templates of vascular geometries. Cells and hydrogels are cast over the templates, and the templates are subsequently dissolved and flushed out with saline. A huge benefit of these approaches is the ability to leverage materials that are already present in our bodies, such as water or sugar, and thus these materials are likely to be particularly biocompatible, ensuring high cell viability during evacuation. However, some water-soluble

templates may be too readily dissolved when warm, aqueous hydrogels are cast around them, leading to template warping and loss of patterning before the surrounding matrix polymerizes. As such, these templates are incompatible with cellularized tissue materials that require warm temperatures or extended polymerization times.

The thermoreversible behavior of certain natural and synthetic hydrogels provides another route to sacrificially pattern channels. These materials are more commonly used in coupled methods, where they are extruded into a cellularized matrix and then removed by manipulating temperature and flushing the tissue with saline. Thermoreversible materials can also be used in decoupled approaches, where they are extruded to form free-standing templates. However, this is less common as these materials are often too soft to maintain their architectures without support[115]. Some hydrogels, like gelatin and agarose, gel at cooler temperatures and become liquid at higher temperatures. Other materials, such as Matrigel, fibrinogen, Pluronic F127 and poly(N-isopropylacrylamide) (PNIPAM), gel at higher temperatures and become liquid at lower temperatures. As such, sacrificial gelatin[88,91,101] structures are evacuated by increasing the temperature to 37°C, causing the gelatin to become fluid and easy to be flushed out with warm saline or cell media. Conversely, sacrificial materials such as Pluronic F127[102,108] and PNIPAM[102,103,116,117] are removed by lowering the temperature to 4°C until these materials become liquid and can be flushed out with cold saline or cell media. Similarly to water-soluble materials, these thermoreversible materials are relatively biocompatible because the sacrificial templates can be removed without harsh evacuation reagents. That said, for materials that are not found in the human body, their introduction into the fabrication process could generate additional regulatory hurdles that would ultimately need to be navigated. Furthermore, due to the

temperature sensitivity, the aqueous and curing temperatures of the surrounding matrix must be opposite to those of the sacrificial template, thereby restricting tissue matrix choices.

Additionally, pH- and ion-dependent reversible crosslinking have been utilized to create sacrificial templates. These are often used in decoupled methods, such as electrospinning, wet spinning or melt spinning to create free-standing templates of vascular networks. Shellac[102,117] is a pH responsive resin that can be used to patterned vasculature into engineered tissues. This has been demonstrated through melt-spinning the resin into templates using a cotton candy machine, casting a hydrogel around it, and flushing with a basic solution to remove the shellac from the tissue. Alginic acid[109,118,119] is a liquid, anionic polymer that crosslinks into alginate when exposed to divalent cations such as Ca^{2+}. Free-standing alginate templates have been formed via wet spinning or molding using calcium chloride as a crosslinker. After the surrounding tissue has been cast, the alginate templates are evacuated with a chelating agent that scavenges these divalent cations. This returns the sacrificial alginate to an aqueous state, allowing it to be flushed out. Though shellac and alginate templates have successfully been used to pattern dense microvascular networks into tissues, exposure to basic solutions or chelators for extended durations can cause damage to cells[120–122]. As such, evacuation times must be limited to maintain cell viability when using these reagents. Notably, since these templates are governed by pH- and ion- conditions, they are largely unaffected by exposure to various temperatures and aqueous conditions during matrix casting. As such, these templates are compatible with a wide range of cellularized tissue matrices.

Finally, some groups utilize synthetic polymers or resins in sacrificial templating processes, which require much harsher reagents to degrade. Polymers used in this way are polylactic acid (PLA)[99,123] and polycaprolactone (PCL)[105], which have been extensively used in

traditional extrusion 3D printing due to their thermal and mechanical properties[124,125]. The high mechanical strength of these materials allows for the formation of complex, free-standing sacrificial templates with high resolution and shape fidelity. However, they require cytotoxic reagents such as dichloromethane, acetone, and chloroform to evacuate them out of the gel. For this reason, tissues patterned with these reagents are typically seeded via perfusion or incubation with cells after evacuation of the sacrificial material is complete, and the bulk tissues are generally acellular[99,105,123]. Additionally, the organic solvents used to remove the templates may alter tissue matrix properties (*e.g.* swelling and stiffness), limiting cellularized material compatibility[126,127].

In all, there are many sacrificial materials that have been leveraged to pattern vasculature into engineered tissues. With the end goal of clinical translation in mind, it is important to consider the biocompatibility and exposure duration of all reagents and processes being used. As such, decoupled approaches, where a sacrificial template is formed first in the absence of cells, and methods that use highly biocompatible reagents and conditions, such as saline, neutral solutions, and physiological temperatures, may face fewer regulatory obstacles on the path towards clinical translation.

3.4 Architectural complexity

To form clinically useful tissues capable of physiological organ functions, we must consider the architectures we are trying to replicate. Vascular architectures serve distinct, form-derived functions that are critical to cell viability and thus overall organ function[128,129]. These architectures modulate blood pressure distribution[130,131] as well as nutrient and oxygen gradients, which provide important cues to cells that affect their metabolic state and function[132–138]. To

date, different sacrificial templating methods have achieved varying levels of architectural complexity. Here, we highlight approaches that have successfully demonstrated sacrificial fabrication of straight channels, simple junctions, and complex biomimetic structures.

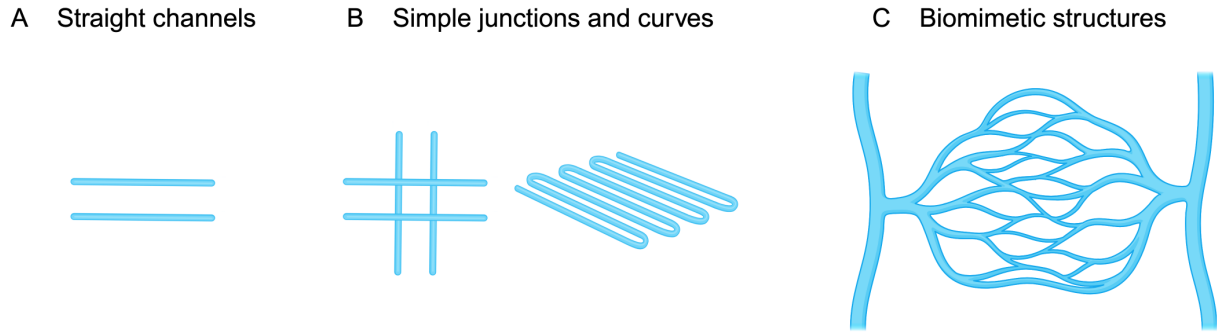

Figure 3.2. Varying degrees of architectural complexity.

(A) Straight channels achievable with simple molding or needle casting approaches.
(B) Simple junctions and curves require printing or electrospinning approaches.
(C) Biomimetic structures are the most challenging to fabricate and require more advanced printing technologies.

3.4.1 *Straight channels*

The simplest sacrificial approaches involve fiber molding or needle casting, which generates straight channels that extend all the way through a tissue (Fig. 3.2A). In these techniques, a solid needle or molded fiber is encapsulated in a cellularized matrix, and the fiber or needle is then manually pulled out to leave an empty channel[92,94,139–142] (Fig. 3.3A). For example, sacrificial agarose fibers were used to pattern channels that were then lined with endothelial cells within a cellularized gelatin methacrylate (GelMA) matrix[94]. Briefly, a layer of GelMA was first polymerized. Melted agarose was then loaded into a glass capillary tube, cooled, and pushed out onto the GelMA. After a second layer of cellularized GelMA was casted

and polymerized, the agarose fibers were manually pulled out. The hollow channels were then seeded with endothelial cells. These needle or fiber molding approaches are fast, easy to learn, and do not require many resources, allowing for quick and simple experiments. However, the architectures that can be achieved with these approaches are limited to straight channels and cannot be used to replicate physiological vascular architectures.

3.4.2 *Simple junctions*

To achieve moderately complex architectures with junctions and/or curved features with sacrificial templating (Fig. 3.2B), fabrication technologies such as bioprinting and electrospinning, are required. Architectures containing junctions or highly curved features preclude manual removal of the sacrificial material after the cellularized matrix has been cast, and instead require dissolving, degrading, or flushing to evacuate the patterned material[95,103,104,108,143] (Fig. 3.3 B). This has been demonstrated by extrusion printing of sacrificial Pluronic F127 into a 3D grid lattice, embedding of the grid lattice into a cellularized hydrogel, and evacuating the lattice by cooling and flushing with cold media[108]. While perfusion through this network importantly sustained the viability of cells in the bulk, the lattice geometry demonstrated is made up of sharp, 90° junctions that may cause turbulent fluid flow[144]. Separately, dense, microvessel networks have been formed sacrificially using wet-spun alginate[109] and melt-spun shellac[102]. However, wet-spinning and melt-spinning result in randomly oriented fibers rather than precise architectures. The inability to recreate native architectures and organ-specific microvasculature will likely negatively affect blood flow distribution across the tissue[145–148].

3.4.3 *Biomimetic structures*

To fabricate the most complex, biomimetic architectural features, such as smooth branching, 3D geometries, and scalar hierarchy (Fig. 3.2C), more advanced technologies are required. Water-soluble 3D sacrificial vascular structures with smooth branching have been achieved via selective laser sintering to make free-standing isomalt templates[85] (Fig. 3.3C-i). Similarly, others have used inkjet printing to form sacrificial ice templates with microscale resolution and smooth branching, that are later removed from the tissue by warming and flushing[93] (Fig. 3.3C-ii). Both these approaches demonstrate biomimetic architectures, but they require specialized and sometimes expensive equipment that also require expertise to operate and maintain.

Other approaches that have achieved vascular biomimetic architectures are extrusion printing of free-standing PLA templates followed by dissolution with chloroform and acetone or dichloromethane[53,93,99,123] (Fig. 3C-iii), and corrosion casting of PCL followed by dissolution with acetone[105] (Fig. 3C-iv). The PLA templates demonstrated smooth branching and diameter transitions, and the PCL templates were highly biomimetic in architecture, but a major drawback for both approaches is the need for cytotoxic evacuation reagents. In both cases, cells were seeded via perfusion or incubation after the template had been removed, resulting in acellular or sparsely seeded bulk tissues.

Additionally, organoid-laden vascularized tissues were fabricated via embedded extrusion of sacrificial gelatin within densely packed hydrogels, followed by warming and flushing out the gelatin[87]. Maintaining the viability of organoids within engineered tissues is an exciting achievement, however, extrusion is unable to form smooth branching junctions. Importantly, this coupled sacrificial process means that the cells are present during fabrication of

the sacrificial material and are subject to hypoxic conditions, thereby limiting tissue sizes achievable.

While the above methods have energized the field by approaching physiological architectures, resolution limitations still prevent most of them from capturing the full scalar hierarchy in native vasculature.

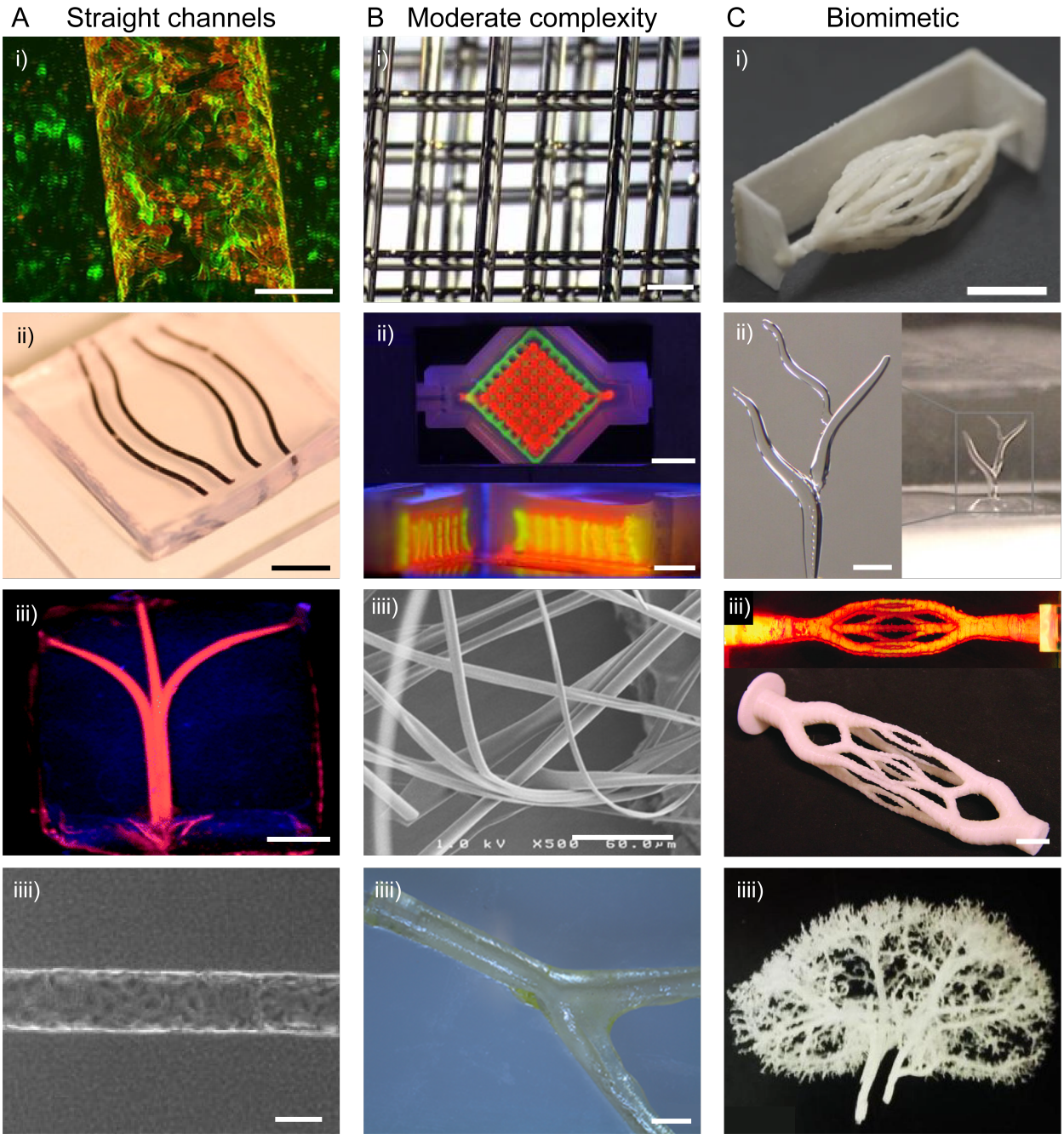

Figure 3.3. Architectures achievable via sacrificial templating.

(A) Examples of straight channels. i) A lymphatic vessels-impregnated breast cancer (LV-BC) model using sacrificial agarose. Confocal imaging of the LV-BC stained for CD31 (red) and EGFR (green). Scale bar = 250 μm. Reproduced with permission from Liu et al 2020[94]. Copyright 2020 Elsevier. ii) Sacrificial agarose fibers encased in GelMA for generating a mammary ductal carcinoma model. Scale bar = 500 μm. Reproduced with permission from Duchamp 2019[92]. Copyright 2019 Wiley. iii)

Fluorescent microbeads (pink) perfused through agarose fiber-molded channels in a GelMA matrix. Scale bar = 3 mm. Reproduced with permission from Bertassoni 2014[139]. Copyright 2014 Royal Society of Chemistry. iv) Phase contrast image of an endothelialized microscale channel in a needle-molded collagen hydrogel. Scale bar = 100 μm. Reproduced with permission from Wong 2010[142]. Copyright 2010 Elsevier.

(B) Examples of moderately complex architectures. i) Multilayered lattice of extrusion-printed sacrificial carbohydrate glass structures. Scale bar = 1mm. Reproduced with permission from Miller 2012[143]. Copyright 2012 Springer Nature Limited. ii) Photograph of a three-dimensional vascularized tissue construct fabricated with extruded sacrificial Pluronic F127. Scale bar = 5 mm. Reproduced with permission from Kolesky 2016[108]. Copyright 2016 Proceedings of the National Academy of Sciences. iii) Scanning electron microscopy image of solvent-spun PNIPAM fibers used to pattern microvasculature within gelatin hydrogels. Scale bar = 60 μm. Reproduced with permission from Lee 2016[103]. Copyright 2016 Wiley. iv) Injection-molded branched tubular scaffold. Scale bar = 2 mm. Reproduced with permission from Martin 2013[104]. Copyright 2013 SAGE Publications.

(C) Examples of complex, biomimetic structures. i) Inkjet-printed ice template and the evacuated channels in a UV-curable resin. Scale bar = 400 μm. Reproduced with permission from Garg 2022[93]. Copyright 2022 Wiley. ii) A dendritic vascular network fabricated by selective laser sintering of isomalt. Scale bar = 10 mm. Reproduced with permission from Kinstlinger 2022[85]. Copyright 2020 Springer Nature Limited. iii) Extrusion-printed PCL branched vasculature template (bottom). Patterned channels in epoxy filled with chemiluminescent dye (top). Scale bar = 10 mm. Reproduced with permission from Gergely 2015[99]. Copyright 2014 Wiley. iv) PCL vascular corrosion cast of kidney vasculature. Reproduced with permission from Huling 2016[105]. Copyright 2022 Elsevier.

3.5 Resolution and hierarchy

To accurately replicate physiological vascular structures, the hierarchy of vessel diameters must be maintained throughout the architecture. In native tissues, vessel diameters decrease at each branching point to prevent sudden drops in blood pressure, with diameters ranging from 10mm down to ~0.005mm (10mm to 5μm)[44]. Channels >1mm have been achieved via inkjet printing of ice templates[53,93], coaxial extrusion of hollow alginate fibers[118,149], and extrusion of sucrose inks[95,100,143]. Channels between 0.1mm – 1mm have been achieved via selective laser

sintering of isomalt[85], extrusion of Pluronic F127[108] and other hydrogels, and multi-material DLP printing of sacrificial hyaluronic acid methacrylate (HAMA)[90]. Finally, some of the smallest diameters (<0.01mm) have been achieved via electrospinning of shellac[117] and PNIPAM[102,103], and wet-spinning of alginate[109], however these result in randomly oriented fibers rather than organ-specific microvascular architectures, which can negatively affect blood flow distribution across the tissue[145–148]. Despite these advancements, no single fabrication method has yet demonstrated the full range of diameters seen in hierarchical vascular networks.

3.6 Leveraging self-assembly

Instead of fabricating the smallest diameter channels, some groups have leveraged the ability of endothelial cells to self-assemble into microvascular networks *in vitro* and *in vivo*[12–14,16,148,150–152]. To integrate this with sacrificial templating, meso- and macro- scale vessels can be sacrificially patterned into controlled architectures within a matrix that supports microvascular self-assembly. This was recently done using multi-material DLP printing of GelMA as the cell-laden matrix and enzyme-degradable sacrificial HAMA to pattern endothelialized channels **(**Fig. 3.4A). When high densities of human mesenchymal stromal cells were included in the GelMA, self-assembled vascular networks formed in both the patterned channels and the surrounding matrix[90]. However, perfusion has not yet been demonstrated for vessels produced using this hybrid approach.

Separately, others have built a custom inkjet 3D printer to precisely pattern collagen and sacrificial gelatin. During the fabrication process, fibrin and endothelial cells were casted between the sacrificial gelatin structures. Following removal of the gelatin, additional endothelial cells were injected into the hollow channels, resulting in a bed of self-assembled microvessels

(10–25μm) between macro-scale (500 – 1000μm) vessels. Two types of angiogenesis from the patterned channels were found – thin, quick-growing sprouts, and wide, slow-growing sprouts – both of which were found to anastomose with self-assembled vessels[89] (Fig. 3.4B). In another study, macro-scale vessels were patterned via needle molding and surrounded by a poly(l-lactic acid)/poly(lactidecoglycolide) (PLLA/PLGA) scaffold. Once the needles were removed, the macro-scale (600μm) channels were endothelialized and the scaffold was seeded with collagen and endothelial cells to promote self-assembled networks. When these tissues were implanted in mice, gels with patterned and self-assembled (20–80μm) vessels had a higher percentage of perfused vessels and improved host vessel invasion when compared to implants containing self-assembled vasculature only[153] (Fig. 3.4C). In all, these studies highlight that combining sacrificial patterning and self-assembly may enable fabrication of continuous hierarchical networks[89,90,153].

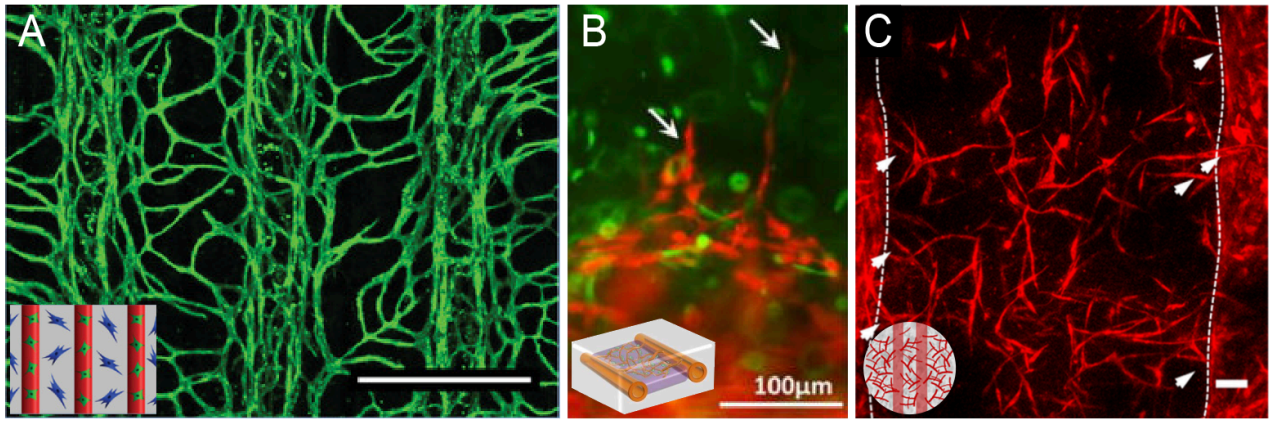

Figure 3.4. Integration of self-assembled and engineered vessels.

(A) Projection based stereolithography 3D bioprinting using a multi-material, layer-by-layer printing approach. The formation of structured microvascular networks stained for CD31 (green). Scale bar = 500 μm. Reproduced with permission from Orellano 2022[90]. Copyright 2022 Wiley.

(B) Multi-scale vascular system fabricated via 3D bioprinting demonstrating different types of angiogenic sprouts. Scale bar = 100 μm. Reproduced with permission from Lee 2014[89]. Copyright 2014 Springer.
(C) Macro-vessel templating rods in porous PLLA/PLGA form a multi-scale vascular tissue construct with microvascular endothelial cells expressing tdTomato (red). Engineered macro-vessels integrate with self-assembled vessels. Scale bar = 50 μm. Reproduced with permission from Debbi 2022[153]. Copyright 2021 Elsevier Ltd.

3.7 *In vivo* implantation

To treat patients via therapeutic engineered organ transplantation, tissues fabricated with sacrificial templating will need to be connected to host circulation. This will likely require direct surgical anastomosis of large host vessels (arteries, veins) with the inlet and outlet of the engineered organ. Importantly, after anastomosis with the patient's vessels, the engineered vasculature must be able to mechanically withstand hemodynamic forces found within the human body without bursting, leaking, or undergoing thrombosis. While some groups have performed direct anastomosis of engineered vessels to host vessels, the sacrificial templating field has yet to show stable long term *in vivo* perfusion of the tissue[100,154,155].

Achieving sustained perfusion of sacrificially templated organs is a major remaining challenge in the field. This is because most engineered tissues currently produced via sacrificial templating contain cells embedded in a relatively soft hydrogel. While these soft matrices are beneficial for parenchymal cellular function[75–83], they are unlikely to withstand hemodynamic pressures without bursting or leaking. Furthermore, most of the vascular networks fabricated, including channels the size of larger arteries and veins, are only lined with a single layer of endothelial cells. Collectively, the soft materials surrounding sacrificially templated vessels and the lack of structural reinforcement in the large vessels themselves provide minimal resistance against hemodynamic pressures. Networks currently produced by sacrificial templating thus

remain susceptible to bursting, leaking, and thrombosis when implanted and challenged with physiological human blood pressure and flow conditions[156–158].

Notably, nature overcomes this challenge in part by lining large and mid-sized vessels with concentric layers of smooth muscle cells, collagen, and elastin, which collectively provide the mechanical support necessary to withstand hemodynamic forces[44,52,156,157,159]. Intriguingly, some groups have developed sacrificial fabrication techniques to create freestanding blood vessel mimics with concentric layers of endothelial cells and smooth muscle cells within biomaterials such as collagen, alginate, GelMA, and chitosan[160–163]. These methods typically leverage radial diffusion of crosslinkers from sacrificial molds or scaffolds to create hollow blood vessel mimics. The radial crosslinking process can be repeated to create multi-layered hollow tubes, with the ability to incorporate endothelial cells in the inner layer and smooth muscle cells in the outer layers. These blood vessel grafts were developed for clinical use and *in vitro* modeling of coronary interventions such as balloons and stents. As a result, the sacrificially templated blood vessel grafts were not embedded within a cellularized matrix, thus their ability to support surrounding tissue viability and function has yet to be examined. Moving forward, integration of these technologies into decoupled sacrificial templating methods may result in reinforced vessel walls. For example, following sacrificial template removal, the hollow lumens might be sequentially lined with collagen, elastin, smooth muscle cells, and endothelial cells that organize to form functional vasculature capable of stable, long-term perfusion and blood-tissue exchange *in vivo.*

In addition to concerns about mechanical integrity of engineered vasculature due to high blood pressures, non-uniform or low pressures throughout networks can also be harmful. Low blood pressures can cause microvessels to undergo thrombosis due to collapse of small diameter

vessels and/or increased platelet adhesion and aggregation[154,164]. These can occur when the vascular architectures do not evenly distribute blood flow across the tissue and across vessels of different scales[130,148]. Microvessel networks fabricated with randomly oriented fibers are particularly susceptible to this issue, since recapitulation of organ-specific microvascular architectures is precluded[145–148]. Collectively, the field will need to solve these challenges before engineered organs produced by sacrificial templating can be used safely to treat patients with acute organ failure.

3.8 Conclusions and perspectives

Sacrificial templating is a highly promising avenue for achieving continuous hierarchical vasculature to support engineered tissues. While significant technological advancements have been developed, questions remain around the optimal degree of complexity required to engineer functional vasculature within artificial organs. For instance, how much patterning is truly necessary, what architectures and scales are required, and how much can self-assembly take care of? Furthermore, how can the anastomosis between patterned vasculature and self-assembled vessels be controlled, improved, or sped up? And finally, how can we line sacrificially templated vasculature with concentric layers of extracellular matrix materials and smooth muscle cells to ensure proper endothelial barrier function in implanted tissues without leaking, bursting, or thrombosing under physiological blood pressures?

Materials and material removal agents currently being used for sacrificial templating range from very benign, natural biomaterials to synthetic materials that can achieve more complex architectures and higher resolutions, at the expense of biocompatibility due to harsh solvents used and extended evacuation times. When incorporating self-assembly into engineered tissues,

the required fabricated architectures and resolutions may lie in the middle of the complexity spectrum, likely more advanced than simple straight channels, but not necessarily requiring dense, highly branched structures. This understanding may allow for a greater emphasis to be placed on biocompatibility of the entire fabrication process, which would facilitate development, testing, and eventual clinical translation of engineered tissues.

Chapter 4: DEEP TISSUE VASCULARIZATION VIA 3D PRINTING ENABLED ENDOTHELIAL TRACK PATTERNING

Portions of this chapter have been submitted as a research article to a peer-reviewed journal.
Prado, O*, Malkani, S*, Johansson, F., and Stevens, K.R.S. (2025)

Engineered tissues could one day offer critical therapeutic relief for those requiring whole organ transplantation. Yet, their translation remains hindered by the need for robust, volumetric vascularization throughout increasingly scaled tissues. Here, we used selective laser sintering of sacrificial isomalt templates to pattern vascular promoting "tracks" across centimeter-scale tissue constructs. Upon implantation in athymic mice, the patterned tracks architecturally guided host-mediated chimeric vascularization within fibrin and gelatin methacrylate (GelMA) constructs. While the inclusion of tracks improved the vascularization response within both matrices, GelMA constructs demonstrated greater implant stability after 1 week *in vivo*. To further integrate patterned, track-guided vessels with surrounding self-assembled vessels, we implanted densely cellularized GelMA constructs, resulting in widespread, volumetric vascularization via track-guided and self-assembled vessels that anastomosed with host circulation. This platform enables the generation of vascular networks spanning large, engineered tissues and represents a significant step toward the development of clinically translatable organ-scale tissues.

4.1 INTRODUCTION

Engineered organs hold great promise for treating end-stage organ failure. However, a major challenge in this field is producing vascular networks that volumetrically span entire constructs and integrate with host circulation[124,165]. Progress towards this goal has been made by leveraging the intrinsic ability of endothelial cells to spontaneously self-assemble to form vasculature. Specifically, endothelial cells cultured in biological matrices (*e.g.*, collagen, fibrin) can self-assemble into microvascular networks *in vitro* and *in vivo*. However, self-assembled vessels are limited in size and are randomly oriented, leading to non-physiological blood flow patterns[145–148]. Separately, 3D printing technologies have shown promise in patterning vascular architectures that follow the flow-optimized branching topologies found in biology[85] though resolution limitations have prevented 3D printing from capturing the full scalar range within vasculature[44]. Efforts to recapitulate the complexity of native vasculature has thus been hindered by the lack of methods that leverage both self-assembly and architectural control. Efforts to recapitulate the complexity of native vasculature has thus been hindered by the lack of methods that leverage both self-assembly and architectural control.

We and other have found that patterning endothelial cells and collagen into vascular promoting “tracks” architecturally guide and promote *in vivo* assembly of capillary- and arteriole-scale vessels[11–14,16]. While demonstrating great potential for coordinating microvascular self-assembly with architectural control, these initial studies used a simple micromolding technique, which has limitations in architecture, size, and reproducibility. We thus reasoned that more advanced 3D printing technologies could be deployed to achieve greater architectural

complexity of patterned tracks while improving the reproducibility and precision of track-containing tissues.

Several 3D printing technologies, such as extrusion[166–169], inkjet[170], and stereolithography[171–174], offer precise material 3D patterning, enable rapid design iteration through CAD software, and support the fabrication of larger cellularized tissue constructs with excellent reproducibility. Leveraging 3D printing technologies, sacrificial templating is a particularly promising strategy for enhancing biocompatibility and scalability in tissue size, as it constrains fabrication stressors and timelines to a temporary "sacrificial" material[1,45]. Briefly, a sacrificial vascular pattern is 3D printed, embedded within a cell-laden tissue matrix, and finally dissolved and flushed out to leave a hollow vascular network. Sacrificially patterned networks can then be seeded with endothelial cells to promote formation of functional vasculature. Sacrificially patterned networks can then be seeded with endothelial cells to promote formation of functional vasculature. While exciting progress has been made in sacrificially patterning these vascular networks *in vitro*[175,85,167,166,176,170], integration with host circulation when implanted *in vivo* is critical to ensuring long term survival and function of the tissue.

Additionally, one of the greatest strengths of sacrificial templating is the flexibility it imparts to the surrounding tissue composition[1]. Most 3D printing technologies require highly tuned materials and are unable to vary the matrix composition to tune biological processes[177,178]. Sacrificial templating, in contrast, is highly versatile as only the sacrificial template is subject to these fabrication constraints, while nearly any tissue matrix can be simply cast and polymerized around it. This flexibility is crucial as the field continues to investigate optimal matrix compositions for enhancing engineered tissue stability, viability, and function *in vivo*.

Here, we leverage the advantages of sacrificial templating to scale track patterning to complex branching architectures within centimeter-scale scale tissues of various biomaterial compositions. We employ a platform we term Topological Railways for Assembly of Integrated Networks (TRAIN), in which vascular promoting tracks are sacrificially patterned in complex branching networks within materials that support self-assembly. To achieve this, we leveraged our previously developed method of selective laser sintering (SLS) of isomalt[85] to fabricate large numbers of tissues in parallel and investigate combinatorial (track-guided and self-assembled) vascularization responses. After 1 week *in vivo*, 2D and 3D analyses revealed multiscale vascularization in thick, densely seeded tissues. The scalable, rapid, reproducible, and versatile fabrication pipeline of TRAIN enabled us to assess host-mediated vascularization responses for murine organ-scale constructs composed of various biomaterials, with and without vascular promoting tracks.

4.2 RESULTS

4.2.1 *Sacrificial templating of dendritic TRAIN tissue constructs*

Sacrificial templating is a powerful biofabrication approach for producing TRAIN constructs, offering flexibility in tissue matrix composition and scalability through the rapid casting process[1,45]. Accordingly, we leveraged our SLS platform for 3D printing and smoothing sacrificial isomalt vascular templates[85,179] (Fig. 4.1A left, B). To produce engineered TRAIN tissue constructs, these isomalt templates are first embedded within a biomaterial matrix (with or without embedded cells) and subsequently dissolved and evacuated with saline (Fig. 4.1A, C). Next, the constructs are placed in 3D printed chambers, where the channel network is filled with a mixture of endothelial cells and unpolymerized collagen and incubated *in vitro* to facilitate

collagen polymerization and endothelial cell-mediated compaction (Fig. 4.1C, right). The end result is a TRAIN construct in which the sacrificially templated channel network is filled with 'topological railways' consisting of endothelial cells surrounding a core of compacted and aligned collagen (Fig. 4.1A, D). After 1 week *in vivo*, the vascularization response was assessed via 3D immunostaining, imaging, and vessel tracing (Fig. 4.1E). The ability to pattern these vascular promoting tracks within physiological scale tissue constructs (20mm x 9mm x 3mm, 500µL volume) using a variety of biomaterial compositions is a major advancement of the TRAIN platform.

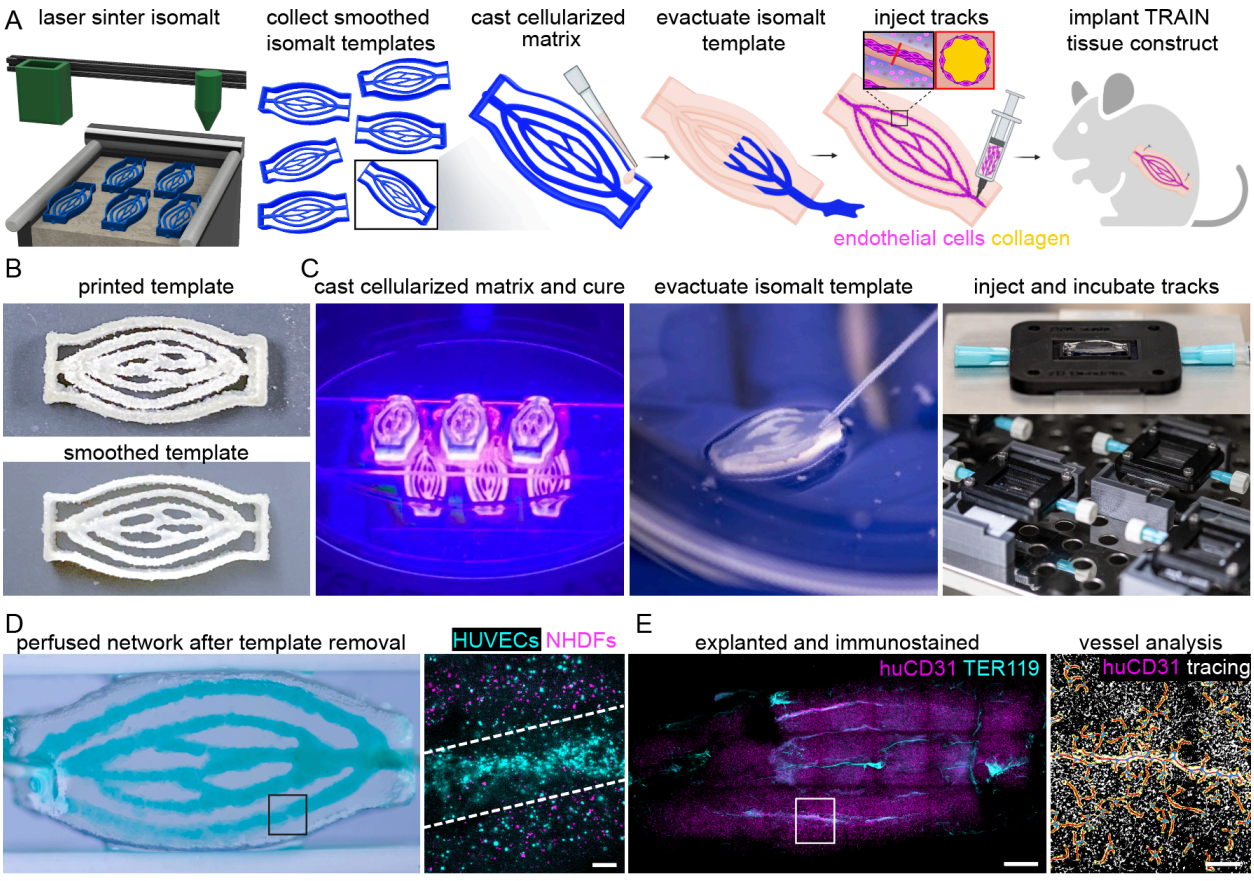

Figure 4.1. Biofabrication of TRAIN tissues via sacrificial isomalt templating of vascular promoting tracks within engineered tissues and downstream analyses.

(A) Workflow for fabrication of TRAIN tissue constructs.

(B) Selectively laser sintered templates before (top) and after (bottom) smoothing.
(C) Matrices are cast and cured before template evacuation and injection and incubation of tracks.
D) Sacrificially templated hydrogel perfused after template removal (left). HUVECs (magenta) and NHDFs (cyan) are cast in the bulk while HUVECs makeup the tracks (right, scale bar = 300μm).
E) 3D immunostaining of huCD31 (magenta) and TER119 (cyan) in explanted tissue (left, scale bar = 1mm) and downstream vessel analyses (right, scale bar = 200μm).

Achieving reproducible and high-powered (large sample size) fabrication of isomalt vascular templates for TRAIN required us to expand our prior SLS work to optimize fabrication of the desired dendritic vascular architecture. First, sintering parameters were examined using a simple straight filament design. Specifically, laser power and translation speed were tuned to achieve fine (thin) filaments (Fig. 4.2A, B). We found that laser power was inversely correlated with filament diameter (Fig. 4.2B). Conversely, translation speed was directly correlated with filament diameter up to a point, with higher translation speeds resulting in thinner sintered filaments up to a speed of 2800 mm/min, beyond which there was no resolution improvement (Fig. 4.2A, bottom right, B). Thus, we identified a promising parameter space for high fidelity sintering of thin filaments (Fig. 4.2A, blue box).

We then further interrogated this parameter space for maintenance of pattern fidelity by 3D printing vascular templates (2800 mm/min laser translation speed, 18-20 W/mm^2; Fig. 2C, left). After post processing, we observed pattern warping of templates at the lowest laser power and fusing of filaments at junctions at the highest laser powers in this parameter space, respectfully (Fig. 3.2C, top right and bottom right, respectfully). Conversely, intermediate laser power (19.5 W/mm^2) resulted in reproducible fabrication and post processing of templates with no discernable pattern warping or filament fusions (Fig. 3.2C, middle). The end result was a

process for parallelized fabrication of high fidelity sintered isomalt vascular templates (Fig. 4.1,4.2).

We finally wanted to assess if we could deploy this method to fabricate TRAIN constructs within different biomaterial matrices. Specifically, we evaluated host-mediated vascularization in fibrin, a natural hydrogel known to support robust vascular self-assembly[11–13,180–182], and gelatin methacrylate (GelMA), a widely used biomaterial which contains bioactive moieties for cell attachment and photoactive moieties enabling stereolithographic 3D printing[183–185]. We embedded sacrificial vascular templates in either fibrin or GelMA and evacuated the isomalt (Fig. 4.2D, "blank"). Next, we patterned tracks into both biomaterial matrices (Fig. 4.2D, "tracks") and confirmed the presence of red fluorescent protein- (RFP) expressing human umbilical vein endothelial cells (HUVECs) in the tracks in both biomaterials (Fig. 4.2E).

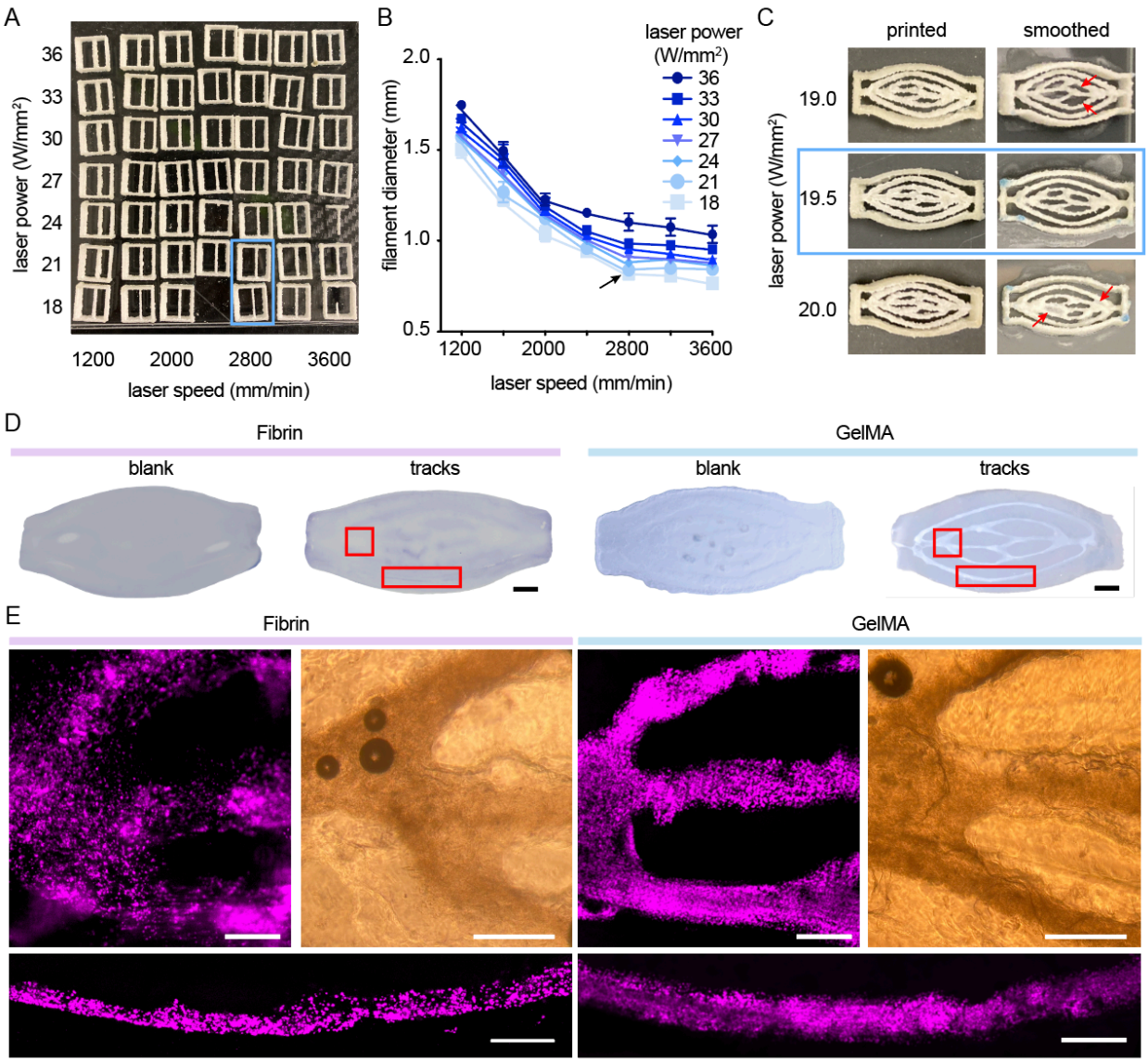

Figure 4.2. In vitro optimization for biofabrication of TRAIN tissue constructs.

(A) Laser power and translation speed screening to sinter reproducible filaments.

(B) Decreased laser power and translation speeds enable fabrication of thin isomalt filaments.

(C) Smoothing of isomalt templates printed at low laser powers.

(D) Sacrificially templated Fibrin (left) and GelMA (right) tissue constructs. Scale bar = 2mm.

(E) Patterned tracks using RFP-HUVECs (magenta) in Fibrin and GelMA TRAIN tissues. Confirmation of tracks in middle branching points (top) and outer branches (bottom). Scale bars = 500μm.

4.2.2 *Patterned tracks guide formation of chimeric host-graft vessels perfused with host blood*

Following optimization of biofabrication methods for TRAIN tissue construct, we set out to validate whether patterned tracks with complex branching geometries in 10x larger tissues guided vasculature and host integration as shown in previous track-containing patches. Towards this end, we cast acellular fibrin and 5% GelMA precursors around sacrificial isomalt templates. We opted to use acellular matrices here to ensure any vasculature formed and visualized was either tracks or host derived, thus isolating the ability of tracks alone to guide vascularization. Once the isomalt was evacuated, we injected the tracks slurry, incubated for 3 hours, and implanted into the intraperitoneal (IP) space of nude mice for 2 weeks *in vivo*.

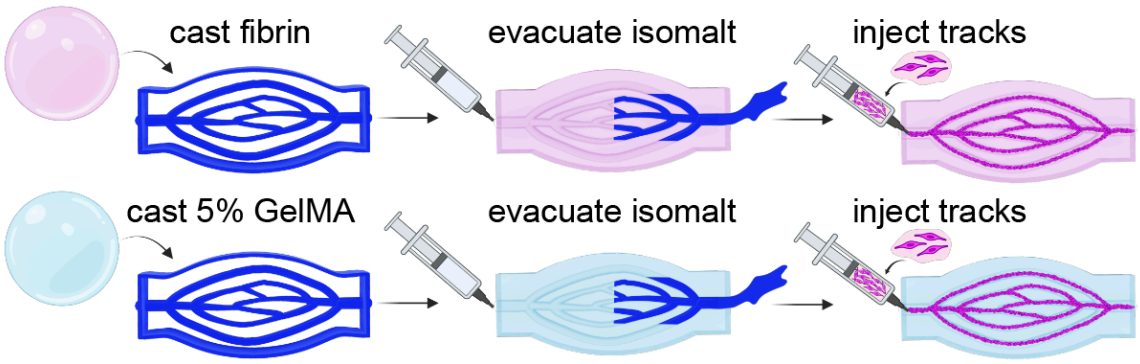

Figure 4.3. Fabrication of acellular fibrin and GelMA track containing tissues.
Workflow for fabrication of aceelular fibrin (top) and GelMA (bottom) track containing tissues.Acellular precursors are cast into template and cured before isomalt is flushed out. Finally cell-collagen slurry is injected and incubated to form tracks.

In order to evaluate whether the vasculature formed exhibited similar chimeric, host-graft phenotype as preciously observed, we injected fluorescent human- and rodent-lectins intravenously to label perfused human (magenta) and host derived (cyan) endothelium before explant. After explant, we rendered the tissue constructs optically transparent before imaging in

3D using scanning confocal microscopy. In both fibrin and GelMA tissue constructs, we observed formation of chimeric, host-graft- vessels, depicted as white due to overlapping magenta and cyan signal (Fig. 4.4A) in various of the patterned tracks regions. Upon quantification, we observed no significant differences between human- or rodent- lectin area in either fibrin or GelMA tissue constructs (Fig. 4.4B).

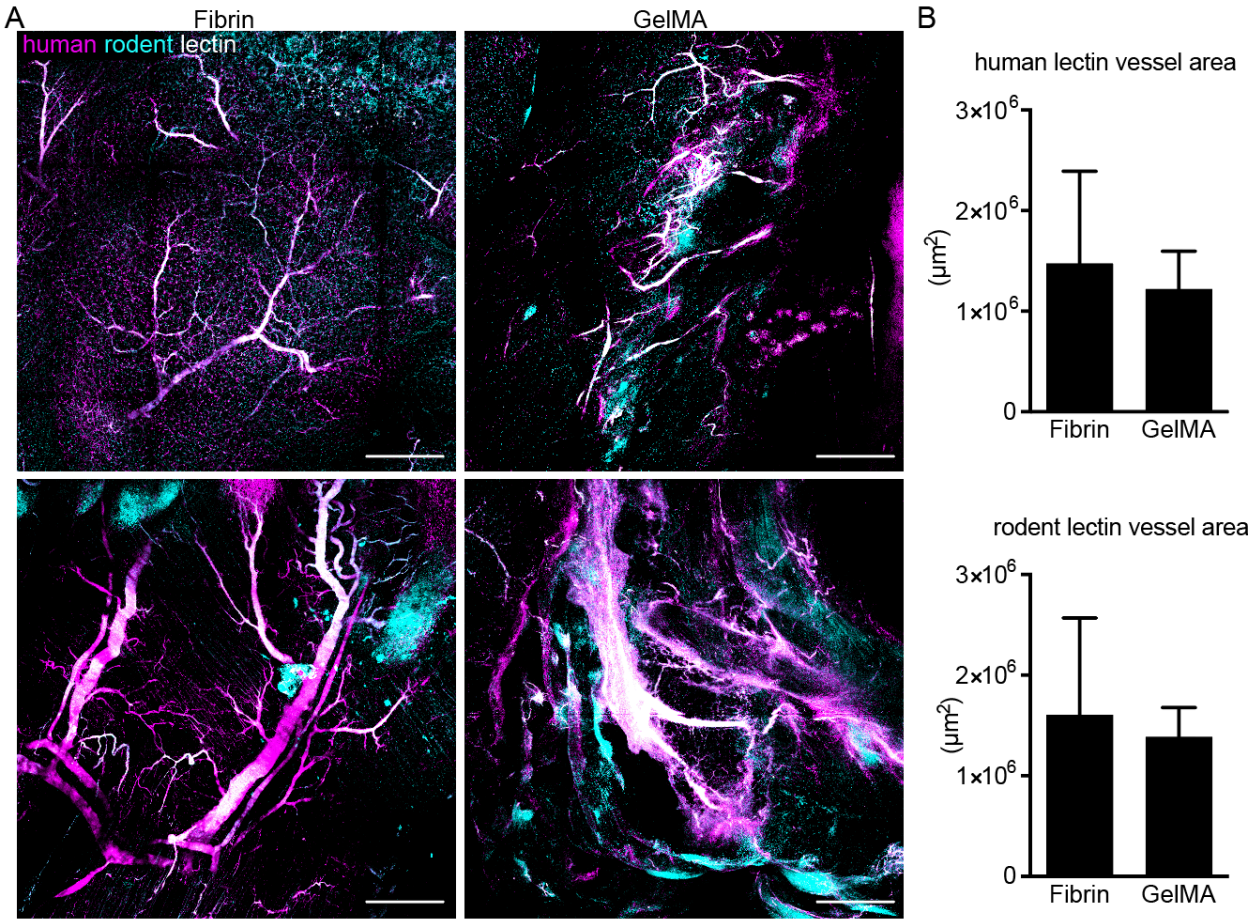

Figure 4.4. Tracks guide formation of host-graft vessels in fibrin and GelMA tissue constructs.

(A) Tracks associated vasculature in fibrin and GelMA tissues perfused with human (magenta) and rodent (cyan) lectins before explant. Scale bar = 500μm.

(B) Quantification of human (left) and rodent (right) lectin fluorescent area revealed no significant differences in vascularization between fibrin and GelMA tissues. $n \geq 3$ for both groups. Data represented as mean ± SEM.

As no significant differences were observed between human- or rodent-lectin positive fluorescent vessel area, we thus qualitatively evaluated the explanted tissues at a macro scale. Curiously, the track-containing GelMA tissue constructs seemed to retain their original implant shape (Fig. 4. bottom row), while the track-containing fibrin tissue constructs were obviously compacted and misshapen, bearing no resemblance to the implanted tissue architecture (Fig. 4. top row). Moving forward, we decided to continue investigation of both biomaterial matrices as candidates for fabrication of large, functional engineered tissue construct.

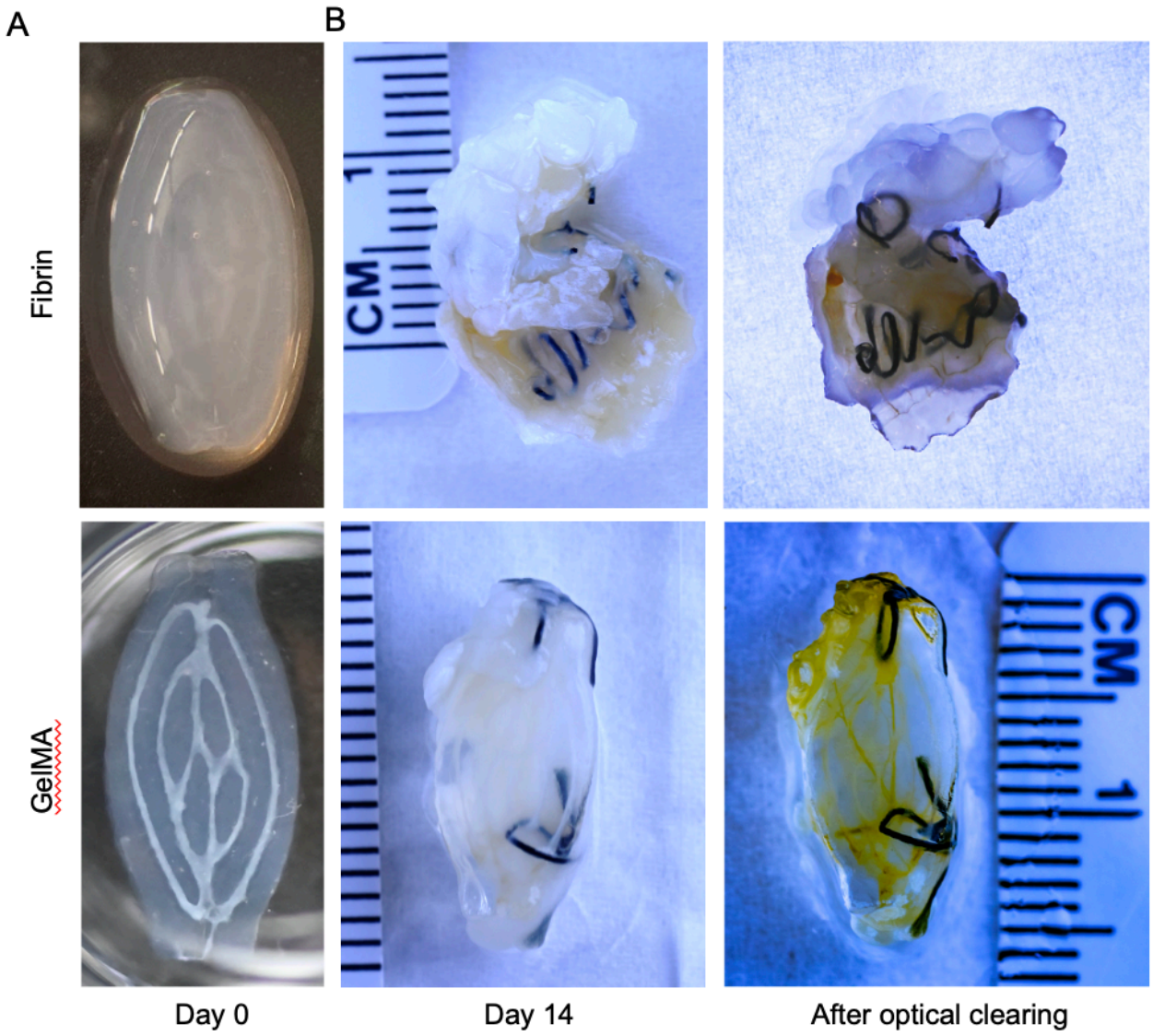

Figure 4.5. Differential degradation in fibrin versus GelMA track containing tissues after 14 days.

(A) Track containing fibrin (top) and GelMA (bottom) tissue constructs before implantation.
(B) Explanted track- containing fibrin (top) and GelMA (bottom) tissue constructs after explant (left) and after optical clearing (right).

4.2.3 *Tracks guide vascularization within fibrin and GelMA tissues*

Next, we sought to investigate if vascular promoting tracks could improve the *in vivo* vascularization response in scaled tissues. Towards this end, we leveraged the TRAIN platform to increase track-patterned construct volume by an order of magnitude (cm-scale, 500μL) compared to our previous work (mm-scale, 50μL)[11–13]. We fabricated sacrificially templated tissue constructs with HUVECs and fibroblasts in the bulk in either fibrin or GelMA (Fig. 4.6A; 10mg/ml fibrin, 5 w/v% GelMA). After template evacuation, patterned channels in control tissues were left vacant (blank), while the remaining tissues were injected with vascular promoting tracks (Fig. 4.6A).

All engineered tissues were implanted on the gonadal fat pad in the intraperitoneal (IP) space of athymic mice and explanted after one week. Gross observation of the explanted tissues suggested the presence of host blood within both fibrin and GelMA tissues that had tracks, but not in blank controls (Fig. 4.6B). Interestingly, the blood was patterned in architectures that mimicked the original vascular templates, especially for explanted GelMA tissues with tracks. Furthermore, the overall size of GelMA tissues appeared more similar to implanted tissue size than fibrin tissues for both blank and tracks groups (Fig. 4.6B, C). Quantification of gross tissue size showed that demonstrated GelMA tissues maintained >70% of their original size compared to tissue constructs at Day 0 (Fig. 4,6C). Conversely, explanted fibrin tissues were substantively smaller (<40% of original size; Fig. 4.6C).

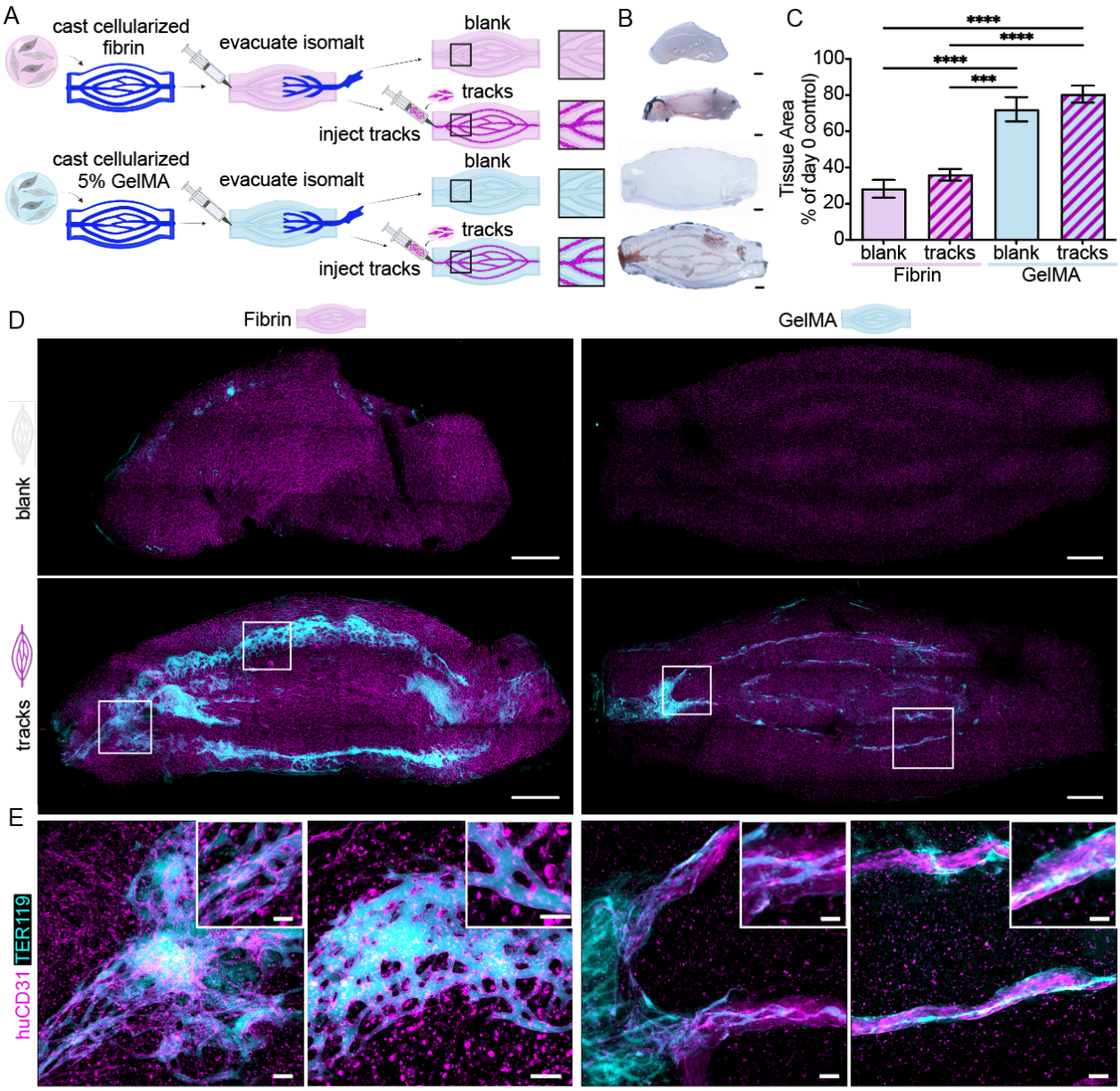

Figure 4.6. *In vivo* vascularization guided by tracks within fibrin and GelMA TRAIN tissue constructs.

(A) Workflow for fabrication and implantation of fibrin or GelMA tissue constructs with or without tracks. (B) Explanted fibrin (top) and GelMA (bottom) tissue constructs with visible blood in track containing tissues.

(C) Quantification of tissue area after explant reveals significant reduction in fibrin tissue sizes. n≥4. Data are represented as mean +/- SEM. *** $p < 0.001$, **** $p < 0.0001$.

(D) Immunostaining of huCD31 (magenta) and TER119 (cyan) in fibrin (left) and GelMA (right) tissues with blank channels (top) or tracks (bottom) for after 7 days *in vivo*. Scale bar = 1mm.
(E) ROIs depicting vasculature (magenta) with host blood (cyan) along patterned tracks. Scale bars = 100μm. Inset scale bars = 50μm.

To examine vascularization and host integration in the explanted tissues, 3D immunostaining followed by tissue clearing enabled visualization of human endothelial cells (huCD31, magenta) and host red blood cells (RBCs) (TER119, cyan) via confocal imaging (Fig. 4.6D, E). Vessel tracing analysis using Angiotool[186] revealed that all explanted tissues from all groups contained human CD31-positive endothelial cells (Fig. 4.7A, B). Many of the track patterned regions had self-assembled into branching structures reminiscent of an immature vascular plexus (Fig 4.7A, B, top rows). There was no difference between total huCD31 signal between blank and tracks groups for each biomaterial, though endothelial cells in bulk regions of fibrin tissues appeared to be more spread out (Fig. 4.7C). Fibrin tissues also had higher vessel density than GelMA tissues of the same experimental conditions (blank and tracks, Fig. 4.7D, E).

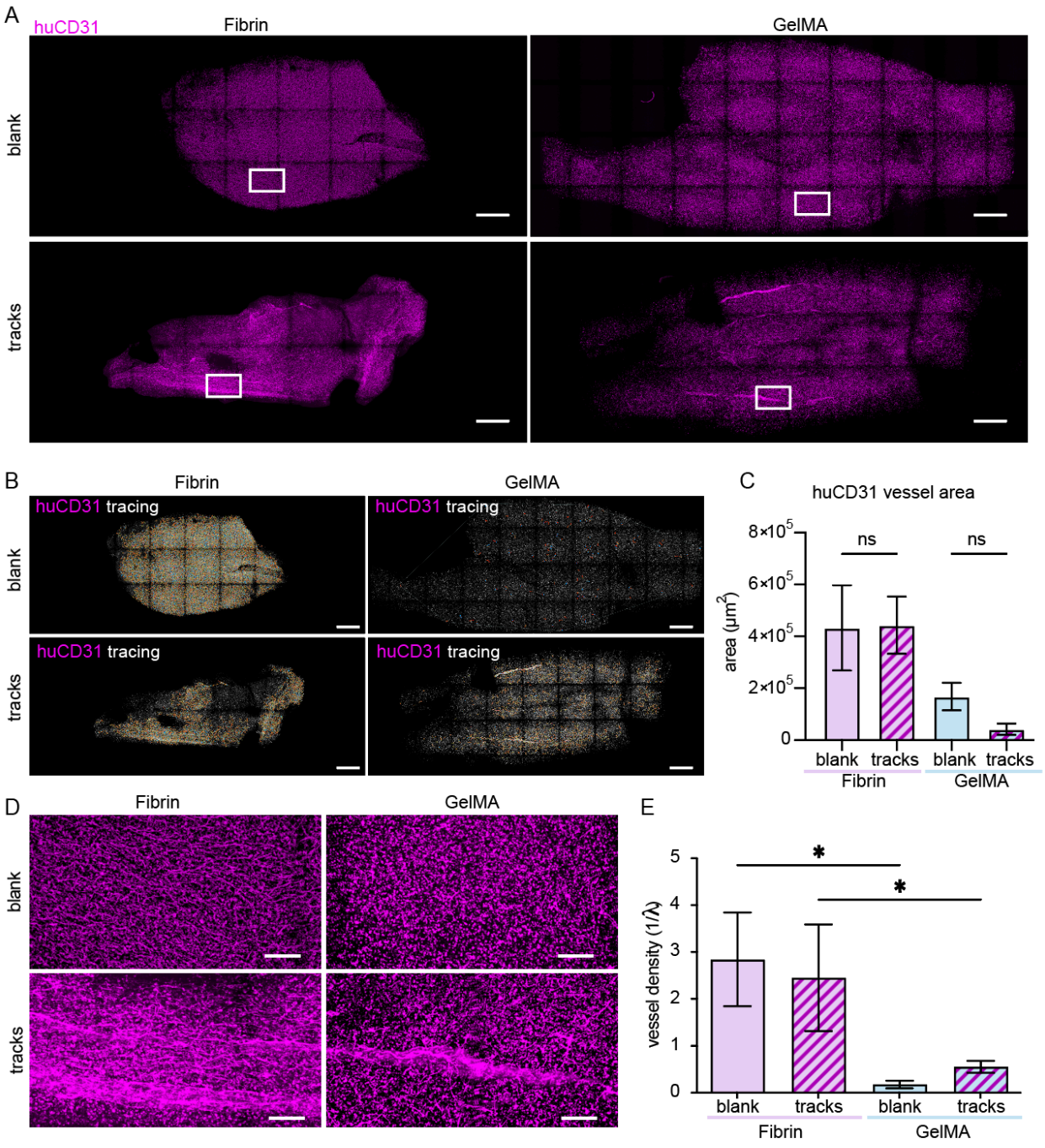

Figure 4.7. huCD31 vessel tracings and analyses.

(A) Immunostaining of huCD31 (magenta) in fibrin (left) and GelMA (right) tissue constructs with blank channels (top) or patterned tracks (bottom). Scale bars = 1mm.

(B) Angiotool tracings of huCD31 signal. Scale bar = 1mm.

(C) Quantification of TER119 traced vessel area. n = 5 for all groups. Two-way ANOVA, Šídáks multiple comparison test. Data are represented as means +/- SEM.
(D) High magnification insets of huCD31(magenta) vessels reveals differential vessel formation and spreading in fibrin (left) versus GelMA(right) tissue constructs. Scale bars = 1mm.

While the presence of huCD31-positive vessels in the engrafted tissue is encouraging, the vessels must also transport blood from the host circulation throughout the tissue to provide essential gas and nutrient exchange. Therefore, we next performed vessel tracing on the TER119 signal of the explanted tissues (Fig. 4.8A). We found that both tracks groups contained greater TER119+ vessel area compared to blank groups of the same biomaterial, revealing significantly improved integration with host circulation in tissues with patterned tracks (Fig. 4.8A, B).

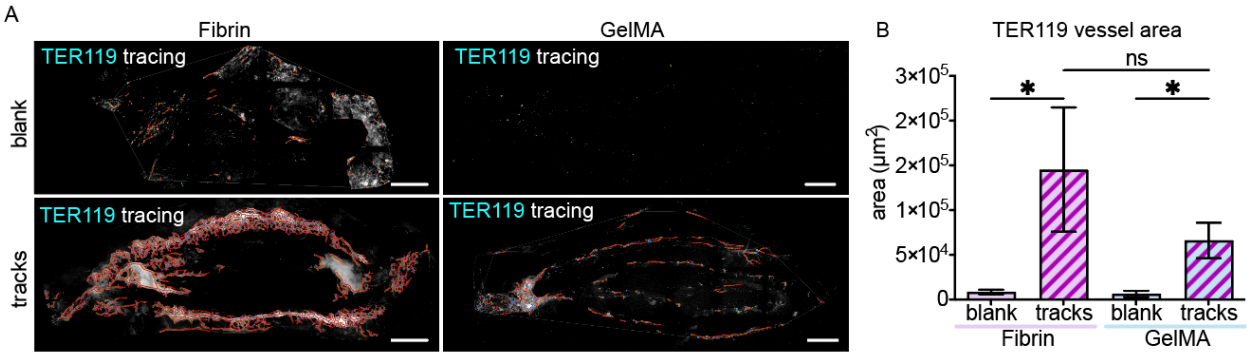

Figure 4.8 Host blood filled vessel tracing and analysis.

(A) Angiotool tracings of TER119 signal. Scale bar = 1mm.

(B) Quantification of TER119 traced vessel area. n = 5 for all groups. Two-way ANOVA, Šídáks multiple comparison test. Data are represented as means +/- SEM. * $p < 0.05$.

The TER119 signal largely followed the patterned architecture in both fibrin and GelMA constructs, indicating that tracks facilitated host blood transport along the designed network (Fig. 3D, bottom). Notably, in fibrin tissues, the TER119 signal formed interconnected, vascular plexus-like structures (Fig. 4.6E, left), while in GelMA tissues, the signal revealed long,

anisotropic structures aligned to the track geometry (Fig. 4.6E, right). Despite these morphological differences, both constructs had blood present along the designed tracks, suggesting that the tracks architecture influenced vascular alignment and blood ingress. To further characterize this architectural guidance, we compared the local orientation of a branched region of the designed vascular architecture (Fig. 4.9A, white box) to huCD31 signal within the same region in explanted tissues (Fig 4.9B). We found that both fibrin and GelMA tracks groups contained significantly more huCD31+ vessels aligned (+/- 15°) to the designed branch compared to each of the blank groups (Fig. 4.9C, D), supporting the hypothesis that tracks architecturally guide vascular assembly. In summary, these results suggest that the inclusion of tracks within patterned channels improves alignment of vessel formation to the patterned architecture. We posit that the tracks serve as 'topological railways', directing endothelial cell migration and supporting the self-assembly of vessels that are lined with human endothelial cells and transport host blood into the tissue.

Finally, we examined the spatial distribution of vessels across the designed network. GelMA constructs showed a more uniform vessel distribution across both inner and outer branches (Fig. 4.9E,F). In contrast, fibrin constructs appeared to favor vessel formation along the outer branches, suggesting limited support for vascularization in the central regions of the patterned network (Fig. 4.9E, F).

Taken together, these results suggest that GelMA constructs better preserve implant integrity and support the formation of long, blood-perfused vessels that follow the track architecture with more uniform spatial distribution. In contrast, fibrin constructs exhibited higher vessel density, potentially due to compaction during degradation, but formed plexus-like networks with preferential vascularization along outer regions. These findings led us to continue

investigations with GelMA constructs, with efforts focused on increasing the density of vessel formation.

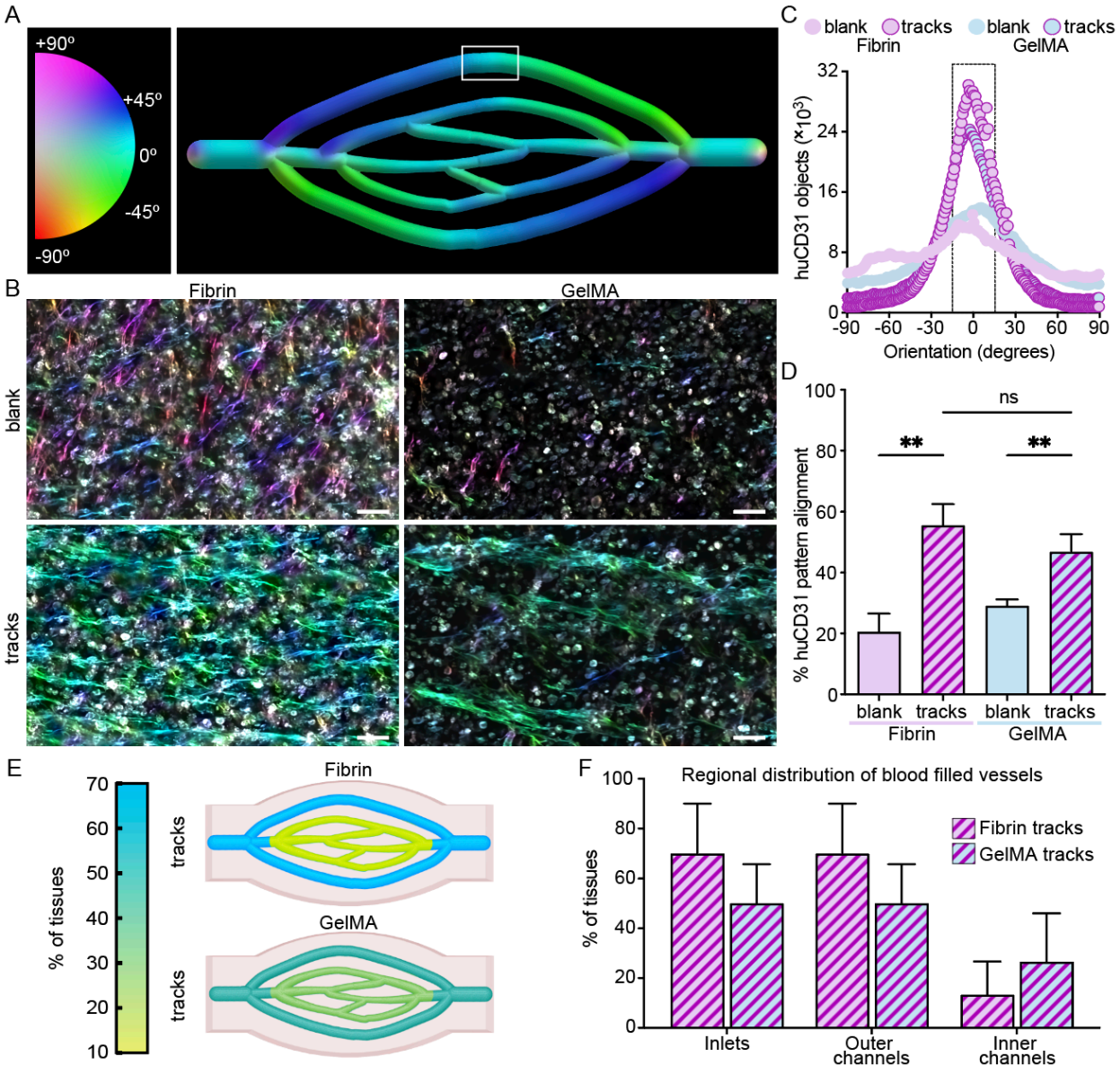

Figure 4.9 Vessel formation and spatial distribution analyses.

(A) Orientation coded dendritic network design. Orientation labeled from +90° to -90°.

(B) Orientation coded huCD31 ROIs. Scale bar = 100μm.

(C) Mean distribution of huCD31 orientation. n = 3. Gray region represents 0+/- 15°.

(D) Percent of huCD31+ objects aligned to channel (within +/-15°). n = 3. Data are represented as mean +/- SEM. Two-way ANOVA, Tukeys multiple comparison test. *p < 0.05, ** p< 0.01.
(E) Regional distribution of blood-filled vessel in Fibrin (top) and GelMA (bottom) track containing tissue constructs represented visually.
(F) Quantification of blood-filled vessel distribution. Data are represented as mean +/- SEM.

4.2.4 *Densely seeded GelMA tissue with sacrificially patterned tracks enables volumetric vascularization*

Collectively, our result thus far demonstrated track-patterned GelMA tissue constructs supported vascularization and host integration *in vivo* while also maintaining pattern and tissue fidelity, albeit with lower vessel densities compared to fibrin. To achieve robustly patterned tissues that maintain their shape and are densely cellularized with self-assembled vasculature, we next sought to increase vascular density by increasing the concentration of HUVECs and fibroblasts in the GelMA matrix surrounding the tracks.

High cell concentrations have been shown to decrease the stiffness and strain relaxation behaviors of hydrogel matrices[187]. Therefore, to account for potential excessive softening and accelerated degradation of 5% GelMA, we sacrificially templated both 5% and 15% GelMA containing 5X higher cells concentrations of HUVECs and fibroblasts in the bulk and implanted them *in vivo* (Fig. 4.10A). Gross examination of tissues explanted after 1 week revealed host blood in both 5% and 15% GelMA constructs (Fig. 4.10B).

To further examine self-assembled and patterned vascularization, we carried out 3D immunostaining for huCD31 (magenta) and TER119 (cyan), followed by tissue clearing and confocal imaging (Fig. 4.10C). Imaging and quantification showed widespread dense self-assembled vessel networks lined with human endothelial cells (magenta), much of which were

filled with host blood (cyan), in the 5% GelMA tissues (Fig. 4.10C, left). Conversely, 15% GelMA tissues showed comparatively lower vascular assembly and blood infiltration (Fig. 4.10C, right). These findings were further confirmed with vessel tracing analysis (Fig. 4.10D-H). Although aligned vessels were present along some of the tracks in 15% GelMA constructs, blood infiltration remained minimal (Fig. 4.10D, E). Additionally, 5% GelMA tissues had significantly more vessel area and density compared to 15% tissues (Fig. 4.10F, G), as well as significantly higher blood-filled vessel area (Fig. 4.10H).

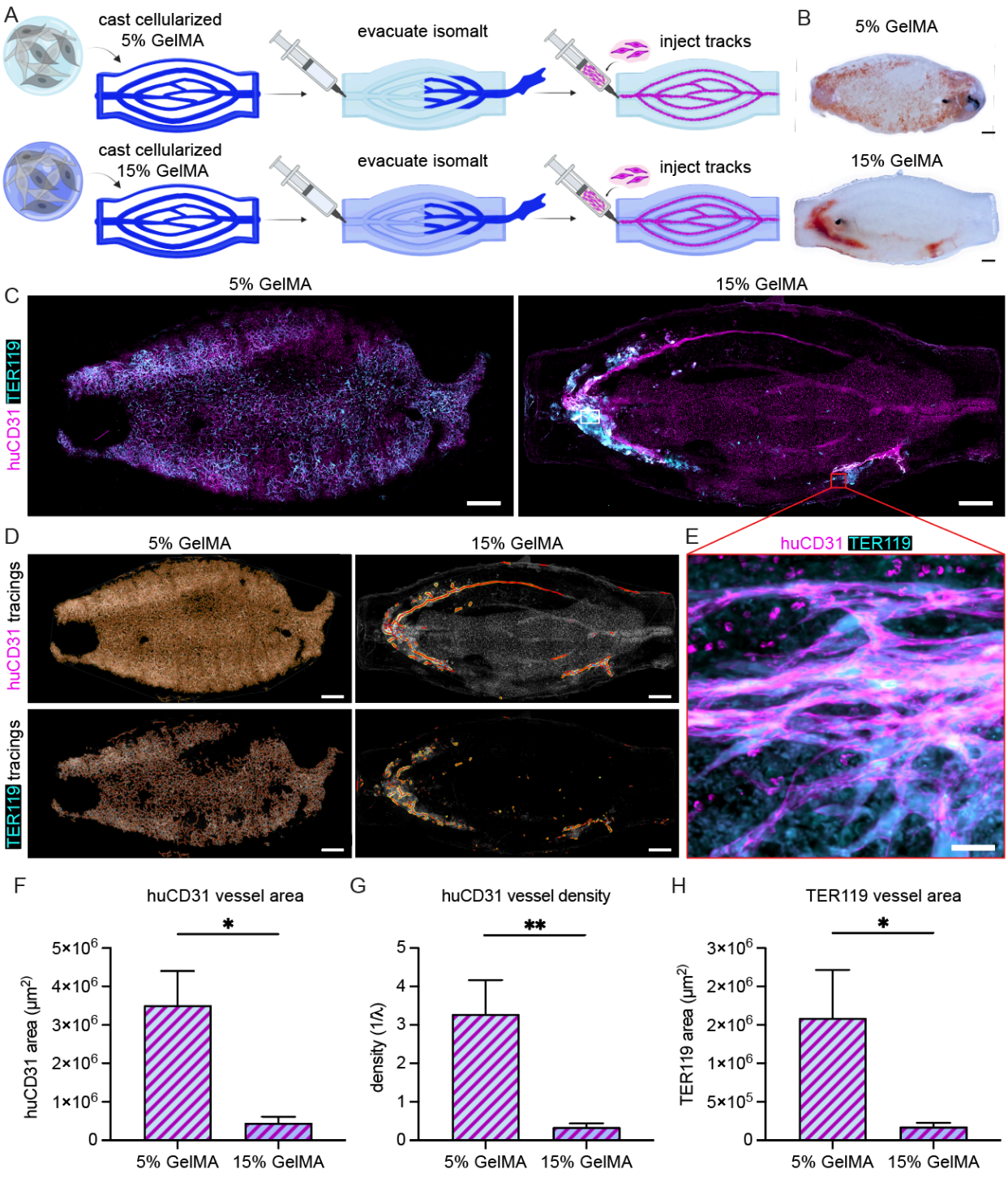

Figure 4.10. Differential vascularization responses in densely seeded 5 and 15% GelMA TRAIN tissues.

(A) Fabrication and implantation of sacrificially templed 5 or 15% GelMA tissues construcvts with tracks. (B) Explanted 5% (top) and 15% (bottom) GelMA tissue constructs after 7 days in vivo. Scale bar = 1mm. (C) Immunostained 5% and 15% GelMA tissue constructs for huCD31 (magenta) and TER119 (cyan). Scale bar = 1mm.
(D) huCD31 (top) and TER119 (bottom) angiotool tracings of 5% and 15% GelMA tissue constructs. Scale bar = 1mm.
(E) High magnification reveals limited vasculature in track adjacent regions in 15% GelMA tissue constructs with huCD31 lining of host RBC filled vessels. Scale bar =100μm.
(F) Quantification of huCD31 vessel area. Data are represented as mean +/- SEM. n = 6 for all groups. Mann Whitney test. * $p< 0.05$.
G) Quantification of huCD31 vessel density. Data are represented as mean +/- SEM. n = 6 for all groups. Mann Whitney test. * $p< 0.05$.
(H) Quantification of TER119 vessel area. Data are represented as mean +/- SEM. n = 6 for all groups. Mann Whitney test. * $p< 0.05$.

Given the degree of widespread vascularization in the 5% GelMA tissue constructs (Fig. 4.11A, left), we carried out 3D analyses to further examine track-patterned and bulk regions. To facilitate visualization of the vascularization response within and around the track-containing regions, we first examined 3D reconstructions of the immufluorescent signals and observed robust vascularization from several angles (Fig. 4.11A). Interestingly, the levels of vascular assembly seemed to correlate with track-containing regions (Fig. 4.11A). We next examined huCD31 and TER119 signal distribution across x, y, and z axes, and found that both signals spanned ~14mm in the x-direction, ~6mm in the y-direction, and ~2mm in the z-direction (Fig. 4.11B).

Additionally, we observed self-assembled vessels lined with human endothelial cells (magenta) carrying host blood (cyan) present in the tissue in track regions along both the outer (Fig. 4.11C, top) and inner (Fig. 4.11C, bottom) branches of patterned network. The vascularization response was seemingly dominated by self-assembled isotropic networks when

viewing the full depth of the tissue (Fig. 4.11A, C). However, a closer look through the z-stacks at the track regions revealed long vessels aligned to the tracks. Interestingly, these track-aligned vessels had angiogenic-like sprouts inosculating with the isotropic microvascular networks in the bulk regions (Fig. 4.11D; immunofluorescent images, top; surface renderings, bottom). This finding supports our hypothesis that tracks act as railways to guide vascular ingrowth deep into the tissue construct, after which vascular sprouts further emanate and pervade the bulk of the gel.

Finally, we examined the diameters of assembled vasculature in track-patterned and bulk regions of the sacrificially patterned tissues. This is important because native vascular networks contain scalar hierarchy, with large diameter vessels (arteries, veins), mid-sized vessels (arterioles, venules), and small vessels (capillaries) contribute to gas and nutrient transport dynamics in distinct ways, affecting overall tissue survival and function[44]. In previous work with 2D track-patterned tissues, we saw track-associated vessels had on average larger diameters than those not associated with patterned tracks[13]. We thus hypothesized that self-assembled vasculature near tracks would also have greater diameters than vessels in unpatterned regions of the tissue construct. To examine this, we isolated a region containing a patterned track segment in a 5% GelMA tissue (Fig. 4.11E left). Diameter coded Imaris filament tracings on both huCD31 and TER119 signals revealed relatively larger diameter tracings (pink) within the track region compared to the adjacent bulk regions (Fig. 4.11E right). Histograms of object diameters within track-patterned and bulk regions further confirmed the association of larger diameter objects with track-patterned regions (Fig. 4.11F). Together, these findings demonstrate robust track-mediated *in vivo* vascularization of GelMA tissue constructs, suggesting potential utility of tracks for recapitulating vascular hierarchies.

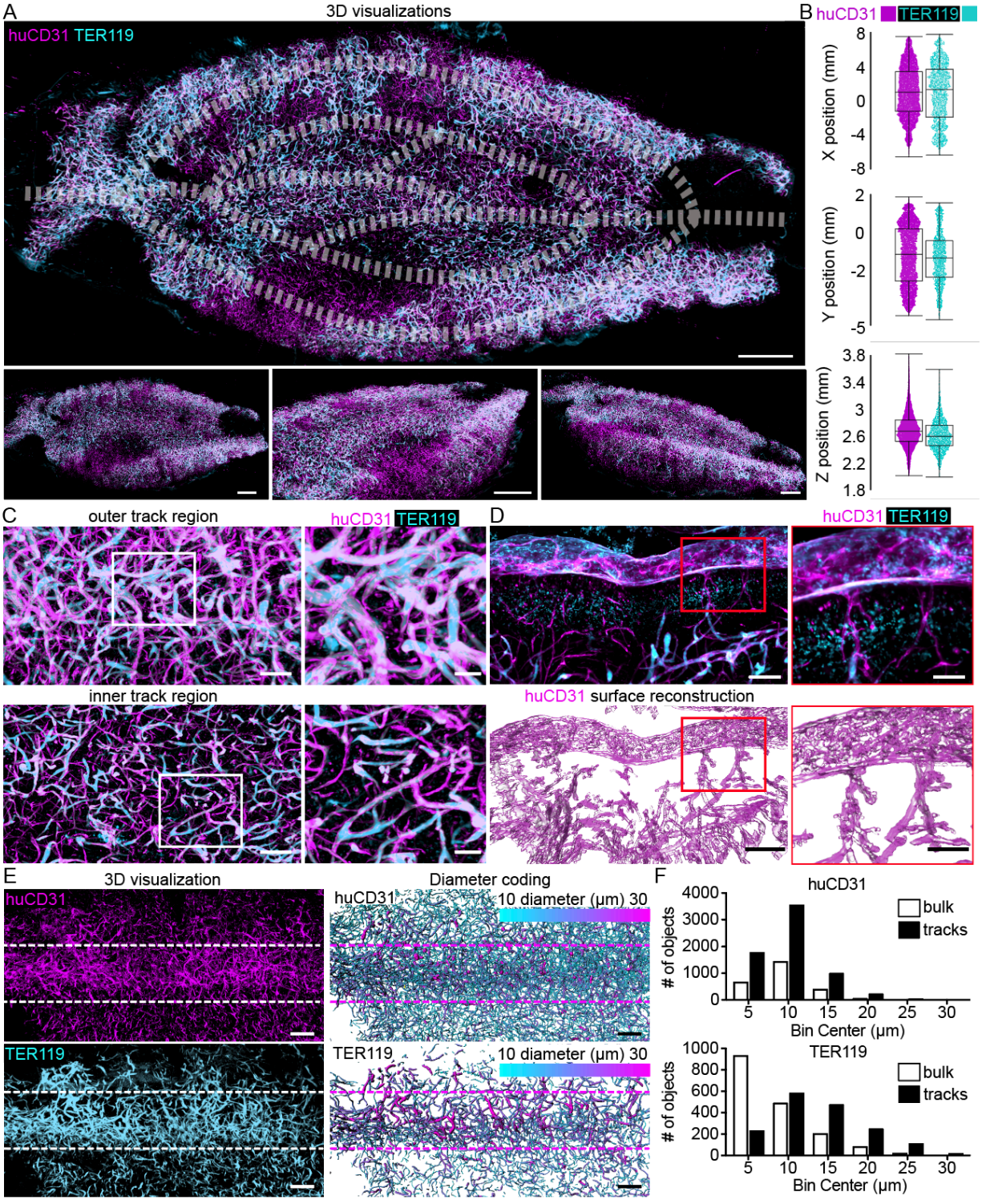

Figure 4.11. Volumetric *in vivo* vascularization of densely seeded 5% GelMA TRAIN tissue constructs.

(A) 3D visualizations of huCD31(magenta) and TER119 (cyan) immunostaining of a 5% GelMA TRAIN tissue construct after 7 days *in vivo*. Top-down view overlaid with patterned track architecture (top, white dashed lines) and oblique views highlight volumetric distribution of vasculature. Scale bars = 1 mm.
(B) Object distribution in the x-, y- and z-directions of huCD31 and TER119 surface renderings.
(C) Blood filled vessels in various track regions across the 5% GelMA tissue construct. Scale bars = 100μm. (D) 3D immunostaining of long vessels aligned to tracks and connecting with self-assembled vessels (top) and corresponding huCD31 Imaris surface (pink, bottom).
(E) huCD31 (top) and TER119 (bottom) 3D immunostaining visualizations (left) and corresponding diameter coded filament tracings (right) of patterned track region. Scale bar = 300μm.
(F) huCD31 (top) and TER119 (bottom) filament diameter distribution histograms.

4.3 DISCUSSION

In this work, we employ 3D printing technologies to pattern vascular promoting tracks in various biomaterial matrices via fabrication of centimeter-scale TRAIN tissue constructs. We successfully generated branched vascular networks that integrate with host circulation at mouse organ-scale dimensions. The resultant tissue constructs undergo widespread volumetric vascularization with distinct tracks-associated vessel morphometrics, demonstrating the potential for fabricating large, multiscale vascularized tissues.

A critical factor influencing vascularization outcomes in engineered tissues is the selection of biomaterials, particularly with regard to cell-interfacing domains, matrix stiffness and strain relaxation behavior, and degradation kinetics[188–191]. The ideal tissue matrix would promote rapid assembly of vasculature and integration into host circulation and resist excessive remodeling and degradation *in vivo*. Although some remodeling is necessary for generation of spontaneous self-assembled vasculature, excess degradation can disrupt patterned vascular architectures, leading to formation of irregular and dysfunctional vascular networks that are unable to effectively transport oxygen and nutrients to the surrounding tissue[189,192–194]. Thus,

tuning biomaterial properties, such as biological and synthetic crosslinker compositions and concentrations, could optimize matrix longevity while ensuring permissive conditions for both self-assembled and biofabrication-mediated vascularization. The TRAIN platform may be particularly powerful in screening biomaterial matrices, as it enables rapid fabrication of large numbers of centimeter-scale tissues and is compatible with nearly any cellularized biomaterial formulations.

Spatial organization and cellular configuration of vasculature play a crucial role in organ function[195]. We show here that track-patterns influence vessel orientation, demonstrating directed vascular growth along the pre-defined architecture. This strategy could be adapted for organ-specific vascular networks where architecture is closely tied to function. Moreover, incorporation of organ-specific endothelial cells (e.g., liver sinusoidal endothelial cells) may drive regional vascular specialization[196–198]. Additionally, incorporating a diverse range of stromal cell types, such as specialized fibroblasts[199,200], stem cells[201,202], and/or mural cells[203,204], could further support vessel stabilization and maturation for sustained tissue function. Spatial patterning of biochemical and biomolecular gradients in cellularized matrices could further accelerate formation of multiscale vasculature with appropriate cellular composition and organization[171,205,206].

While our approach successfully guided vascularization at the inlets and outer channels, inner channels exhibited less vascular assembly. This is potentially due to the smaller diameters of the inner channels, as patterned tracks with larger diameters have been shown to increase vessel density and presence of host RBCs *in vivo*[11]. Additionally, tracks patterned near the inlets are closer to host tissue and thus may contribute to earlier formation of vasculature and anastomosis with host circulation. Further investigations will examine additional vascular

architectures and the influence of track geometries on vascularization potential to improve tissue-wide vascularization.

In densely seeded tissues, more widespread and volumetric vascularization was observed, indicating that increasing the metabolic demand within the tissue may be a tractable approach to promoting vascularization. While the vascularization responses observed in TRAIN tissues are encouraging, future studies incorporating parenchymal cells will be essential in evaluating the potential of the TRAIN platform to fabricate highly functional, physiologically scaled engineered tissues.

Vascular networks within engineered tissues must support essential biological functions to provide therapeutic relief upon implantation. Given the intrinsic relationship between vascular architecture and tissue function, the ability to guide vascular network formation and integration with host circulation *in vivo* is critical to ensure long term perfusion and function of large, engineered tissues. Development of the TRAIN platform represents a major step towards this, demonstrating guided vascularization along patterned architectures that integrate with host circulation within centimeter-scale tissues of various biomaterial matrices. In all, the biofabrication methods and analysis pipelines presented here enable volumetric vascularization of thick, densely seeded tissues, collectively advancing engineered tissues toward clinical translation.

4.4 METHODS

4.4.1. *Selective laser sintering of isomalt templates*

Isomalt templates were fabricated as previously described using a custom SLS printer[85,179]. Briefly, isomalt (Decomalt, Paris Gourmet) was ground and strained through a No.

140 mesh (106μm grid spacing). Corn starch (Argo) was mixed into the isomalt at a 3:7 mass ratio to improve flowability of the powder. G-code files were generated using Slic3r, modified using a Python script, and loaded into Pronterface. An initial layer of powder was distributed onto the SLS printer and layer-by-layer (150μm) sintering was initiated in Pronterface using 18-21 W/mm^2 laser power and 2500 - 2800 mm/min laser translation speed. Following the sintering process, isomalt templates were smoothed by dipping them in a concentrated (60% w/v) isomalt solution and treated with an amphiphilic solution (25% w/v PEG-stearate (Myrj S8) in chloroform) to prevent premature template dissolution during casting of tissue matrix precursors. Templates were adhered to glass slides using 30% w/v Pluronic F127 (Sigma-Aldrich) in chloroform. Prior to tissue casting, isomalt templates were sterilized under UV for 30 minutes.

4.4.2 *Catheterization chamber design and preparation*

To facilitate hydrogel handling and cell injection, we designed and 3D printed catheterization chambers using a previously published OpenSCAD script[207]. Chambers, lids, and poly(dimethylsiloxane) (PDMS) gasket molds were printed with PLA on an Ultimaker 3D extrusion printer. 6:1 PDMS was filled into the gasket molds and used to adhere glass slides to the printed components as the top and bottom surfaces to form a sealed chamber with photocuring capability. All components were sterilized by soaking in 70% ethanol for 1 hour and exposing to UV light for 30 minutes before use.

4.4.3 *Cell culture*

Human Umbilical Vein Endothelial Cells (Lonza, P4-P7) were cultured in EGM2 (Lonza), Neonatal Normal Human Dermal Fibroblasts (Lonza, P7) were cultured in Dulbecco's Modified Eagle's Medium (DMEM) +10% v/v fetal bovine serum (FBS), and mouse

mesenchymal cells CH310t1/2 (ATCC, P7–P9) were cultured in low-glucose DMEM + 10% v/v FBS.

4.4.4 *Fabrication of sacrificially templated tissues*

Sacrificially templated tissues contained either 3.33M (standard tissue) or 12M (highly metabolic tissue) HUVECs/mL and 1.67M (standard tissue) or 12M (highly metabolic tissue) NHDFs/mL. For fibrin constructs, HUVECs and NHDFs were resuspended in 20mg/mL fibrinogen (Millipore-Sigma) and combined 1:1 with 2.5U/mL thrombin (Millipore-Sigma) before casting around the sacrificial isomalt template. Fibrin tissues were incubated at 37°C for 30 minutes to fully set before template evacuation. For GelMA constructs, HUVECs and NHDFs were suspended in either 5% or 15% GelMA prepolymers with 10mM lithium phenyl (2,4,6-trimethylbenzoyl) phosphinate (LAP) photoinitiator. GelMA prepolymers were cast around sacrificial isomalt templates and cured using 405nm near-UV light for 1-2 minutes. GelMA tissues were incubated at 37°C for 30 minutes to fully set before template evacuation. Isomalt templates were evacuated from within the tissues by flushing the channels with warm PBS using syringes with flexible blunt catheter tips (Nordson EFD; 25GA). Following complete evacuation of the isomalt, fibrin and GelMA constructs were catheterized in chambers with 25GA leur lock flexible dispensing tips (Nordson). EBM2 (Lonza) was gently dropped onto catheterized hydrogels before sealing the chamber.

4.4.5 *Patterning of endothelial collagen tracks*

Sealed chambers were placed on a cooled (4°C) stainless steel block for 15 minutes before cell slurry injection to prevent premature collagen polymerization during injection. 10M HUVECs/mL and 0.2M C3H10T1/2s/mL were resuspended in a neutralized 2.5mg/mL collagen

I (Corning) solution. The cell-collagen slurry was injected into the evacuated tissues using a chilled syringe. Chambers were sealed with leur lock caps to prevent leakage and tissues were incubated at 37°C for 30 minutes to complete collagen polymerization. Tissues with tracks were then removed from the chambers and placed in EGM2 at 37°C for 3 hours for the endothelial cells to self-organize into a tubular structure around a collagen core[12]. Sacrificially templated constructs were kept on ice in EBM2 until implantation.

4.4.6 *In vivo implantation of sacrificially templated tissues*

Female nude mice (Taconic, 8-12 weeks) were used for all *in vivo* experiments. Sacrificially templated constructs were sutured to the gonadal fat pad using 5-0 silk on both ends of the constructs. Constructs were explanted after 7 days and fixed in 4% PFA for 48 hours before being moved to PBS. All animal procedures were approved by the University of Washington Institutional Animal Care and Use Committee (IACUC protocols #4388-01).

4.4.7 *3D staining, optical clearing, and imaging of explanted tissues*

Explanted constructs were incubated in a blocking solution (0.1M Tris, 1% BSA, 1% Normal Donkey Serum, 0.3% Triton x-100) overnight at room temperature followed by 24 hour incubation with 1:100 anti-human CD31/PECAM-1 DyLight 550 conjugated antibody (Clone: JC/70A, Novus) and 1:100 anti-mouse TER-119 Alexa Fluor 488 (Biolegend) conjugated antibody at 37°C on an orbital shaker. Constructs were rendered optically transparent using Clearing Enhanced 3D (Ce3D) Microscopy clearing solution with 1:500 Hoescht 33342 for 24 hours at room temperature[208]. Finally, constructs were moved into a fresh Ce3D clearing solution for 24 hours before confocal imaging. Constructs were imaged using a Nikon Ti2: AX-R scanning confocal microscope. NIS-Elements version 5.42.04 was used to obtain maximum

intensity projections and remove shot noise. For visualization purposes, we imaged a control channel and used it to remove large-image tiling artifacts.

4.4.8 *Vessel characterizations and fluorescence signal quantification*

Graft areas were obtained in ImageJ by manually tracing tissue boundaries in maximum intensity projections. Signal area and percent graft for TER119 and huCD31 were quantified in ImageJ[209] by applying a uniform threshold across maximum intensity projections, measuring positive pixel area, and dividing by total graft area to obtain percent graft. Vessel tracing was done on maximum intensity projections using Angiotool[186]. Vascular density was calculated as (Mean E Lacunarity (λ))$^{-1}$. For orientation analyses, ROIs of patterned channel regions were used to determine local orientation distribution OrientationJ[210]. Skeletonization of maximum intensity projections was done using an ImageJ plugin[211]. 3D visualization, surface rendering, depth coding, filament tracing, and diameter coding were done in Imaris software version 10.2.

4.4.9 *Statistical analysis*

All statistical analysis was done using GraphPad Prism.

4.5 Conclusions and future work

*4.5.*1 *Limitations of track containing tissues*

While track containing tissues show great promise in rapidly integrating engineered tissues with host circulation and improving implant engraftment, one limitation of track containing tissues is that the patterned channels themselves cannot be perfused immediately after fabrication or directly anastomosed to host vessels. When the tracks organize into cord-like structures, forming a lumen around aligned collagen, the tracks contract to approximately 50% of

the channel they are patterned in, and are not adhered to the patterned channels. Thus, if the patterned channels with tracks were immediately perfused, the endothelial collagen tracks would dislodge and be flushed out of the channels.

One potential remedy to this limitation is patterning two discrete networks within the same engineered tissues. This would enable direct anastomosis and blood flow to one of the patterned networks within the engineered tissue, while the other could contain patterned tracks. An additional possible approach to mitigate this obstacle is to develop methodologies that allow for interfacial seeding of the endothelial cell-collagen tracks formulation, combining the ability of tracks to guide vascularization and improve host integration with the ability to directly anastomose tracks containing tissues with host vasculature.

4.5.2 *Alternative sacrificial templating methods for future studies*

Portions of this chapter have been submitted as a research article to a peer-reviewed journal.

In this work, sacrificial isomalt templates enabled biofabrication of centimeter-scale engineered tissues with patterned tracks. However, fabrication of these templates requires highly specialized equipment and extensive training to operate. We also found printing and post-processing of the isomalt templates to be laborious, time consuming, and resulted in the loss of 40% and 60% of templates at each respective stage. (Table 4.1). Moreover, sintered isomalt is a hard, brittle material. So, while it can be dissolved with a warm saline solution, brittle filaments often dislodged and ruptured through the channel walls. When this occurs, the tissue becomes unusable in downstream studies, as isomalt evacuation will remain incomplete and any endothelial cell-collagen slurry will leak out of the patterned channels when injected.

Fabrication step	% templates lost	Reason for failure
SLS printing *(average of 3 print batches, n=32 templates each)*	44%	Broken filaments Layer distributor issues
Post-processing *(average of 2 print batches, n=32 templates each)*	66%	Broken filaments Filaments
Template evacuation *(4 in vivo experiments, average n = 12)*	17%	Ruptures Incomplete evacuation

Table 4.1 Fabrication drawbacks of sintered isomalt templates.

Given the drawbacks of this approach, we are developing an alternative sacrificial templating material system, leverage alginate to fabricate sacrificial templates. Moreover, we developed a method to accelerate template degradation by embedding microparticles with dissolution agents within the template, thus allow for global template dissolution as opposed to small surface areas accessible through the channel (Fig. 4.12). We term this approach Suspended Particles for Omnidirectional Template Sacrifice (SPOTS).

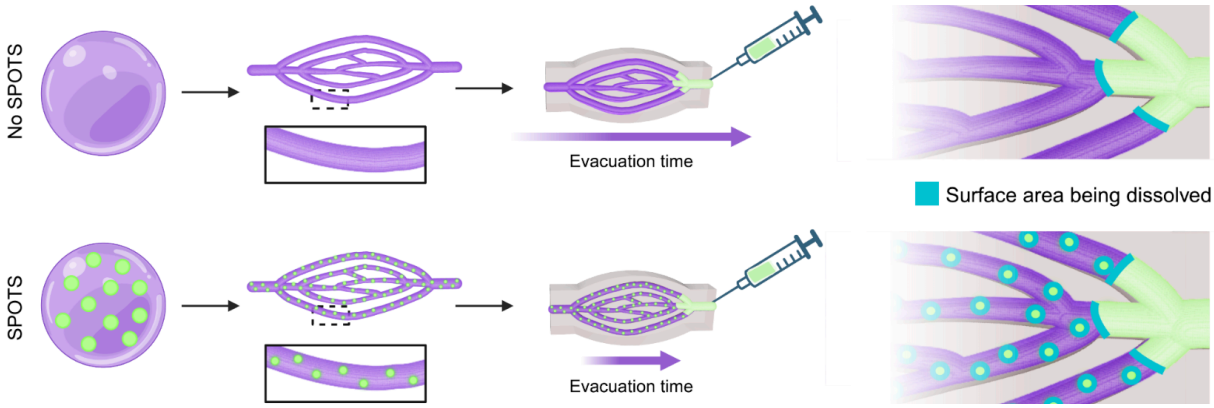

Figure 4.12. SPOTS accelerate template dissolution by increased dissolution surface area via embedding dissolution agent loaded microparticles.

No SPOTS template dissolution surface area limited to area accessible through channels (top) while SPOTS templates enable global template dissolution (bottom).

Chapter 5. CONCLUSION

The work presented here offers promising avenues for engineering tissues that rapidly integrate with host circulation upon implantation by patterning vascular promoting tracks that guide formation of chimeric vasculature *in vivo*. However, while patterning of vascular promoting, endothelial collagen tracks have proven to be a promising strategy to improve vascularization of engineered tissues, further investigation is required to reveal the exact mechanism in which the endothelial cells and collagen that makeup tracks guide formation of chimeric, host-graft vessels while improving host integration. Curiously, the organization of endothelial cells around a compacted collagen core is reminiscent of tubulogenesis occurring during vasculogenesis. Moreover, in this work we observed track guided vasculature with similar network morphologies to immature vascular plexus and to the formation of struts during de novo large vessel formation. We also observe "sprouts" emerging from patterned track associated vessels to connect with spontaneous self-assembled networks *in vivo*. Separately, recent investigations have highlighted the role of collagen basement membrane reorganization in both host-graft coupling, and regeneration of native vasculature[212,213]. Moreover, alignment of collagen fibrils has been to shown to guide endothelial cell migration *in vitro*[213–215] and facilitate invasion of tumor cells and tumor angiogenesis *in vivo*[216,217,218], highlighting the physiological relevance of the aligned collagen formed in the patterned endothelial tracks. Taken together, the patterned endothelial collagen tracks may guide formation of vasculature via mechanisms similar to those observed in de novo vascularization and thus may aid in formation of host-mediated, biomimetic vascular networks.

In all, the work presented here describes key insights and biofabrication approaches towards the goal of generating human organ scale vascular networks within engineered tissues. Importantly, advancements made here move the field close to clinical translation by scaling track-containing tissues 10-fold, generating centimeter-scale tissues that undergo volumetric vascularization when implanted. What's more, we also evaluate the role of host biology, which will be increasingly important as we scale tissues sizes and host models, as potentially damaging immune responses upon implantation should be avoided to ensure long-term success of engineered organs. To conclude, the field of tissue engineering will benefit tremendously by not only understanding host biology but leveraging host biology to aid in vascularization and engraftment of engineered, organ scale-tissues. Here, we demonstrate host-mediated vascularization and integration of large tissues, moving the field closer to engineering transplantable, human scale organs.

BIBLIOGRAPHY

1. Malkani, S., Prado, O. & Stevens, K. R. Sacrificial Templating for Accelerating Clinical Translation of Engineered Organs. *ACS Biomater. Sci. Eng.* **11**, 1–12 (2025).
2. Goldie, L. C., Nix, M. K. & Hirschi, K. K. Embryonic vasculogenesis and hematopoietic specification. *Organogenesis* **4**, 257–263 (2008).
3. Kubis, N. & Levy, B. I. Vasculogenesis and Angiogenesis: Molecular and Cellular Controls. *Interv Neuroradiol* **9**, 227–237 (2003).
4. Wang, Y. & Zhao, S. Vasculogenesis and Angiogenesis of Human Placenta. in *Vascular Biology of the Placenta* (Morgan & Claypool Life Sciences, 2010).
5. Adair, T. H. & Montani, J.-P. Overview of Angiogenesis. in *Angiogenesis* (Morgan & Claypool Life Sciences, 2010).
6. Markiewski, M. M., Daugherity, E., Reese, B. & Karbowniczek, M. The Role of Complement in Angiogenesis. *Antibodies* **9**, 67 (2020).
7. Weijts, B. *et al.* Endothelial struts enable the generation of large lumenized blood vessels de novo. *Nat Cell Biol* **23**, 322–329 (2021).
8. Schechner, J. S. *et al.* In vivo formation of complex microvessels lined by human endothelial cells in an immunodeficient mouse. *Proceedings of the National Academy of Sciences* **97**, 9191–9196 (2000).
9. Levenberg, S., Golub, J. S., Amit, M., Itskovitz-Eldor, J. & Langer, R. Endothelial cells derived from human embryonic stem cells. *Proc Natl Acad Sci U S A* **99**, 4391–4396 (2002).
10. Koike, N. *et al.* Creation of long-lasting blood vessels | Nature. *Nature* **428**, 138–139 (2004).
11. Chaturvedi, R. R. *et al.* Patterning Vascular Networks *In Vivo* for Tissue Engineering Applications. *Tissue Engineering Part C: Methods* **21**, 509–517 (2015).
12. Baranski, J. D. *et al.* Geometric control of vascular networks to enhance engineered tissue integration and function. *Proc Natl Acad Sci U S A* **110**, 7586–7591 (2013).
13. Brady, E. L. *et al.* Engineered tissue vascularization and engraftment depends on host model. *Sci Rep* **13**, 1973 (2023).
14. Stevens, K. R. *et al.* In situ expansion of engineered human liver tissue in a mouse model of chronic liver disease. *Sci. Transl. Med.* **9**, eaah5505 (2017).

15. O'Connor, C. E. *et al.* Bioprinted platform for parallelized screening of engineered microtissues *in vivo*. *Cell Stem Cell* (2025) doi:10.1016/j.stem.2025.03.002.
16. Brady, E. L. *et al.* Guided vascularization in the rat heart leads to transient vessel patterning. *APL Bioengineering* **4**, 016105 (2020).
17. Abouna, G. M. Organ Shortage Crisis: Problems and Possible Solutions. *Transplantation Proceedings* **40**, 34–38 (2008).
18. Jain, R. K., Au, P., Tam, J., Duda, D. G. & Fukumura, D. Engineering vascularized tissue. *Nature Biotechnology* **23**, 821–823 (2005).
19. Kaully, T., Kaufman-Francis, K., Lesman, A. & Levenberg, S. Vascularization--the conduit to viable engineered tissues. *Tissue Eng Part B Rev* **15**, 159–169 (2009).
20. Vunjak-Novakovic, G. *et al.* Challenges in cardiac tissue engineering. *Tissue Eng Part B Rev* **16**, 169–187 (2010).
21. Levenberg, S. *et al.* Engineering vascularized skeletal muscle tissue. *Nature Biotechnology* **23**, 879 (2005).
22. Stevens, K. R. *et al.* Physiological function and transplantation of scaffold-free and vascularized human cardiac muscle tissue. *Proc Natl Acad Sci U S A* **106**, 16568–16573 (2009).
23. White, S. M. *et al.* Longitudinal in vivo imaging to assess blood flow and oxygenation in implantable engineered tissues. *Tissue Eng Part C Methods* **18**, 697–709 (2012).
24. White, S. M. *et al.* Implanted cell-dense prevascularized tissues develop functional vasculature that supports reoxygenation after thrombosis. *Tissue Eng Part A* **20**, 2316–2328 (2014).
25. Raghavan, S., Nelson, C. M., Baranski, J. D., Lim, E. & Chen, C. S. Geometrically Controlled Endothelial Tubulogenesis in Micropatterned Gels. *Tissue Eng Part A* **16**, 2255–2263 (2010).
26. Hirschi, K. K. & D'Amore, P. A. Pericytes in the microvasculature. *Cardiovascular Research* **32**, 687–698 (1996).
27. Luttikhuizen, D. T. *et al.* The correlation between difference in foreign body reaction between implant locations and cytokine and MMP expression. *Biomaterials* **27**, 5763–5770 (2006).
28. Kellar, R. S., Kleinert, L. B. & Williams, S. K. Characterization of angiogenesis and inflammation surrounding ePTFE implanted on the epicardium. *J. Biomed. Mater. Res.* **61**, 226–233 (2002).

29. Hirschi, K. K., Rohovsky, S. A. & D'Amore, P. A. PDGF, TGF-β, and Heterotypic Cell–Cell Interactions Mediate Endothelial Cell–induced Recruitment of 10T1/2 Cells and Their Differentiation to a Smooth Muscle Fate. *Journal of Cell Biology* **141**, 805–814 (1998).

30. Cook, J. L. & Lewis, A. M. Immunological surveillance against DNA-virus-transformed cells: correlations between natural killer cell cytolytic competence and tumor susceptibility of athymic rodents. *Journal of Virology* **61**, 2155–2161 (1987).

31. Jong, W. H. D. *et al.* The athymic nude rat. III. Natural cell-mediated cytotoxicity. *Clin. Immunol. Immunopathol* 163–172 (1980).

32. Rolstad, B. The athymic nude rat: an animal experimental model to reveal novel aspects of innate immune responses? *Immunol Rev* **184**, 136–144 (2001).

33. Cheers, C. & Waller, R. Activated Macrophages in Congenitally Athymic "Nude" Mice and in Lethally Irradiated Mice. *The Journal of Immunology* **115**, 844–847 (1975).

34. Couto, G. de *et al.* Macrophages mediate cardioprotective cellular postconditioning in acute myocardial infarction. *J Clin Invest* **125**, 3147–3162 (2015).

35. Vagnozzi, R. J. *et al.* An acute immune response underlies the benefit of cardiac stem-cell therapy. *Nature* 1–1 (2019) doi:10.1038/s41586-019-1802-2.

36. Baker, M. 1,500 scientists lift the lid on reproducibility. *Nature News* **533**, 452 (2016).

37. Cossu, G. *et al.* Lancet Commission: Stem cells and regenerative medicine. *The Lancet* **391**, 883–910 (2018).

38. Zhang, M. *et al.* Cardiomyocyte Grafting for Cardiac Repair: Graft Cell Death and Anti-Death Strategies. *Journal of Molecular and Cellular Cardiology* **33**, 907–921 (2001).

39. Laflamme, M. A. *et al.* Cardiomyocytes derived from human embryonic stem cells in pro-survival factors enhance function of infarcted rat hearts. *Nat Biotechnol* **25**, 1015–1024 (2007).

40. Burridge, P. W. *et al.* Chemically Defined and Small Molecule-Based Generation of Human Cardiomyocytes. *Nat Methods* **11**, 855–860 (2014).

41. Tohyama, S. *et al.* Distinct Metabolic Flow Enables Large-Scale Purification of Mouse and Human Pluripotent Stem Cell-Derived Cardiomyocytes. *Cell Stem Cell* **12**, 127–137 (2013).

42. Li, W., Germain, R. N. & Gerner, M. Y. Multiplex, quantitative cellular analysis in large tissue volumes with clearing-enhanced 3D microscopy (Ce3D). *Proc. Natl. Acad. Sci. U.S.A.* **114**, E7321–E7330 (2017).

43. Schindelin, J. *et al.* Fiji: an open-source platform for biological-image analysis. *Nature Methods* **9**, 676–682 (2012).

44. O'Connor, C., Brady, E., Zheng, Y., Moore, E. & Stevens, K. R. Engineering the multiscale complexity of vascular networks. *Nat Rev Mater* **7**, 702–716 (2022).

45. Li, S., Li, H., Shang, X., He, J. & Hu, Y. Recent advances in 3D printing sacrificial templates for fabricating engineered vasculature. *MedComm – Biomaterials and Applications* **2**, e46 (2023).

46. Inbody, S. C., Sinquefield, B. E., Lewis, J. P. & Horton, R. E. Biomimetic microsystems for cardiovascular studies. *American Journal of Physiology-Cell Physiology* **320**, C850–C872 (2021).

47. Jose, R. R., Rodriguez, M. J., Dixon, T. A., Omenetto, F. & Kaplan, D. L. Evolution of Bioinks and Additive Manufacturing Technologies for 3D Bioprinting. *ACS Biomater. Sci. Eng.* **2**, 1662–1678 (2016).

48. Murphy, S. V. & Atala, A. 3D bioprinting of tissues and organs. *Nat Biotechnol* **32**, 773–785 (2014).

49. Raees, S. *et al.* Classification, processing, and applications of bioink and 3D bioprinting: A detailed review. *International Journal of Biological Macromolecules* **232**, 123476 (2023).

50. Kirillova, A., Maxson, R., Stoychev, G., Gomillion, C. T. & Ionov, L. 4D Biofabrication Using Shape-Morphing Hydrogels. *Advanced Materials* **29**, 1703443 (2017).

51. Chaji, S., Al-Saleh, J. & Gomillion, C. T. Bioprinted Three-Dimensional Cell-Laden Hydrogels to Evaluate Adipocyte-Breast Cancer Cell Interactions. *Gels* **6**, 10 (2020).

52. Xu, H.-Q., Liu, J.-C., Zhang, Z.-Y. & Xu, C.-X. A review on cell damage, viability, and functionality during 3D bioprinting. *Military Medical Research* **9**, 70 (2022).

53. Zheng, F., Wang, Z., Huang, J. & Li, Z. Inkjet printing-based fabrication of microscale 3D ice structures. *Microsyst Nanoeng* **6**, 1–10 (2020).

54. Grigoryan, B. *et al.* Multivascular networks and functional intravascular topologies within biocompatible hydrogels. *Science* **364**, 458–464 (2019).

55. Li, S., Liu, S. & Wang, X. Advances of 3D Printing in Vascularized Organ Construction. *IJB* **8**, 588 (2022).

56. Datta, P., Ayan, B. & Ozbolat, I. T. Bioprinting for vascular and vascularized tissue biofabrication. *Acta Biomaterialia* **51**, 1–20 (2017).

57. Corbett, D. C. *et al.* Thermofluidic heat exchangers for actuation of transcription in artificial tissues. *Sci Adv* **6**, eabb9062 (2020).

58. Pedroza-González, S. C., Rodriguez-Salvador, M., Pérez-Benítez, B. E., Alvarez, M. M. & Santiago, G. T. Bioinks for 3D Bioprinting: A Scientometric Analysis of Two Decades of Progress. *Int J Bioprint* **7**, 333 (2021).

59. Fontes, A. B. & Marcomini, R. F. 3D Bioprinting: a review of materials, processes and bioink properties. *The Journal of Engineering and Exact Sciences* **6**, 0617–0639 (2020).

60. Pati, F., Gantelius, J. & Svahn, H. A. 3D Bioprinting of Tissue/Organ Models. *Angewandte Chemie International Edition* **55**, 4650–4665 (2016).

61. Kačarević, Ž. P. *et al.* An Introduction to 3D Bioprinting: Possibilities, Challenges and Future Aspects. *Materials* **11**, 2199 (2018).

62. Panda, S. *et al.* A focused review on three-dimensional bioprinting technology for artificial organ fabrication. *Biomaterials Science* **10**, 5054–5080 (2022).

63. Corbett, D. C., Olszewski, E. & Stevens, K. A FRESH Take on Resolution in 3D Bioprinting. *Trends Biotechnol* **37**, 1153–1155 (2019).

64. Lenihan, C. R. & Taylor, C. T. The impact of hypoxia on cell death pathways. *Biochemical Society Transactions* **41**, 657–663 (2013).

65. McGarry, T., Biniecka, M., Veale, D. J. & Fearon, U. Hypoxia, oxidative stress and inflammation. *Free Radical Biology and Medicine* **125**, 15–24 (2018).

66. Han, S., Kim, C. M., Jin, S. & Kim, T. Y. Study of the process-induced cell damage in forced extrusion bioprinting. *Biofabrication* **13**, (2021).

67. Blaeser, A. *et al.* Controlling Shear Stress in 3D Bioprinting is a Key Factor to Balance Printing Resolution and Stem Cell Integrity. *Advanced Healthcare Materials* **5**, 326–333 (2016).

68. Köpf, M., Nasehi, R., Kreimendahl, F., Jockenhoevel, S. & Fischer, H. Bioprinting-Associated Shear Stress and Hydrostatic Pressure Affect the Angiogenic Potential of Human Umbilical Vein Endothelial Cells. *Int J Bioprint* **8**, 606 (2022).

69. Adhikari, J. *et al.* Effects of Processing Parameters of 3D Bioprinting on the Cellular Activity of Bioinks. *Macromolecular Bioscience* **21**, 2000179 (2021).

70. Ng, W. L. *et al.* Controlling Droplet Impact Velocity and Droplet Volume: Key Factors to Achieving High Cell Viability in Sub-Nanoliter Droplet-based Bioprinting. *Int J Bioprint* **8**, 424 (2021).

71. Nieto, D., Marchal Corrales, J. A., Jorge de Mora, A. & Moroni, L. Fundamentals of light-cell–polymer interactions in photo-cross-linking based bioprinting. *APL Bioeng* **4**, 041502 (2020).

72. de Gruijl, F. R., van Kranen, H. J. & Mullenders, L. H. UV-induced DNA damage, repair, mutations and oncogenic pathways in skin cancer. *J Photochem Photobiol B* **63**, 19–27 (2001).

73. Sinha, R. P. & Häder, D.-P. UV-induced DNA damage and repair: a review. *Photochem. Photobiol. Sci.* **1**, 225–236 (2002).

74. Chin, K. C. H., Ovsepyan, G. & Boydston, A. J. Multi-color dual wavelength vat photopolymerization 3D printing via spatially controlled acidity. *Nat Commun* **15**, 3867 (2024).

75. LaValley, D. J. & Reinhart-King, C. A. Matrix stiffening in the formation of blood vessels. *Advances in Regenerative Biology* **1**, 25247 (2014).

76. Guimarães, C. F., Gasperini, L., Marques, A. P. & Reis, R. L. The stiffness of living tissues and its implications for tissue engineering. *Nat Rev Mater* **5**, 351–370 (2020).

77. Lee, S. *et al.* Contractile force generation by 3D hiPSC-derived cardiac tissues is enhanced by rapid establishment of cellular interconnection in matrix with muscle-mimicking stiffness. *Biomaterials* **131**, 111–120 (2017).

78. Sasikumar, S., Chameettachal, S., Cromer, B., Pati, F. & Kingshott, P. Decellularized extracellular matrix hydrogels—cell behavior as a function of matrix stiffness. *Current Opinion in Biomedical Engineering* **10**, 123–133 (2019).

79. Chaudhuri, O., Cooper-White, J., Janmey, P. A., Mooney, D. J. & Shenoy, V. B. Effects of extracellular matrix viscoelasticity on cellular behaviour. *Nature* **584**, 535–546 (2020).

80. Li, W. *et al.* Matrix stiffness and shear stresses modulate hepatocyte functions in a fibrotic liver sinusoidal model. *American Journal of Physiology-Gastrointestinal and Liver Physiology* **320**, G272–G282 (2021).

81. Desai, S. S. *et al.* Physiological ranges of matrix rigidity modulate primary mouse hepatocyte function in part through hepatocyte nuclear factor 4 alpha. *Hepatology* **64**, 261 (2016).

82. Dickinson, L. E., Rand, D. R., Tsao, J., Eberle, W. & Gerecht, S. Endothelial cell responses to micropillar substrates of varying dimensions and stiffness. *Journal of Biomedical Materials Research Part A* **100A**, 1457–1466 (2012).

83. Shen, Y.-I. *et al.* Hyaluronic acid hydrogel stiffness and oxygen tension affect cancer cell fate and endothelial sprouting. *Biomater. Sci.* **2**, 655–665 (2014).

84. Mirdamadi, E., Tashman, J. W., Shiwarski, D. J., Palchesko, R. N. & Feinberg, A. W. FRESH 3D Bioprinting a Full-Size Model of the Human Heart. *ACS Biomater Sci Eng* **6**, 6453–6459 (2020).

85. Kinstlinger, I. S. *et al.* Generation of model tissues with dendritic vascular networks via sacrificial laser-sintered carbohydrate templates. *Nature Biomedical Engineering* **4**, 916–932 (2020).

86. Wang, Y. *et al.* Direct writing alginate bioink inside pre-polymers of hydrogels to create patterned vascular networks. *J Mater Sci* **54**, 7883–7892 (2019).

87. Skylar-Scott, M. A. *et al.* Biomanufacturing of organ-specific tissues with high cellular density and embedded vascular channels. *Science Advances* **5**, eaaw2459 (2019).

88. Lee, V. K. *et al.* Creating perfused functional vascular channels using 3D bio-printing technology. *Biomaterials* **35**, 8092–8102 (2014).

89. Lee, V. K. *et al.* Generation of Multi-scale Vascular Network System Within 3D Hydrogel Using 3D Bio-printing Technology. *Cel. Mol. Bioeng.* **7**, 460–472 (2014).

90. Orellano, I. *et al.* Engineering Vascular Self-Assembly by Controlled 3D-Printed Cell Placement. *Advanced Functional Materials* **32**, 2208325 (2022).

91. Golden, A. P. & Tien, J. Fabrication of microfluidic hydrogels using molded gelatin as a sacrificial element. *Lab Chip* **7**, 720–725 (2007).

92. Duchamp, M. *et al.* Sacrificial Bioprinting of a Mammary Ductal Carcinoma Model. *Biotechnology Journal* **14**, 1700703 (2019).

93. Garg, A., Yerneni, S. S., Campbell, P., LeDuc, P. R. & Ozdoganlar, O. B. Freeform 3D Ice Printing (3D-ICE) at the Micro Scale. *Advanced Science* **9**, 2201566 (2022).

94. Liu, T. *et al.* Investigating lymphangiogenesis in a sacrificially bioprinted volumetric model of breast tumor tissue. *Methods* **190**, 72–79 (2021).

95. Moeun, B. N. *et al.* Improving the 3D Printability of Sugar Glass to Engineer Sacrificial Vascular Templates. *3D Printing and Additive Manufacturing* **10**, 869–886 (2023).

96. Tocchio, A. *et al.* Versatile fabrication of vascularizable scaffolds for large tissue engineering in bioreactor. *Biomaterials* **45**, 124–131 (2015).

97. Pan, B. *et al.* 3D printing sacrificial templates for manufacturing hydrogel constructs with channel networks. *Materials & Design* **222**, 111012 (2022).

98. Doyle, S. E. *et al.* Printing between the Lines: Intricate Biomaterial Structures Fabricated via Negative Embodied Sacrificial Template 3D (NEST3D) Printing. *Advanced Materials Technologies* **6**, 2100189 (2021).

99. Gergely, R. C. R. *et al.* Multidimensional Vascularized Polymers using Degradable Sacrificial Templates. *Advanced Functional Materials* **25**, 1043–1052 (2015).

100. Sooppan, R. *et al.* In Vivo Anastomosis and Perfusion of a Three-Dimensionally-Printed Construct Containing Microchannel Networks. *Tissue Engineering Part C: Methods* **22**, 1–7 (2016).

101. Ahn, M. *et al.* Engineering of Uniform Epidermal Layers via Sacrificial Gelatin Bioink-Assisted 3D Extrusion Bioprinting of Skin. *Advanced Healthcare Materials* **12**, 2301015 (2023).

102. Jacoby, A. *et al.* Fabrication of capillary-like structures with Pluronic F127® and Kerria lacca resin (shellac) in biocompatible tissue-engineered constructs. *Journal of Tissue Engineering and Regenerative Medicine* **11**, 2388–2397 (2017).

103. Lee, J. B. *et al.* Development of 3D Microvascular Networks Within Gelatin Hydrogels Using Thermoresponsive Sacrificial Microfibers. *Advanced Healthcare Materials* **5**, 781–785 (2016).

104. Martin, C., Sofia, A., Zhang, B., Nunes, S. S. & Radisic, M. Fusible Core Molding for the Fabrication of Branched, Perfusable, Three-Dimensional Microvessels for Vascular Tissue Engineering. *Int J Artif Organs* **36**, 159–165 (2013).

105. Huling, J., Ko, I. K., Atala, A. & Yoo, J. J. Fabrication of biomimetic vascular scaffolds for 3D tissue constructs using vascular corrosion casts. *Acta Biomaterialia* **32**, 190–197 (2016).

106. Li, S., Wang, K., Hu, Q., Zhang, C. & Wang, B. Direct-write and sacrifice-based techniques for vasculatures. *Materials Science and Engineering: C* **104**, 109936 (2019).

107. Ozdemir, S., Yalcin-Enis, I., Yalcinkaya, B. & Yalcinkaya, F. An Investigation of the Constructional Design Components Affecting the Mechanical Response and Cellular Activity of Electrospun Vascular Grafts. *Membranes* **12**, 929 (2022).

108. Kolesky, D. B., Homan, K. A., Skylar-Scott, M. A. & Lewis, J. A. Three-dimensional bioprinting of thick vascularized tissues. *Proceedings of the National Academy of Sciences* **113**, 3179–3184 (2016).

109. Lammers, A. *et al.* Rapid tissue perfusion using sacrificial percolation of anisotropic networks. *Matter* **7**, 2184–2204 (2024).

110. McNulty, J. D. *et al.* Micro-injection molded, poly(vinyl alcohol)-calcium salt templates for precise customization of 3D hydrogel internal architecture. *Acta Biomaterialia* **95**, 258–268 (2019).

111. Huang, A. *et al.* Fabrication of poly(ε-caprolactone) tissue engineering scaffolds with fibrillated and interconnected pores utilizing microcellular injection molding and polymer leaching. *RSC Adv.* **7**, 43432–43444 (2017).

112. Cui, Z. *et al.* Fabrication and characterization of injection molded poly (ε-caprolactone) and poly (ε-caprolactone)/hydroxyapatite scaffolds for tissue engineering. *Materials Science and Engineering: C* **32**, 1674–1681 (2012).

113. Bellan, L. M. *et al.* Fabrication of an artificial 3-dimensional vascular network using sacrificial sugar structures. *Soft Matter* **5**, 1354–1357 (2009).

114. Eltaher, H. M. *et al.* Human-scale tissues with patterned vascular networks by additive manufacturing of sacrificial sugar-protein composites. *Acta Biomaterialia* **113**, 339–349 (2020).

115. Brunel, L. G., Hull, S. M. & Heilshorn, S. C. Engineered assistive materials for 3D bioprinting: support baths and sacrificial inks. *Biofabrication* **14**, 10.1088/1758-5090/ac6bbe (2022).

116. Lee, J. B. *et al.* Microchannel network hydrogel induced ischemic blood perfusion connection. *Nat Commun* **11**, 615 (2020).

117. Bellan, L. M., Pearsall, M., Cropek, D. M. & Langer, R. A 3D Interconnected Microchannel Network Formed in Gelatin by Sacrificial Shellac Microfibers. *Advanced Materials* **24**, 5187–5191 (2012).

118. Li, S. *et al.* Rapid Fabrication of Ready-to-Use Gelatin Scaffolds with Prevascular Networks Using Alginate Hollow Fibers as Sacrificial Templates. *ACS Biomater. Sci. Eng.* **6**, 2297–2311 (2020).

119. Saeki, K. *et al.* Sacrificial Alginate-Assisted Microfluidic Engineering of Cell-Supportive Protein Microfibers for Hydrogel-Based Cell Encapsulation. *ACS Omega* **5**, 21641–21650 (2020).

120. Azueta-Aguayo, P. H. *et al.* Effects of Neutralization on the Physicochemical, Mechanical, and Biological Properties of Ammonium-Hydroxide-Crosslinked Chitosan Scaffolds. *International Journal of Molecular Sciences* **23**, 14822 (2022).

121. Koulaouzidou, E. A., Margelos, J., Beltes, P. & Kortsaris, A. H. Cytotoxic effects of different concentrations of neutral and alkaline EDTA solutions used as root canal irrigants. *Journal of Endodontics* **25**, 21–23 (1999).

122. Marins, J. S. R., Sassone, L. M., Fidel, S. R. & Ribeiro, D. A. In vitro genotoxicity and cytotoxicity in murine fibroblasts exposed to EDTA, NaOCl, MTAD and citric acid. *Braz. Dent. J.* **23**, 527–533 (2012).

123. Davoodi, E. *et al.* Template-Enabled Biofabrication of Thick 3D Tissues with Patterned Perfusable Macrochannels. *Advanced Healthcare Materials* **11**, 2102123 (2022).

124. Arif, Z. U. *et al.* Recent advances in 3D-printed polylactide and polycaprolactone-based biomaterials for tissue engineering applications. *International Journal of Biological Macromolecules* **218**, 930–968 (2022).

125. Patrício, T. *et al.* Fabrication and characterisation of PCL and PCL/PLA scaffolds for tissue engineering. *Rapid Prototyping Journal* **20**, 145–156 (2014).

126. Linnes, M. P., Ratner, B. D. & Giachelli, C. M. A fibrinogen-based precision microporous scaffold for tissue engineering. *Biomaterials* **28**, 5298–5306 (2007).

127. Wang, J. *et al.* The synthesis and simulations of solvent-responsive bilayer hydrogel. *Polymer* **204**, 122801 (2020).

128. Augustin, H. G. & Koh, G. Y. Organotypic vasculature: From descriptive heterogeneity to functional pathophysiology. *Science* **357**, eaal2379 (2017).

129. Fu, J. & Wang, D.-A. In Situ Organ-Specific Vascularization in Tissue Engineering. *Trends Biotechnol* **36**, 834–849 (2018).

130. Secomb, T. W. Hemodynamics. *Compr Physiol* **6**, 975–1003 (2016).

131. Joyner, W. L. & Davis, M. J. Pressure profile along the microvascular network and its control. *Fed Proc* **46**, 266–269 (1987).

132. Ardakani, A. G., Cheema, U., Brown, R. A. & Shipley, R. J. Quantifying the correlation between spatially defined oxygen gradients and cell fate in an engineered three-dimensional culture model. *Journal of The Royal Society Interface* **11**, 20140501 (2014).

133. Lewis, D. M., Blatchley, M. R., Park, K. M. & Gerecht, S. O2-controllable hydrogels for studying cellular responses to hypoxic gradients in three dimensions in vitro and in vivo. *Nat Protoc* **12**, 1620–1638 (2017).

134. Thomas, D. D., Liu, X., Kantrow, S. P. & Lancaster, J. R. The biological lifetime of nitric oxide: Implications for the perivascular dynamics of NO and O2. *Proceedings of the National Academy of Sciences* **98**, 355–360 (2001).

135. Allen, J. W. & Bhatia, S. N. Formation of steady-state oxygen gradients in vitro: Application to liver zonation. *Biotechnology and Bioengineering* **82**, 253–262 (2003).

136. Singh, M., Berkland, C. & Detamore, M. S. Strategies and Applications for Incorporating Physical and Chemical Signal Gradients in Tissue Engineering. *Tissue Engineering Part B: Reviews* **14**, 341–366 (2008).

137. Panday, R., Monckton, C. P. & Khetani, S. R. The Role of Liver Zonation in Physiology, Regeneration, and Disease. *Seminars in Liver Disease* **42**, 001–016 (2022).

138. Kietzmann, T. Metabolic zonation of the liver: The oxygen gradient revisited. *Redox Biology* **11**, 622–630 (2017).

139. Bertassoni, L. E. *et al.* Hydrogel bioprinted microchannel networks for vascularization of tissue engineering constructs. *Lab Chip* **14**, 2202–2211 (2014).

140. Chrobak, K. M., Potter, D. R. & Tien, J. Formation of perfused, functional microvascular tubes in vitro. *Microvasc Res* **71**, 185–196 (2006).

141. Daghighi, Y., Heidari, H. & Taylor, H. Micro-engineering a platform to reconstruct physiology and functionality of the human brain microvasculature in vitro. in *Microfluidics, BioMEMS, and Medical Microsystems XVI* vol. 10491 96–107 (SPIE, 2018).

142. Wong, K. H. K., Truslow, J. G. & Tien, J. The Role of Cyclic AMP in Normalizing the Function of Engineered Human Blood Microvessels in Microfluidic Collagen Gels. *Biomaterials* **31**, 4706–4714 (2010).

143. Miller, J. S. *et al.* Rapid casting of patterned vascular networks for perfusable engineered three-dimensional tissues. *Nature Mater* **11**, 768–774 (2012).

144. Han, H.-C. Twisted Blood Vessels: Symptoms, Etiology and Biomechanical Mechanisms. *J Vasc Res* **49**, 185–197 (2012).

145. Bosetti, F. *et al.* "Small Blood Vessels: Big Health Problems?": Scientific Recommendations of the National Institutes of Health Workshop. *Journal of the American Heart Association* **5**, e004389 (2016).

146. Sharma, D. *et al.* Upgrading prevascularization in tissue engineering: A review of strategies for promoting highly organized microvascular network formation. *Acta Biomaterialia* **95**, 112–130 (2019).

147. Son, J. *et al.* Engineering Tissue-Specific, Multiscale Microvasculature with a Capillary Network for Prevascularized Tissue. *Small Methods* **5**, e2100632 (2021).

148. Zheng, Y. *et al.* In vitro microvessels for the study of angiogenesis and thrombosis. *Proceedings of the National Academy of Sciences* **109**, 9342–9347 (2012).

149. Liu, W. *et al.* Coaxial extrusion bioprinting of 3D microfibrous constructs with cell-favorable gelatin methacryloyl microenvironments. *Biofabrication* **10**, 024102 (2018).

150. Fortin, C. L. *et al.* Temporal Dynamics of Metabolic Acquisition in Grafted Engineered Human Liver Tissue. *Advanced Biology* **7**, 2200208 (2023).

151. Song, J. & Gerecht, S. Hydrogels to Recapture Extracellular Matrix Cues That Regulate Vascularization. *Arteriosclerosis, Thrombosis, and Vascular Biology* **43**, e291–e302 (2023).

152. Koike, N. *et al.* Creation of long-lasting blood vessels. *Nature* **428**, 138–139 (2004).

153. Debbi, L. *et al.* Integrating engineered macro vessels with self-assembled capillaries in 3D implantable tissue for promoting vascular integration in-vivo. *Biomaterials* **280**, 121286 (2022).

154. Hooper, R. C. *et al.* Fabrication and In Vivo Microanastomosis of Vascularized Tissue-Engineered Constructs. *Tissue Engineering Part A* **20**, 2711–2719 (2014).

155. Szklanny, A. A. *et al.* 3D Bioprinting of Engineered Tissue Flaps with Hierarchical Vessel Networks (VesselNet) for Direct Host-To-Implant Perfusion. *Advanced Materials* **33**, 2102661 (2021).

156. Gasser, T. C., Ogden, R. W. & Holzapfel, G. A. Hyperelastic modelling of arterial layers with distributed collagen fibre orientations. *Journal of The Royal Society Interface* **3**, 15–35 (2005).

157. Chen, E. P., Toksoy, Z., Davis, B. A. & Geibel, J. P. 3D Bioprinting of Vascularized Tissues for in vitro and in vivo Applications. *Front. Bioeng. Biotechnol.* **9**, (2021).

158. Ben-Shaul, S., Landau, S., Merdler, U. & Levenberg, S. Mature vessel networks in engineered tissue promote graft–host anastomosis and prevent graft thrombosis. *Proc. Natl. Acad. Sci. U.S.A.* **116**, 2955–2960 (2019).

159. Lindeman, J. H. N. *et al.* Distinct defects in collagen microarchitecture underlie vessel-wall failure in advanced abdominal aneurysms and aneurysms in Marfan syndrome. *Proceedings of the National Academy of Sciences* **107**, 862–865 (2010).

160. Silva, J. M., Custódio, C. A., Reis, R. L. & Mano, J. F. Multilayered Hollow Tubes as Blood Vessel Substitutes. *ACS Biomater. Sci. Eng.* **2**, 2304–2314 (2016).

161. Ching, T. *et al.* Biomimetic Vasculatures by 3D-Printed Porous Molds. *Small* **18**, 2203426 (2022).

162. Ouyang, L., Burdick, J. A. & Sun, W. Facile Biofabrication of Heterogeneous Multilayer Tubular Hydrogels by Fast Diffusion-Induced Gelation. *ACS Appl. Mater. Interfaces* **10**, 12424–12430 (2018).

163. Li, X., Xu, J., Bartolák-Suki, E., Jiang, J. & Tien, J. Evaluation of 1-mm-diameter endothelialized dense collagen tubes in vascular microsurgery. *Journal of Biomedical Materials Research Part B: Applied Biomaterials* **108**, 2441–2449 (2020).

164. Yazdani, A., Li, H., Humphrey, J. D. & Karniadakis, G. E. A General Shear-Dependent Model for Thrombus Formation. *PLOS Computational Biology* **13**, e1005291 (2017).

165. Sohn, S., Buskirk, M. V., Buckenmeyer, M. J., Londono, R. & Faulk, D. Whole Organ Engineering: Approaches, Challenges, and Future Directions. *Applied Sciences* **10**, 4277 (2020).

166. Skylar-Scott, M. A. *et al.* Biomanufacturing of organ-specific tissues with high cellular density and embedded vascular channels. *Science Advances* **5**, eaaw2459 (2019).

167. Kolesky, D. B., Homan, K. A., Skylar-Scott, M. A. & Lewis, J. A. Three-dimensional bioprinting of thick vascularized tissues. *Proceedings of the National Academy of Sciences* **113**, 3179–3184 (2016).

168. Mirdamadi, E., Tashman, J. W., Shiwarski, D. J., Palchesko, R. N. & Feinberg, A. W. FRESH 3D Bioprinting a Full-Size Model of the Human Heart. *ACS Biomater Sci Eng* **6**, 6453–6459 (2020).

169. Szklanny, A. A. *et al.* 3D Bioprinting of Engineered Tissue Flaps with Hierarchical Vessel Networks (VesselNet) for Direct Host-To-Implant Perfusion. *Advanced Materials* **33**, 2102661 (2021).

170. Garg, A., Yerneni, S. S., Campbell, P., LeDuc, P. R. & Ozdoganlar, O. B. Freeform 3D Ice Printing (3D-ICE) at the Micro Scale. *Advanced Science* **9**, 2201566 (2022).

171. Corbett, D. C. *et al.* Thermofluidic heat exchangers for actuation of transcription in artificial tissues. *Sci Adv* **6**, eabb9062 (2020).

172. Grigoryan, B. *et al.* Multivascular networks and functional intravascular topologies within biocompatible hydrogels. *Science* **364**, 458–464 (2019).

173. Wang, M. *et al.* Molecularly cleavable bioinks facilitate high-performance digital light processing-based bioprinting of functional volumetric soft tissues. *Nat Commun* **13**, 3317 (2022).

174. O'Connor, C. E. *et al.* Bioprinted platform for parallelized screening of engineered microtissues in vivo. *Cell Stem Cell* S193459092500092X (2025) doi:10.1016/j.stem.2025.03.002.

175. Sundaram, S. *et al.* Sacrificial capillary pumps to engineer multiscalar biological forms. *Nature* **636**, 361–367 (2024).

176. Lammers, A. *et al.* Rapid tissue perfusion using sacrificial percolation of anisotropic networks. *Matter* **7**, 2184–2204 (2024).

177. Fu, Z. *et al.* Printability in extrusion bioprinting. *Biofabrication* **13**, 033001 (2021).

178. Seo, J. W., Kim, G. M., Choi, Y., Cha, J. M. & Bae, H. Improving Printability of Digital-Light-Processing 3D Bioprinting via Photoabsorber Pigment Adjustment. *International Journal of Molecular Sciences* **23**, 5428 (2022).

179. Kinstlinger, I. S. *et al.* Open-Source Selective Laser Sintering (OpenSLS) of Nylon and Biocompatible Polycaprolactone. *PLOS ONE* **11**, e0147399 (2016).

180. Shaikh, F. M. *et al.* Fibrin: A Natural Biodegradable Scaffold in Vascular Tissue Engineering. *Cells Tissues Organs* **188**, 333–346 (2008).

181. Chen, X. *et al.* Prevascularization of a Fibrin-Based Tissue Construct Accelerates the Formation of Functional Anastomosis with Host Vasculature. *Tissue Engineering Part A* **15**, 1363–1371 (2009).

182. Rao, R. R., Peterson, A. W., Ceccarelli, J., Putnam, A. J. & Stegemann, J. P. Matrix composition regulates three-dimensional network formation by endothelial cells and mesenchymal stem cells in collagen/fibrin materials. *Angiogenesis* **15**, 253–264 (2012).

183. Yue, K. *et al.* Synthesis, properties, and biomedical applications of gelatin methacryloyl (GelMA) hydrogels. *Biomaterials* **73**, 254–271 (2015).

184. Im, G.-B. & Lin, R.-Z. Bioengineering for vascularization: Trends and directions of photocrosslinkable gelatin methacrylate hydrogels. *Front. Bioeng. Biotechnol.* **10**, 1053491 (2022).

185. Heltmann-Meyer, S. *et al.* Gelatin methacryloyl is a slow degrading material allowing vascularization and long-term use in vivo. *Biomed. Mater.* **16**, 065004 (2021).

186. Zudaire, E., Gambardella, L., Kurcz, C. & Vermeren, S. A Computational Tool for Quantitative Analysis of Vascular Networks. *PLOS ONE* **6**, e27385 (2011).

187. Distler, T. *et al.* Mechanical properties of cell- and microgel bead-laden oxidized alginate-gelatin hydrogels. *Biomater. Sci.* **9**, 3051–3068 (2021).

188. Chaudhuri, O., Cooper-White, J., Janmey, P. A., Mooney, D. J. & Shenoy, V. B. Effects of extracellular matrix viscoelasticity on cellular behaviour. *Nature* **584**, 535–546 (2020).

189. LaValley, D. J. & Reinhart-King, C. A. Matrix stiffening in the formation of blood vessels. *Advances in Regenerative Biology* **1**, 25247 (2014).

190. Datta, P., Ayan, B. & Ozbolat, I. T. Bioprinting for vascular and vascularized tissue biofabrication. *Acta Biomaterialia* **51**, 1–20 (2017).

191. Shin, H., Jo, S. & Mikos, A. G. Biomimetic materials for tissue engineering. *Biomaterials* **24**, 4353–4364 (2003).

192. White, S. M. *et al.* Longitudinal *In Vivo* Imaging to Assess Blood Flow and Oxygenation in Implantable Engineered Tissues. *Tissue Engineering Part C: Methods* **18**, 697–709 (2012).

193. White, S. M. *et al.* Implanted Cell-Dense Prevascularized Tissues Develop Functional Vasculature That Supports Reoxygenation After Thrombosis. *Tissue Engineering Part A* **20**, 2316–2328 (2014).

194. Mehdizadeh, H. *et al.* Agent-based modeling of porous scaffold degradation and vascularization: Optimal scaffold design based on architecture and degradation dynamics. *Acta Biomaterialia* **27**, 167–178 (2015).

195. Augustin, H. G. & Koh, G. Y. Organotypic vasculature: From descriptive heterogeneity to functional pathophysiology. *Science* **357**, eaal2379 (2017).

196. Przysinda, A., Feng, W. & Li, G. Diversity of Organism-Wide and Organ-Specific Endothelial Cells. *Curr Cardiol Rep* **22**, 19 (2020).

197. Koch, P.-S., Lee, K. H., Goerdt, S. & Augustin, H. G. Angiodiversity and organotypic functions of sinusoidal endothelial cells. *Angiogenesis* **24**, 289–310 (2021).

198. Marcu, R. *et al.* Human Organ-Specific Endothelial Cell Heterogeneity. *iScience* **4**, 20–35 (2018).

199. Wang, X. *et al.* Construction of functional tissue-engineered microvasculatures using circulating fibrocytes as mural cells. *J Tissue Eng* **16**, 20417314251315523 (2025).

200. Costa-Almeida, R. *et al.* Fibroblast-Endothelial Partners for Vascularization Strategies in Tissue Engineering. *Tissue Engineering Part A* **21**, 1055–1065 (2015).

201. Bhang, S. H., Lee, S., Shin, J.-Y., Lee, T.-J. & Kim, B.-S. Transplantation of Cord Blood Mesenchymal Stem Cells as Spheroids Enhances Vascularization. *Tissue Engineering Part A* **18**, 2138–2147 (2012).

202. Melchiorri, A. J., Nguyen, B.-N. B. & Fisher, J. P. Mesenchymal Stem Cells: Roles and Relationships in Vascularization. *Tissue Engineering Part B: Reviews* **20**, 218–228 (2014).

203. Holm, A., Heumann, T. & Augustin, H. G. Microvascular Mural Cell Organotypic Heterogeneity and Functional Plasticity. *Trends in Cell Biology* **28**, 302–316 (2018).

204. Wang, Z. *et al.* Rapid vascularization of tissue-engineered vascular grafts in vivo by endothelial cells in co-culture with smooth muscle cells. *J Mater Sci: Mater Med* **23**, 1109–1117 (2012).

205. Regier, M. C. *et al.* User-defined morphogen patterning for directing human cell fate stratification. *Sci Rep* **9**, 6433 (2019).

206. Shadish, J. A., Benuska, G. M. & DeForest, C. A. Bioactive site-specifically modified proteins for 4D patterning of gel biomaterials. *Nat. Mater.* **18**, 1005–1014 (2019).

207. Kinstlinger, I. S. *et al.* Perfusion and endothelialization of engineered tissues with patterned vascular networks. *Nat Protoc* **16**, 3089–3113 (2021).

208. Li, W., Germain, R. N. & Gerner, M. Y. High-dimensional cell-level analysis of tissues with Ce3D multiplex volume imaging. *Nat Protoc* **14**, 1708–1733 (2019).

209. Schneider, C. A., Rasband, W. S. & Eliceiri, K. W. NIH Image to ImageJ: 25 years of image analysis. *Nat Methods* **9**, 671–675 (2012).

210. Püspöki, Z., Storath, M., Sage, D. & Unser, M. Transforms and Operators for Directional Bioimage Analysis: A Survey. in *Focus on Bio-Image Informatics* (eds. De Vos, W. H., Munck, S. & Timmermans, J.-P.) vol. 219 69–93 (Springer International Publishing, Cham, 2016).

211. Sato, Y. *et al.* Three-dimensional multi-scale line filter for segmentation and visualization of curvilinear structures in medical images. *Med Image Anal* **2**, 143–168 (1998).

212. Cheng, G. *et al.* Engineered blood vessel networks connect to host vasculature via wrapping-and-tapping anastomosis. *Blood* **118**, 4740–4749 (2011).

213. Senk, A. & Djonov, V. Collagen fibers provide guidance cues for capillary regrowth during regenerative angiogenesis in zebrafish. *Sci Rep* **11**, 19520 (2021).

214. Lai, E. S., Huang, N. F., Cooke, J. P. & Fuller, G. G. Aligned Nanofibrillar Collagen Regulates Endothelial Organization and Migration. *Regen Med* **7**, 649–661 (2012).

215. McCoy, M. G. *et al.* Collagen Fiber Orientation Regulates 3D Vascular Network Formation and Alignment. *ACS Biomater. Sci. Eng.* **4**, 2967–2976 (2018).

216. Mammoto, T. *et al.* Role of Collagen Matrix in Tumor Angiogenesis and Glioblastoma Multiforme Progression. *The American Journal of Pathology* **183**, 1293–1305 (2013).

217. Ray, A. & Provenzano, P. P. Aligned forces: Origins and mechanisms of cancer dissemination guided by extracellular matrix architecture. *Current Opinion in Cell Biology* **72**, 63–71 (2021).

218. Provenzano, P. P. *et al.* Collagen reorganization at the tumor-stromal interface facilitates local invasion. *BMC Medicine* **4**, 38 (2006).